Dissertation

submitted to the

Combined Faculties of the Natural Sciences and Mathematics

of the Ruperto-Carola-University of Heidelberg, Germany

for the degree of

Doctor of Natural Sciences

Put forward by

Andreas Weigel

born in Schemonaicha, Kazakhstan

Oral examination: January 16th, 2019

Detection Electronics Design and First Observation of Bound-Electron Spin Transitions at the ALPHATRAP g-Factor Experiment

Referees: Prof. Dr. Klaus Blaum
Prof. Dr. Selim Jochim

Zusammenfassung

Entwicklung der Detektionselektronik und erster Nachweis von Spinübergängen des gebundenen Elektrons am ALPHATRAP g-Faktor-Experiment

ALPHATRAP ist ein Penning-Fallen-Experiment, welches sich am Max-Planck-Institut für Kernphysik (MPIK) befindet. Es widmet sich der Erforschung von schweren, hochgeladenen Ionen im Grundzustand. Das Hauptanliegen des ALPHATRAP-Experiments sind hochgenaue Messungen des g-Faktors des gebundenen Elektrons. Der Vergleich des experimentell ermittelten Wertes mit jüngsten theoretischen Berechnungen dient als ein empfindlicher Test der Quantenelektrodynamik (QED) gebundener Zustände und bietet zudem einen neuen Zugang für die Bestimmung von elementaren Naturkonstanten wie der Elektronenmasse oder der Feinstrukturkonstante α. Die Messung des g-Faktors des gebundenen Elektrons eines einzelnen hochgeladenen Ions wird in einem optimierten Penning-Fallen-Aufbau unter Ausnutzung des kontinuierlichen Stern-Gerlach-Effektes durchgeführt. Für den Einschuss von hochgeladenen Ionen bis hin zu $^{208}\mathrm{Pb}^{81+}$ verfügt das ALPHATRAP Experiment über eine Ankopplung an diverse Ionenquellen, einschließlich der Heidelberg Electron-Beam Ion Trap.

Diese Arbeit beschreibt den Aufbau und die Vorbereitung des ALPHATRAP Experiments für seine erste g-Faktor-Messung. In diesem Zusammenhang wurde ein neues hochempfindliches Detektionssystem implementiert und erfolgreich getestet. Dies ermöglichte eine erste Kommissionierung der gesamten Apparatur sowohl mit in situ erzeugten Ionen als auch mit Ionen, die mit Hilfe der Raumtemperatur-Strahlführung eingeschossen wurden. Der erstmalige Einbau eines von außen bedienbaren kryogenen Ventils ermöglichte dabei ein exzellentes Vakuum mit langen Ionenspeicherzeiten. Die Anwendung von typischen Techniken für die Detektion und Manipulation von gespeicherten Ionen wurde anhand von Charakterisierungsmessungen des Detektionssystems und der Fallenfelder demonstriert. Die Kommissionierung gipfelte in der ersten direkten Beobachtung von induzierten Spinübergängen des gebundenen Elektrons am ALPHATRAP Experiment.

Abstract

Detection Electronics Design and First Observation of Bound-Electron Spin Transitions at the ALPHATRAP g-Factor Experiment

ALPHATRAP is a Penning-trap based experiment located at the Max-Planck-Institut für Kernphysik (MPIK). It is dedicated to the exploration of ground-state properties of heavy, highly charged ions (HCI). The major goal of the ALPHATRAP experiment are high precision measurements of the bound-electron g-factor. The comparison of the experimental result with recent theoretical calculations will not only serve as a sensitive test of bound-state quantum electrodynamics (BS-QED) but also yields a new approach for the determination of fundamental constants such as the electron mass or the fine structure constant α. The measurement of the bound-electron g-factor of a single HCI is performed in an optimized cryogenic double Penning-trap setup, utilizing the continuous Stern-Gerlach effect. For injection of externally produced HCI up to $^{208}\mathrm{Pb}^{81+}$ the ALPHATRAP experiment is coupled to various ion sources, including the Heidelberg Electron-Beam Ion Trap. This thesis describes the setup and preparation of the ALPHATRAP experiment on its way towards its first g-factor measurement. In this context a new highly sensitive detection system was implemented and successfully tested. This enabled a first commissioning of the whole apparatus with in situ generated HCI as well as HCI injected through the room temperature beamline. The first-time integration of an externally operable cryogenic valve allowed for excellent vacuum conditions with long ion storage times. The implementation of typical ion detection and manipulation techniques was demonstrated by characterization measurements of the detection system and the trapping fields. The commissioning culminated in the first direct observation of induced bound-electron spin transitions at the ALPHATRAP experiment.

Contents

List of Figures

List of Tables

1 Introduction

With the formulation of the Dirac equation in 1928 [1], Paul Dirac paved the way for the development of the theory of quantum electrodynamics (QED), a blueprint of all the quantum field theories (QFT) which currently make up the mathematical structure of the Standard Model of particle physics (SM).

Since its formulation more then 40 years ago the SM reflects the current status of our understanding about the nature and classification of the elementary (fermionic) constituents of matter and their mutual interactions by the three fundamental quantum fields known as the electromagnetic, strong and weak force (mediated via gauge bosons). However, despite ongoing efforts [2], so far all attempts to extend the SM by incorporating also the 4th fundamental force of gravitation via a quantum mechanical substitution of the laws of general relativity were not convincing enough[1]. In this sense, the SM is suspected to be just an intermediate step on the way towards already proposed higher-level theoretical frameworks such as a Grand Unified Theory (GUT) [3, 4] of particle physics [2] or a superior Theory of Everything (ToE), the unification of all known fundamental interaction forces including gravity, a yearning goal of physics.

In the course of the years, some further observations were made which also may speak for the incompleteness of the Standard Model. Prominent among those are for example the baryon asymmetry in the universe, the existence of the neutrino masses, the composition and origin of dark matter and dark energy, or the discrepancy in the determination of the proton radius (proton radius puzzle) which was once again confirmed in 2017 [5]. Because of these and other deficiencies the SM is persistently verified with different experimental approaches and continuously improving accuracy throughout the whole currently accessible energy range. However, so far none of the predictions of the SM have been definitely disproved by experiments.

Probing Quantum Electrodynamics

Among the three cornerstones of the SM[3], QED has become a prime example of a successful quantum field theory. The beginning of QED can be traced back to the discovery of the Lamb-Shift and the anomalous magnetic moment $a = \frac{g-2}{2}$ of

---

[1] Due to the high energy scales involved, the problem lies predominantly in the experimental verification of existing theoretical approaches [3].

[2] The GUT focuses on the expected merging of the electromagnetic, weak and strong force in the high energy limit of which the first two have already been successfully combined in the electroweak theory.

[3] quantum electrodynamics, quantum chromodynamics (QCD) and quantum flavourdynamics (QFD)

the electron, where g is the gyromagnetic factor or g-factor (introduced in the next chapter). Since then, these measurable quantities have played an indispensable role in the evolution and verification of QED and the SM in general. This can be mainly attributed to the high degree of accuracy with which they can be determined both theoretically and experimentally. For decades, the comparison of both methods has been used to test the underlying theory but at the current level of precision no significant discrepancy was observed. Nevertheless, it is assumed that the measurement is sensitive to all kinds of SM contributions and that a strong deviation between the experimental value a_{exp} and the theoretical prediction of the Standard Model a_{SM} would indicate its incompleteness and thus the possible existence of new physics [6]:

$$a_{exp} = \underbrace{a_{QED} + a_{QCD} + a_{weak}}_{a_{SM}} + a_{new}. \tag{1.1}$$

The measurement of the anomalous magnetic moment of the muon at Brookhaven National Laboratory (BNL) showed first deviations from the theoretical prediction by more than 3 standard deviations [7] and thus temporarily disturbed the long-running success story of the Standard Model[4]. Another experiment called "Muon g-2" at Fermilab is currently in preparation and is expected to provide an independent verification of the BNL measurement. Because of their higher mass, muon (and also tau leptons) are particularly sensitive to other contributions within and possibly outside the SM. However these benefits are also associated with a short lifetime. Being the lightest electrically charged lepton the electron is considered to be stable which allows for high-precision measurements due to long observation times. In fact, the most sensitive measurements of the anomalous magnetic moment and the g-factor so far are the ones performed on a single electron/ion in a Penning-trap apparatus. Motivated by the rapid development of the theory of QED in the early 60s this technique was initially introduced by Dehmelt in 1959[5]. Since then, it was continuously improved in numerous experiments. Until now the most accurate measurement of the anomalous magnetic moment of a free electron was accomplished in a Penning-trap apparatus. It achieved a relative uncertainty of $\delta a_e/a_e = 0.24 \cdot 10^{-9}$ [9, 10]. In combination with an independent high-precision measurement of the fine structure constant [11], the crucial coupling constant which is also needed as an input parameter in a perturbative QED series expansion, this allowed for the so far most stringent test of free-field QED. According to the latest calculations the difference between theory and experiment amounts [12]

$${a_e}^{exp} - {a_e}^{theo} = -0.91(0.82) \cdot 10^{-12}. \tag{1.2}$$

---

[4] Typically, a discrepancy of 5 sigma is defined as the critical threshhold for a new discovery within the Standard Model.

[5] Earlier experiments on the electron anomaly were carried out e.g. by Crane and coworkers at the University of Michigan [8].

Probing QED of Bound States

Despite the remarkable result of the free electron experiment, the question about the validity of QED applies to all accessible interaction energies and field strengths. Apart from high-energy tests at collider facilities such as the LHC, the regime of intense magnetic and electric fields is of special interest. Here, possible non-linear effects associated with the field strength might be intensified and thus become detectable. In this regard, highly charged ions (HCI) are perfect candidates for investigating such effects. The remaining ground-state electrons in HCI are exposed to the extreme electrical field of the nucleus which also shields them from external influences. The electrical field acting on the 1s electron in hydrogenlike lead/uranium is on the order of 10^{18} V/m, and thus even approaches the Schwinger limit [6] $E_S \approx 1.3 \times 10^{18}$ V/m [13], where the QED-vacuum itself is expected to become unstable. From the theoretical perspective HCI, especially those with only few or a single electron left, are well-defined systems whose properties can be accurately described in the framework of bound-state QED (BS-QED). Furthermore, BS-QED contributions increase with the nuclear charge number and are thus more accessible to experiments.

Notable experiments on HCI in the high-field regime have already been performed at the GSI heavy ion research facility. Among those are spectroscopy based methods such as measurements of the Lamb shift in hydrogenlike $^{238}\mathrm{U}^{91+}$ [14] or the hyperfine-splitting (HFS) in hydrogenlike and lithiumlike HCI [15, 16]. These experiments allow for BS-QED tests in the highest achievable electric and magnetic fields. However, difficulties arise from the bad knowledge of the nuclear structure/properties imposing a major limitation on the accuracy of the theoretically predicted value. Such limitations can be overcome to a certain degree by minimizing (the sensitivity to) unknown nuclear properties in so-called specific differences between different charge states of the same HCI [17, 18]. In 2017 this method was applied in the HFS measurement of hydrogen- and lithiumlike bismuth $^{209}\mathrm{Bi}^{82+,80+}$ [16].

As mentioned before, in terms of precision, QED tests via measurements of the electron anomaly in a Penning-trap are so far unrivaled. This is also true for BS-QED tests, where the anomaly is accessed by measuring the g-factor of the electronic ground-state of a HCI situated in a Penning-trap. An important feature of this method is that it can be applied to virtually any HCI. In contrast to the Lamb shift or the HFS the basic measurement principle does not involve optical electronic transitions (although some of them can be addressed for special purposes [19]). Furthermore, measuring HCI without nuclear spin allows to significantly reduce the influence of nuclear contributions[7].

---

[6] Actually, the Schwinger Limit is calculated for homogeneous fields. Here, the comparison only serves to give an illustrative impression of the magnitude and possible implications.

[7] In HFS calculations the Bohr-Weisskopf effect, arising from the poorly known distribution of magnetization in the nucleus, increases the uncertainty.

The Mainz g-Factor Experiment

So far the most sensitive g-factor measurements on electrons bound in HCI were performed with the g-factor Penning-trap experiment at the Johannes Gutenberg-University in Mainz. The measurement principle is based on the determination of two frequencies, namely, the free cyclotron frequency of the ion as well as the Larmor spin-precession frequency of the electron. The measurement process is distributed over two spatially separated traps: The precise determination of the free cyclotron frequency of the ion via image charge detection (chapter 3.2.4) is performed in the so called precision trap (PT) which features the essential homogeneous magnetic field. On the other hand, the Larmor frequency is measured by probing spin transitions with microwave excitations and subsequently analyzing the spin state in the analysis trap (AT), a dedicated magnetic bottle which allows to exploit the Continuous Stern-Gerlach effect (introduced in chapter). The development of this so called double-trap technique constituted a major breakthrough in terms of precision. From the year 2000 on, this technique enabled the group around H.-J. Kluge, G. Werth, W. Quint and K.Blaum to perform QED tests on a 10^{-9} level by measuring the g-factors of hydrogenlike carbon and later oxygen [20, 21]. In the further course, the experiment was completely revised by Sven Sturm and colleagues. The implementation of an integrated electron beam ion source (EBIS) into the trap tower allowed to access even heavier systems. Furthermore, improvements of the trap design, the cryogenic electronics and the introduction of a new phase-sensitive detection technique PnA [22] allowed to push down systematic shifts and significantly improve the sensitivity and precision of the experiment. These and other developments initiated a series of outstanding measurements at the Mainz experiment.

- In 2011 the g-factor of hydrogenlike silicon $^{28}Si^{13+}$ was measured with a relative precision of $\delta g/g = 5 \cdot 10^{-10}$ [23]. Until now this measurement constitutes the most stringent test of BS-QED for medium-heavy systems.

- In 2013 the same team specifically addressed many-electron BS-QED contributions by measuring the g-factor of lithiumlike $^{28}\mathrm{Si}^{11+}$ with $\delta g/g = 1.1 \cdot 10^{-9}$ [24].

- In 2014 the atomic mass of the electron was derived from a new high-precision measurement on hydrogenlike carbon $^{12}\mathrm{C}^{5+}$ in combination with the latest BS-QED calculations[8] [26, 27]. The new value features an impressive relative precision of $2.8 \cdot 10^{-11}$ and surpasses the earlier CODATA entry by more than one order of magnitude.

- In 2015 the first isotope shift between the g-factors of the valence electrons in lithiumlike $^{40}Ca^{17+}$ and $^{48}Ca^{17+}$ [28] was measured. This allowed to confirm the BS-QED contribution originating from the relativistic nuclear recoil effect on a 10^{-9} level.

---

[8] The method was introduced and already applied by the group of Günther Werth for the former measurement on hydrogenlike carbon. However, compared to the new measurement the earlier result was more then two orders of magnitude less accurate [25].

- For the time being the Mainz group is focusing on mass measurements of single nucleons. For this purpose the experiment was once more completely rebuilt. A part of the project was successfully completed in 2017 by measuring the atomic mass of a proton with a previously unattained precision of $\delta m_p/m_p = 32 \cdot 10^{-12}$ which however also disagrees with the former CODATA value by about 3 standard deviations [29]. A further more precise verification of this value as well as the measurement of the neutron mass are currently in preparation.

An important feature but also a major drawback of the Mainz experiment is its autonomy. It was designed as a stand alone experiment, meaning that in terms of its construction and current location it was not foreseen to be coupled to large scale ion sources. At present the only available ion production technique at the Mainz experiment is the small in-trap EBIS which for technical reasons does not allow for the generation of HCI with ionization-energies higher than 5 keV [9]. For now this and other circumstances restrict the Mainz experiment to g-factor and mass measurements on light- and medium-heavy ions. In order to extend the range of accessible systems to even higher masses and charge states, in 2013 the planning and construction of a new g-factor experiment, named ALPHATRAP, was initiated at the Max-Planck-Institut für Kernphysik (MPIK) in Heidelberg.

The ALPHATRAP Experiment

ALPHATRAP is a next generation g-factor experiment located at the MPIK and a direct successor of the Mainz g-factor experiment. Although the two experiment are conceptually very similar, the ALPHATRAP setup was designed with the special focus to perform ultra precise g-factor measurements on the heaviest HCI with ionization energies of up to 100 keV. This regime is currently only accessible via external ion sources such as the ESR at GSI [10] or the large superconducting electron-beam ion trap in Heidelberg (HD-EBIT) [30]. For this purpose, the ALPHATRAP setup is additionally connected to a dedicated ultra-high vacuum beamline which is already equipped with two ion sources including a laser ion source (LIS) [31] for the sympathetic laser-cooling with beryllium and a small table-top(tt) EBIT [32] for the production of medium mass HCI. The coupling to the large HD-EBIT is in preparation.
My PhD project at ALPHATRAP started in a very early stage of the experiment when major parts of the mechanical, cryogenic and electronic setup were still in the planning phase. This constituted on the one hand a great challenge but also the unique opportunity to be part of the complete development process from the first concept draft to a fully operational experiment. Building the experiment from scratch allowed to incorporate already approved techniques together with new design ideas. This thesis describes the preparation of ALPHATRAP for its first g-factor

---

[9] High voltage flashovers limit the maximum voltage that can be applied.

[10] not yet finalized in preparation

measurement. It comprises the assembly of large parts of the experimental setup including the development, implementation and testing of crucial components with a special focus on the electronic detection system. During my time as a PhD student the construction was completed and the commissioning phase of the whole experiment with HCI began. These were generated in situ as well as supplied by the small table-top EBIT and successfully injected through the room temperature beamline into the cryogenic Penning-trap setup. In this context the first integration of an externally operable cryogenic vacuum valve allowed for excellent vacuum conditions from the beginning on. Single ion storage times in excess of months were achieved. The commissioning included all essential mechanic and electronic components and covered ion generation and capturing, transport and cleaning as well as state-of-the-art detection and manipulation techniques. The commissioning culminated in the very first spin flip observation at the ALPHATRAP g-factor Experiment.

This thesis is organized as follows: Chapter 2 is a short introduction of the anomalous magnetic moment and the theoretical basics of the free and bound electron g-factor contributions. Chapter 3 introduces the ALPHATRAP experimental approach and the prerequisites and techniques needed for a high-precision g-factor measurement in a real Penning-trap apparatus. Chapter 4 gives a complete technical overview of the ALPHATRAP experiment including the available ion production techniques. Furthermore, it details on the design and test of the cryogenic setup including the new cryogenic valve and a description of the improved Penning-trap system. Chapter 5 is solely dedicated to the electronic detection system with a special focus on the design of the cryogenic detection electronics. Chapter 6 describes the first commissioning experiments. Apart from the demonstration of state-of-the-art cleaning, detection and manipulation techniques, major breakthroughs were the first successful injection of externally produced ions and the first observations of induced spin state transitions of the bound electron in a single $^{40}\mathrm{Ar}^{13+}$ ion in our experiment. Finally, chapter 7 gives a summary of this work and discusses the promising future prospects of ALPHATRAP.

2 Theoretical Basics

This chapter serves to give a brief introduction of the anomalous magnetic moment and the most basic concepts of QED and the free- and bound-electron g-factor which are required to motivate the work presented here.

2.1 The Anomalous Magnetic Moment

In quantum mechanics the magnetic dipole moment arising from the spin $\boldsymbol{S}$ i.e. the inherent angular momentum of a particle as the electron with elementary charge e and mass m is given by

$$\boldsymbol{\mu} = -\gamma \boldsymbol{S} = -g \frac{e}{2m} \boldsymbol{S}. \tag{2.1}$$

Here γ is the gyromagnetic ratio and $\mu = \frac{e\hbar}{2m}$ is the magneton or Bohr magneton μ_B in case of the electron. The dimensionless quantity g is called gyromagnetic factor or simply g-factor. It characterizes the strength of the magnetic interaction and is the deviation from the classically expected value where g=1 for objects with identical charge and mass distribution, which are spinning around an axis of symmetry [33]. In principle the history of g-factor measurements performed on atomic systems reach back more than 100 years. The intriguing discovery of the anomalous Zeeman effect in 1896 led to the modification of the simple Bohr model by the Bohr-Sommerfeld hypothesis only in 1916 [34]. It was partially confirmed by a direct measurement of the directional quantization of angular momenta in the famous Stern-Gerlach experiment in 1922. However, a complete understanding of the experimental observations, especially the often observed splitting of spectral lines into even numbers or the fine structure, could be only explained in 1925 by Goudsmit and Uhlenbeck by putting forward the concept of the electron having an intrinsic angular momentum or spin of 1/2. This can be considered as the advent of modern quantum mechanics.
As we know today, for an isolated electron, which has no known internal structure (Dirac particle), the spin and gyromagnetic factor follow directly from Dirac theory: In his relativistic treatment of quantum mechanics in 1928 Paul Dirac derived the spin of a freely propagating electron to be only half of the orbital momentum unit without further assumptions. As a direct consequence the spin of $s = 1/2\hbar$ is accompanied by a gyromagnetic factor of [1]

$$g_{Dirac} = 2 \tag{2.2}$$

---

[1] Based on the observation of the anomalous Zeeman effect the value of $g = 2$ was already phenomenologically proposed by Landé in 1923

to cause the same magnetic moment contribution of $1\mu_B$. In the following the value was experimentally confirmed by Kinster and Houston in 1934 [35].
The Dirac formalism was the first step of quantum electrodynamics (QED) [2], the gerneralized unification of quantum mechanics with classical electrodynamics and a "paradigmatic example of a successful quantum field theory" (Weinberg 1995). It allowed for direct calculation of various physical interaction processes between charged particles and electromagnetic radiation. However, it was problematic at higher orders of perturbation theory due to the emergence of infinities [37].
The applicability of Dirac theory to experimental observations found its first limitation with the Lamb-Retherford experiment and the discovery of the Lamb-Shift in 1947 [38]. The measured energy difference of only about 4 µeV between the energy levels $^2S_{1/2}$ and $^2P_{1/2}$ of a hydrogen atom, which were previously assumed to be degenerate, could not be derived from the Dirac equation.
The results of further experiments on the hyperfine structure of hydrogen and deuterium delivered strong indications for the existence of an "anomalous" magnetic dipole moment of the electron [39, 40], i.e. a relative deviation from the simple Dirac value of 2 expressed by

$$a = \frac{g-2}{2}. \tag{2.3}$$

At about the same time on the theory side the calculation of higher order effects was made possible by Hans Bethe by introducing a new calculation technique, which removed the divergent terms and is today known as renormalization [41]. This new approach and the following fundamental work of Shin'ichirō Tomonaga, Julian Schwinger, Richard Feynman and Freeman Dyson contributed to a fast development of the theory of quantum electrodynamics [42, 43, 44, 45].
In 1948 Schwinger managed to derive the dominant contribution[3] to the anomalous magnetic moment respectively the g factor from a first order perturbation calculation giving

$$a = \frac{\alpha}{2\pi} \iff g = 2 + \frac{\alpha}{\pi} \approx 2(1 + 0.0011614), \tag{2.4}$$

where the fine structure constant α is a measure for the coupling strength in QED. The first compatible experimental verification of the so called Schwinger term $\frac{\alpha}{\pi}$ was performed by Kusch and Foley [46] in the year of its prediction. Their measurement of the Zeeman effect of the two lowest states of gallium yielded a value of $g = 2.00238(10)$ and can be considered as the first successful precision test of QED. From there on the question about the scope of the validity of the new theory was at the center of interest. This motivated a series of fast developments on the theoretical as well as on the experimental side.
As mentioned earlier, so far, the most precise determination of the free electron g-factor was performed on a single electron in a Penning-trap by the group of Gerald

---

[2] Dirac was the first to use that term [36].

[3] It amounts 99% of the correction.

Gabrielse in 2008 [9, 10]. Their direct measurement of the anomalous magnetic moment reached a relative uncertainty of $0.24 \cdot 10^{-9}$ which corresponds to a relative uncertainty of $2.8 \cdot 10^{-13}$ for the final g-factor value[4]. The group is also planning to improve the precision with a new apparatus [47].

2.2 The g-Factor of an Isolated Electron

The Schwinger term $\frac{\alpha}{\pi}$ from equation (2.4) is only one of many possible contributions to the electron anomaly. They are caused by interactions of the electron with quantum fluctuations of the vacuum and the complete radiation field and are therefore often referred to as radiative corrections. They can be individually visualized via the corresponding Feynman diagrams, exemplary shown in figure 2.1. This formalism was developed by Richard Feynman as a graphical representation of the underlying mathematical equations describing the real and virtual coupling of charged particles to the electromagnetic field [48].

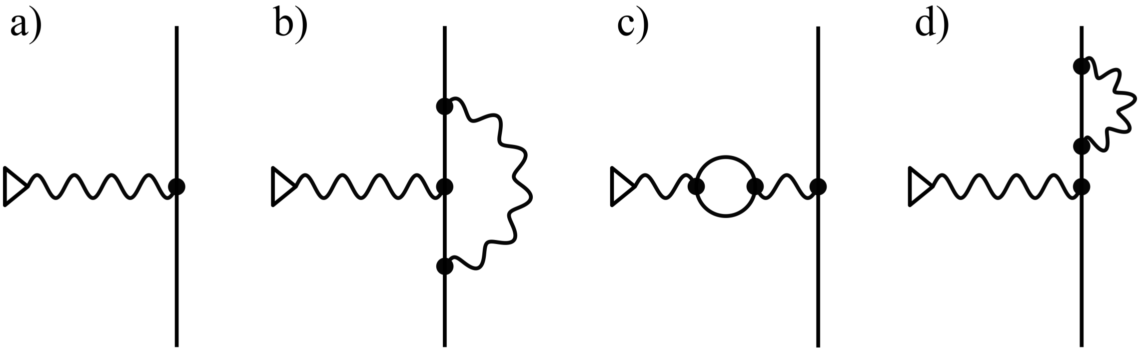

Figure 2.1: Low order Feynman diagrams for the free electron g-factor. The straight lines describe a freely propagating electron. Wavy lines represent real and virtual photon propagators. The triangle depicts an externally applied magnetic field. Interaction takes place at the vertices (black dots) involving the coupling constant $\sqrt{\alpha}$. a) The bare vertex diagram represents the pure Dirac value of $g_{Dirac} = 2$. b) The "vertex correction" (Schwinger term) is the dominant first order contribution to the anomaly. c) The "vacuum polarization" i.e. the interaction with a virtual lepton/anti-lepton pair represented by a circle. d) The "self energy" interaction of the electron with its own electromagnetic field. Diagrams c) and d) do not explicitly contribute to the free electron g-factor but are included in the renormalization.

---

[4] From equation (2.3) it is obvious, that determining the g-factor from a direct measurement of the anomalous magnetic moment is advantageous since it decreases the final uncertainty by a factor of $(1 + \frac{1}{a})^{-1} \approx 10^{-3}$.

A common procedure in QED is the series expansion of the electron anomaly or the g-factor in powers of the fine structure constant:

$$g = 2\left(1 + \sum_{n=1}^{\infty} C_{2n} \left(\frac{\alpha}{\pi}\right)^n + a(HVP) + a(weak)\right). \tag{2.5}$$

The order of the contribution $(2n)$ of a specific Feynman diagram is directly related to the number of closed "loops" (formed by virtual photons and particle/anti-particle pairs) appearing in the diagram. At higher order the number of possible diagrams and consequently the necessary arithmetical effort is rapidly increasing. However, due to the small value of $\alpha \approx \frac{1}{137}$ and $C_{2n} \approx \mathcal{O}(1)$ the higher order terms have a comparably smaller contribution than the higher order terms. Thus, the perturbation series rapidly converges and allows for adequate results even when calculating only a finite number of diagrams. Nevertheless, at increasing precision considerably more Feynman diagrams have to be taken into account.
Apart from the Schwinger Term with $C_2 = 0.5$, to date the C coefficients up to the 6th order (C_6) were calculated analytically. However, for the calculation of the 8th and 10th order 891 4-loop[5], respectively 12672 5-loop Feynman diagrams have to be taken into account which was accomplished numerically [50]. On this level of precision not only QED but also contributions involving quantum chromodynamics (QCD) such as hadronic vacuum-polarizations and also electroweak interactions become increasingly important [12] [6]. They are represented by extra terms $a(HVP)$ and $a(weak)$ in equation (2.5).
Interestingly, since the theoretically determined value for the g-factor is directly dependent on the fine structure constant, it is naturally also limited by its precision. Thus, a highly accurate determination of α via a method which is independent of QED, contributes to a more precise theoretical evaluation of the electron anomaly. Until now the best theoretical value for the anomalous magnetic moment was based on the fine structure constant derived from a rubidium recoil experiment ($\alpha_{exp}^{-1} = 137.035999049(90)$) [11, 12]:

$$a_{QED} = 1,159,652,181.643(25)(23)(16)(763) \cdot 10^{-12}, \tag{2.6}$$

where the first three brackets contain the intrinsic theoretical uncertainties (8th order, 10th order and hadronic/electroweak terms) while the 4th and largest error originates from the independent α measurement. Compared with the direct measurement of the anomalous magnetic moment by the group of Gerald Gabrielse [9, 10]:

$$a_{exp}^{g-2} = 1,159,652,180.73(28) \cdot 10^{-12}. \tag{2.7}$$

---

[5] Only recently an improvement in the numerical calculation of the 4-loop contribution to the electron $g-2$ with up to 1100 digits of precision was achieved by Stefano Laporta [49].

[6] In general, the magnitude of the individual contributions are sensitive to the square of the mass of the considered lepton species (termed "decoupling"). For example, in case of a muon which is 200 times heavier than an electron $a(HVP)$ is enhanced by a factor of 40000. As a consequence the muon is also expected to be comparably more sensitive to new physics beyond the Standard Model.

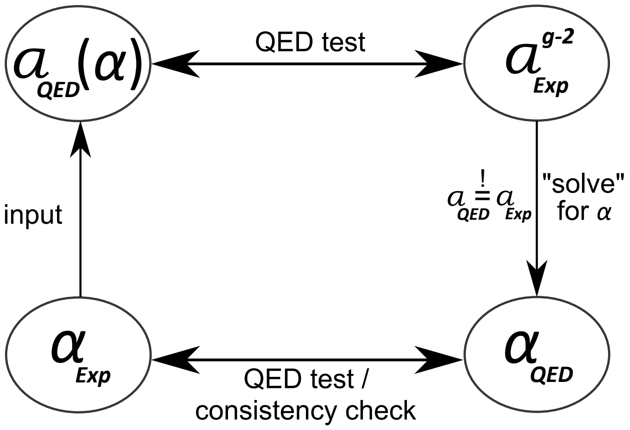

Figure 2.2: Flowchart visualizing the procedure for a two fold QED test.

this yields a sensitive test of QED. Furthermore, implying the correctness of QED, the theoretical value can be matched to the experimental value by adjusting the value of α. This enables a highly precise (QED-dependent) determination of the fine structure constant [12]:

$$\alpha_{QED}^{-1} = 137.0359991570(29)(27)(18)(331), \tag{2.8}$$

which corresponds to a relative uncertainty of $\delta\alpha/\alpha = 2.4 \cdot 10^{-10}$. The uncertainty is once more dominated by the experimental error (last bracket). This value was recently improved by an independent experimental determination of α based on the recoil frequency of cesium-133 atoms in a matter-wave interferometer [51]:

$$\alpha_{exp}^{-1} = 137.035999046(27). \tag{2.9}$$

The direct comparison of α_{QED} with α_{exp} allows for another test and consistency check of QED and the SM.

2.3 The *g*-Factor of a Bound Electron

As motivated in the first chapter the primary goal of ALPHATRAP is to perform ultra sensitive QED tests in the strong field regime. In this context measurements of the g-factor of an electron bound to a heavy nucleus are so far unrivaled (as was demonstrated by the Mainz experiment). The significance of bound systems and especially HCI can be understood from figure 2.3, where the expectation value for the electric field at the position of the single electron bound in a hydrogenlike ion is plotted against the nuclear charge number. The scope of systems accessible to the ALPHATRAP experiment allows to exceed the field strength achievable with modern high-intensity laser sources by many orders of magnitude[7].

---

[7] The Guinnes world record of ≈3×10^{14} V/m is hold by the HERCULES Petawatt Laser at the University of Michigan [52]. Other developments with field strengths exceeding 9×10^{15} V/m are foreseen [53]. However, the pulse duration of such facilities is typically on the order of femtoseconds, while the local beam intensity is difficult to control.

In comparison with a free electron the bound electron g-factor is notably altered by a number of effects arising from the interaction with the binding potential and the nucleus (figure 2.6) which are briefly addressed in the following.

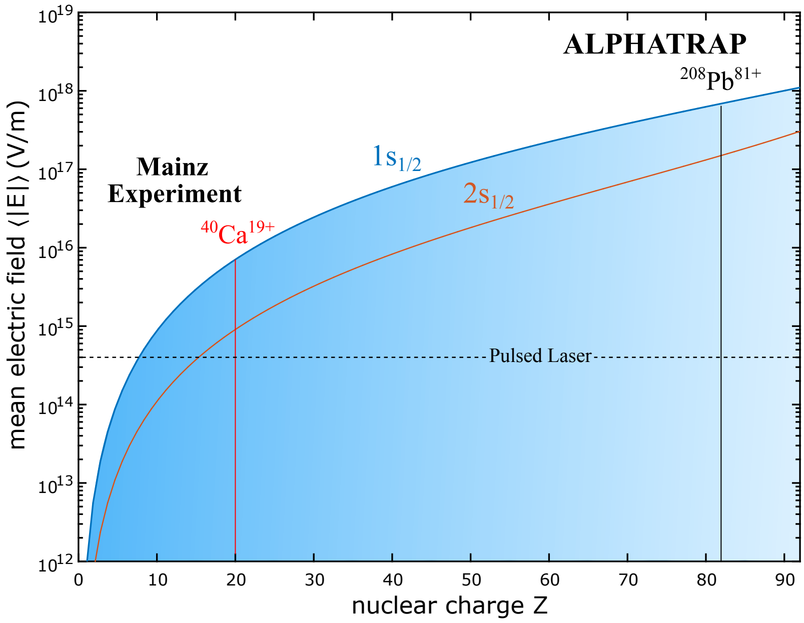

Figure 2.3: Expectation value for the electric field acting on the electron in the $1s_{1/2}$ and $2s_{1/2}$ state in hydrogenlike ions plotted against the nuclear charge number Z. For $Z > 8$ the field strength in a HCI exceeds the value achievable with modern pulsed lasers. The left vertical line marks the limit of the experimental scope accessible with the Mainz experiment. Being coupled to large external ion sources as the HD-EBIT, ALPHATRAP advances into the extreme field regime of up to 10^{18} V/m. For comparison: For homogeneous electric fields strong nonlinear effects are awaited at the so called Schwinger limit $E_S \approx 1.3 \times 10^{18}$ V/m where the QED-vacuum is expected to become unstable.

The Relativistic Bound Electron g-Factor

A rigorous relativistic treatment is particularly important in the case of HCI. Already in 1928, shortly after the formulation of the Dirac equation for the free electron, Charles Galton Darwin [54] and Walter Gordon [55] solved the stationary Dirac equation for a single electron in a pure Coulomb potential by simplifying the nucleus to be a point charge with infinite mass. The relativistic calculation results in a shifting and splitting (fine structure) of the former degenerate energy levels according to:

$$E_{nj} = m_e c^2 \left(1 + \left(\frac{Z\alpha}{n - |j+1/2| + \sqrt{(j+1/2)^2 - (Z\alpha)^2}} \right)^2 \right)^{-1/2} . \tag{2.10}$$

For a ground state electron ($n = 1$, $j = 1/2$) this simplifies to

$$E_{1s_{1/2}} = m_e c^2 \sqrt{1 - (Z\alpha)^2}, \tag{2.11}$$

which corresponds to a decreasing of the 1s energy level (compared to the non-relativistic case). Based on the work of Darwin and Gordon, Gregory Breit derived the relativistic magnetic moment of the bound electron [56]. Compared to the free electron g-factor of $g_{Dirac} = 2$ the bound g-factor is modified according to the equation

$$g_{Dirac}^{bound} = 2 \left(\frac{1 + 2\sqrt{1 - (Z\alpha)^2}}{3} \right) = 2 \underbrace{- \frac{2}{3}(Z\alpha)^2 - \frac{1}{6}(Z\alpha)^4 + \ldots}_{\Delta g_{Breit}} . \tag{2.12}$$

The Breit contribution Δg_{Breit} is increasing with the nuclear charge number Z. For $Z > 8$ the Breit term which can be considered as a pure relativistic effect, is the dominant contribution depending on α. In this way it holds the potential for an independent high-precision determination of the fine structure constant.

Radiative Corrections

Aside the QED effects (discussed in chapter 2.2) appearing in the interaction between the electron and a weak external magnetic field ("free QED") the transition to the bound electron necessitates to consider also the electromagnetic coupling to the nucleus.

In accordance to the free electron the contributions to the bound electron g-factor can be evaluated with a perturbative series expansion in the framework of bound state QED (BS-QED). In this regard, two methods have become established:

- Using the free electron propagator requires to modify the expansion in α/π by an additional expansion in $Z\alpha$ which accounts for the radiative corrections affecting the photon exchange with the nucleus. However, considering that $\alpha \approx 1/137$, especially for high Z the slow convergence of the $Z\alpha$ series is troublesome and requires to evaluate a large number of complicated Feynman diagrams to get a reasonable precision. Therefore this method is predominantly applied in the low Z regime.

- In order to avoid a perturbative series expansion in $Z\alpha$ for heavy systems an alternative approach is the calculation in the so called Furry picture, a classical time independent external field approximation of the nuclear potential [57].

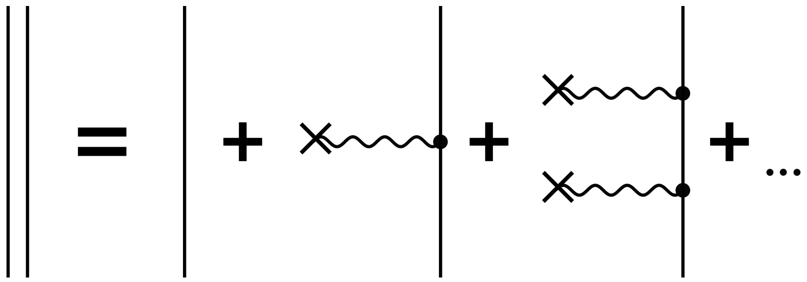

Figure 2.4: In BS-QED Feynman diagrams the double line represents the electron propagator in the field of the nucleus in the Furry picture. It includes the vertex corrections of the interaction with the Coulomb potential in all orders of $Z\alpha$.

> This allows to include all orders in $Z\alpha$ in the electron propagator (figure 2.4) by using the eigenfunctions of the Dirac equation (of the bound system) as a basis [58].

So far the one loop corrections (order α/π) to the g-factor of a hydrogenlike ion, represented by the six Feynman diagrams in 2.5 were evaluated in all orders of $Z\alpha$ using the second approach [59, 60, 61].
Currently, the calculation of two loop contributions which requires the evaluation of 49 Feynman diagrams is incessantly progressing. By now analytic results for specific subsets of diagrams up to the order $\alpha^2(Z\alpha)^5$ are available [62, 63, 64]. To date, the uncalculated higher order contributions constitute the dominant uncertainty to the theoretical prediction of the bound electron g-factor.

Interelectronic Contributions

When considering also many electron ions the mutual photon exchange between the shell electrons necessitates an additional evaluation of special Feynman diagrams (not shown here) in orders of $1/Z$. In references [18, 66] the pure interelectronic contributions (i.e. diagrams without additional radiative loop corrections) for lithiumlike systems have been calculated up to the second order in $1/Z$ (two photon exchange). The remaining diagrams which also include self-energy and vacuum-polarization terms (so called screened QED corrections) are discussed in [66].

Nuclear Corrections

The hitherto discussed contributions to the bound electron g-factor were assuming a pure Coulomb potential originating from an idealized pointlike nucleus with infinite mass. However, the properties of a real nucleus give rise to additional corrections which have to be treated individually.

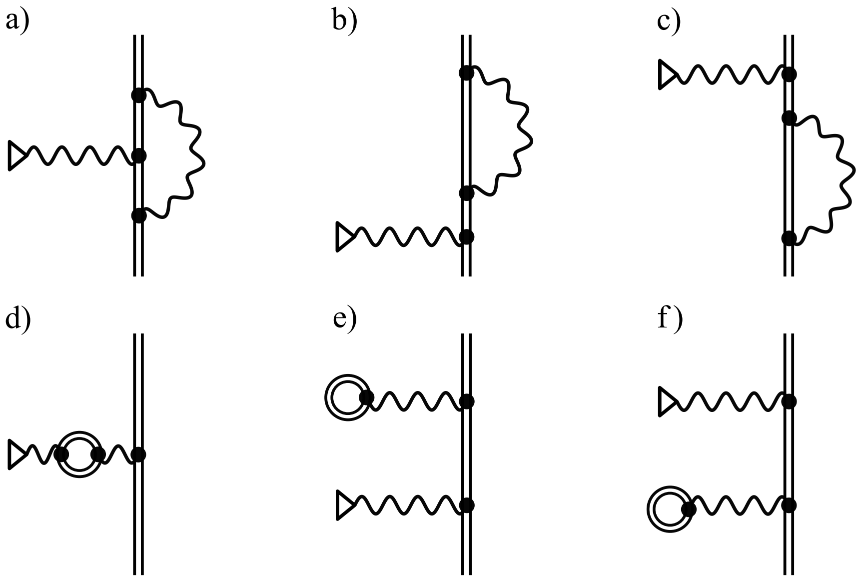

Figure 2.5: Feynman diagrams of the six one loop corrections contributing to the bound electron g-factor. a): Self-energy vertex term. b) and c): Self-energy wave function corrections. d): Vacuum polarization potential term. c) and f): Vacuum polarization wave function corrections.

Finite Nuclear Size and Shape The finite nuclear size correction accounts for the extended charge distribution of the nucleus which affects the electron wave function and thus also the binding energy and the g-factor. It can be deduced by solving the Dirac equation for the extended nucleus which can be modeled by an appropriate radial charge distribution $\rho(r)$ characterized by the nuclear root-mean-square charge radius [8] $r_{rms} = \langle r^2 \rangle^{1/2}$ [58].
In [67] the leading non-relativistic and dominant relativistic contribution to the nuclear size correction is perturbatively calculated for low and medium heavy systems (Z=1-20). Higher order effects are considered in [68].
At high nuclear charge numbers, additional shape effects beyond a spherical nuclear model become increasingly important[9], imposing a limitation on the theoretical precision. The calculation of specific shape corrections (quadrupole and hexadecapole deformation) is carried out in [69].
In general the impact of nuclear shape effects can be reduced by performing g-factor measurements on HCI with doubly magic nuclei (i.e. nuclei with completely filled proton and neutron shells) which are spherically symmetric, as for example ^{4}He, ^{40,48}Ca or ^{208}Pb.

---

[8] The nuclear charge radius can be measured in scattering experiments but can also be derived from a g-factor measurement. This method was for the first time demonstrated on hydrogenlike silicon [23].

[9] For hydrogenlike uranium the nuclear shape effects amounts $\approx$ 1ppm of the total contribution to the g-factor [69].

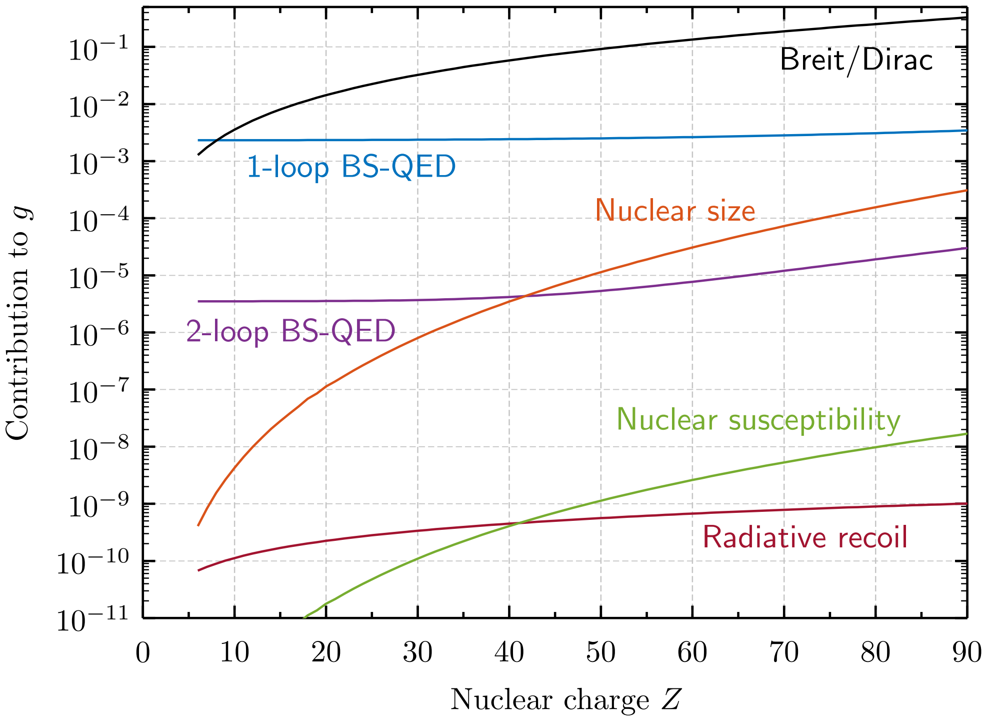

Figure 2.6: Relative contributions to the bound electron g-factor of a hydrogenlike ion. The complete calculation of the one loop contributions has already been carried out numerically. The two-loop contributions are not yet fully evaluated and are represented by selected leading orders in $Z\alpha$. All contributions are increasing with Z and are thus more accessible to experiments. Taken from [65].

Nuclear Polarization Apart from a static deformation the nuclear structure/shape is also prone to changes arising from intrinsic excitations of the nuclear energy levels by virtual photon exchange with the shell electrons. Especially for heavy systems as hydrogenlike uranium the nuclear polarization cannot be neglected since its relative contribution to the bound g-factor scales up to a 10^{-6} level [70]. In [71] the nuclear polarization correction is evaluated up to the first order in a $1/Z$ series expansion.

Nuclear Recoil Compared to the time independent external field approach, the consideration of the finite nuclear mass necessitates for a separate evaluation beyond the furry picture, which accounts for the mutual dynamics of the nucleus and the shell electron. In [72, 73] such an evaluation of the relativistic recoil correction to the g-factor is derived and calculate to all orders in αZ and to first order in m_e/M, where M is the mass of the nucleus. In 2015 the theoretical prediction was experimentally verified by the Mainz group who specifically addressed the recoil correction by measuring the g-factor difference of the doubly magic calcium isotopes $^{48}\mathrm{Ca}^{17+}$ and $^{40}\mathrm{Ca}^{17+}$ [28]. This special isotope pair stands out by a comparatively large mass difference combined with a very similar nuclear size. Due to this similarity, limiting uncertainties of higher order contributions are canceled in the difference of the g-factors and the isotopic shift is almost completely (99.96%) dominated by the nuclear recoil contribution.

Nuclear Magnetic Moment In reality the net nuclear magnetic moment of a spin carrying nucleus is originating from a finite spread of the nuclear magnetization instead of a hypothetical pointlike magnetic dipole. The poorly known distribution of the magnetization within the nucleus gives rise to a hyperfine anomaly also referred as the Bohr-Weisskopf effect [74]. In bound g-factor measurements this effect can be avoided by focusing on isotopes with zero nuclear spin.

3 The ALPHATRAP g-Factor Experiment

The ALPHATRAP experiment builds upon the experience and success of its predecessor experiment in Mainz. While the Mainz experiment is technically limited to low- and medium mass HCI, ALPHATRAP is designed with the special focus to extend the range of accessible systems to the high mass regime. Apart from mechanical differences and certain improvements which will be discussed in chapter 4, the basic procedure of a g-factor determination at both experiments rests on a common ground concerning the underlying experimental principles. This chapter serves to introduce the essential experimental tools and techniques which were partly adopted by the ALPHATRAP experiment.

3.1 Experimental Approach

Experimentally the g-factor can be addressed by exploiting the spin quantization. For spin 1/2 particles such as the electron there are only two possible eigenvalues $\pm\hbar/2$ of the spin operator $\boldsymbol{S}$ [1] observable along any axis. This also applies in the case of a valence s-state electron bound in a HCI without nuclear spin. In an externally applied magnetic field $\boldsymbol{B} = B\boldsymbol{e_z}$ (w.l.o.g.), the z-component of the electron spin has two possible orientations, i.e. either parallel or antiparallel, in respect to the external field. The interaction of the electron spin related magnetic moment $\boldsymbol{\mu}$ with the magnetic field leads to a Zeeman splitting (anomalous Zeeman effect) of the degenerate ground state energy level E_0 into two sublevels

$$E_{\pm} = E_0 \pm g\boldsymbol{\mu}\boldsymbol{B} = E_0 \pm g\frac{\mu_B B}{2}. \tag{3.1}$$

The M1-transition between the sublevels is associated with a spin transition or "spinflip" and a photon energy of

$$\Delta E = g\mu_B B = h\nu_L, \tag{3.2}$$

where the frequency of the photon is given by the Larmor spin precession frequency ν_L of the electron. Looking at equation (3.2) it is obvious that it allows for a direct determination of the g-factor via a measurement of the Larmor frequency. Simultaneously the strength of the external magnetic field has to be determined. For this one can exploit the fact, that the external magnetic field not only interacts with the electron but also implies a circular motion of the whole ion with mass m_{ion} and charge q_{ion}. The revolution frequency of the motion is given by the free

---

[1] Strictly speaking this is true for the projection operators $s_{x,y,z}$ along any axis x,y,z.

cyclotron frequency $\nu_c = \frac{q_{ion}}{2\pi m_{ion}} B$. In combination with equation (3.2) the g-factor thus follows from

$$g = \frac{\nu_L}{\nu_c} \frac{\hbar}{\mu_B} \frac{q_{ion}}{m_{ion}} = 2 \frac{\nu_L}{\nu_c} \frac{m_e}{m_{ion}} \frac{q_{ion}}{e}. \tag{3.3}$$

Provided that the ions and electrons charge-to-mass ratio are known[2], the determination of the g-factor can be thus reduced to the measurement of the frequency ratio $\Gamma = \frac{\nu_L}{\nu_c}$. Therein lies the beauty of this approach.

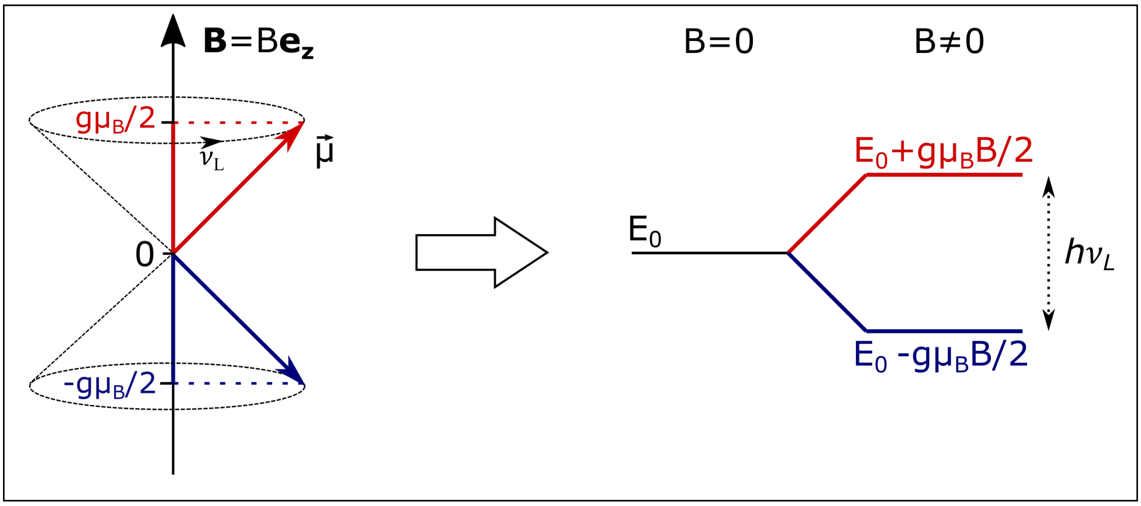

Figure 3.1: For an electron which is situated in an external magnetic field applied along the z-axis, there are only two possible values for the z-component of the spin induced magnetic moment. The external field is associated with a symmetry breaking which causes the splitting of the former degenerate energy level into two sublevels. The transition energy between the sublevels is characterized by the Larmor precession frequency. Adopted from [76].

3.2 The Penning-Trap

The Penning-trap[3] is a particle trap and the central tool in our experiment. Originally, the Penning-trap was introduced by Dehmelt in 1959 for the measurement of

---

[2] In principle the knowledge of the electron-to-ion mass ratio $\frac{m_e}{m_{ion}}$ is already sufficient since $\frac{q_{ion}}{e} \in \mathbb{N}$. A highly precise value for the atomic mass of the electron can be independently derived from a bound electron g-factor measurement on carbon (as was demonstrated by the Mainz group [26]), while the ion mass follows from dedicated mass spectrometer experiments such as PENTATRAP [75].

[3] Named after the dutch physicist Frans Michel Penning, who was the first to suggest the underlying experimental principle [77].

the free electron anomaly. Since then, it has developed to an indispensable, versatile instrument in different branches of physics and numerous precision experiments involving the investigation of fundamental properties of atomic systems and their elementary constituents [78]. The Penning-trap is characterized by very long particle storage times, combined with well defined and accurately controllable experimental conditions. These allow to perform non-destructive[4] high-precision measurements on single long-lived charged particles which are exposed to the strong homogeneous magnetic trapping field and cooled to small motional amplitudes. Thus, the Penning-trap inherently fulfills the special requirements which are necessary for a g-factor measurement via the experimental approach discussed in the previous section.

3.2.1 The Ideal Penning-Trap

Essentially, the ideal Penning-trap is a special static field configuration which enables the confinement of a charged particle in all three space dimensions. For radial confinement a strong axial homogeneous magnetic field $\boldsymbol{B} = B\boldsymbol{e_z}$ is applied. As a consequence the magnetic Lorentz force

$$\boldsymbol{F_L} = q \cdot \boldsymbol{v} \times \boldsymbol{B} = qB \begin{pmatrix} \dot{y} \\ -\dot{x} \\ 0 \end{pmatrix} \tag{3.4}$$

binds a particle of charge q, mass m and velocity $\boldsymbol{v}$ on a helical trajectory which is characterized by the free cyclotron revolution frequency

$$\omega_c = \frac{qB}{m}. \tag{3.5}$$

For axial confinement a superimposed, rotationally symmetric electric field $\boldsymbol{E(z,\rho)} = -\nabla\Phi(\boldsymbol{z},\boldsymbol{\rho})$ is generated by a quadrupole potential

$$\Phi(\boldsymbol{z},\boldsymbol{\rho}) = \frac{\Phi_0 C_2}{2d^2}\left(\boldsymbol{z}^2 - \frac{\boldsymbol{\rho}^2}{2}\right), \tag{3.6}$$

where $\boldsymbol{\rho}^2 = \boldsymbol{x}^2 + \boldsymbol{y}^2$, C_2 is a geometry dependent dimensionless constant and

$$d^2 = \frac{1}{2}\left({z_0}^2 + \frac{{\rho_0}^2}{2}\right) \tag{3.7}$$

represents a characteristic length scale given by the inner trap dimensions z_0 and ρ_0 (figure 3.3). The most convenient way to create such a potential is by applying a DC voltage $V_r = \Phi_0$ between the ring and the two endcap electrodes of a hyperbolic Penning-trap configuration as shown in figure 3.3. Here the equipotential surfaces given by equation 3.6 are intrinsically defined by the (ideally infinitely extended) hyperbolic electrode shape.

---

[4] This implies no particle loss during the measurement.

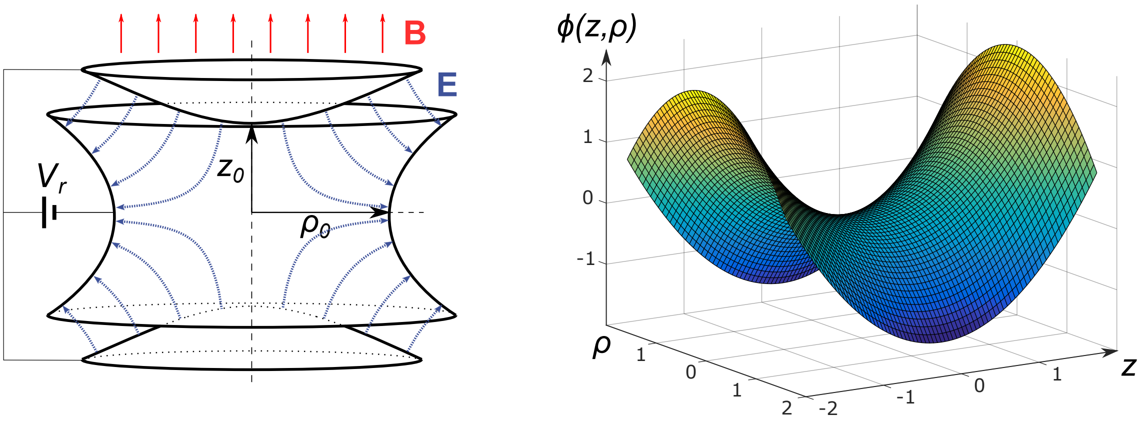

Figure 3.2: In the left picture a hyperbolic Penning-trap configuration is sketched. B and E denote the static superimposed magnetic and electric trapping field. The characteristic length scale d is defined by the inner trap dimensions z_0 and ρ_0 according to equation (3.7). The voltage polarity of V_r is chosen such that the electric field direction enables the trapping of positively charged particles. The electric field lines are perpendicular to the equipotetial surfaces which are dictated by the hyperbolic electrode shape. This results in a quadrupole potential as shown in the right side plot in arbitrary units.

3.2.2 Confined Particle Motion in a Penning-Trap

The ideal field configuration previously described affects the trajectory of a single trapped charged particle which can be derived by solving the associated differential equation of motion. Assuming a classical, non-relativistic particle motion it can be written as:

$$m \begin{pmatrix} \ddot{x} \\ \ddot{y} \\ \ddot{z} \end{pmatrix} = \frac{qV_r C_2}{2d^2} \begin{pmatrix} x \\ y \\ -2z \end{pmatrix} + qB \begin{pmatrix} \dot{y} \\ -\dot{x} \\ 0 \end{pmatrix}. \tag{3.8}$$

The complete analytic solution of this equation and a detailed analysis of the fundamental properties of a Penning-trap are summarized in [79]. In general the resulting motion is a superposition of three harmonic eigenmotions. The independent oscillation in the axial direction is characterized by the axial frequency

$$\omega_z = \sqrt{\frac{qV_r C_2}{md^2}}, \tag{3.9}$$

which accordingly can be adjusted by the applied trapping voltage V_r. In the radial direction the combination of the axial magnetic field and the radial electric field component have a twofold effect: The free cyclotron frequency (equation (3.5)) is

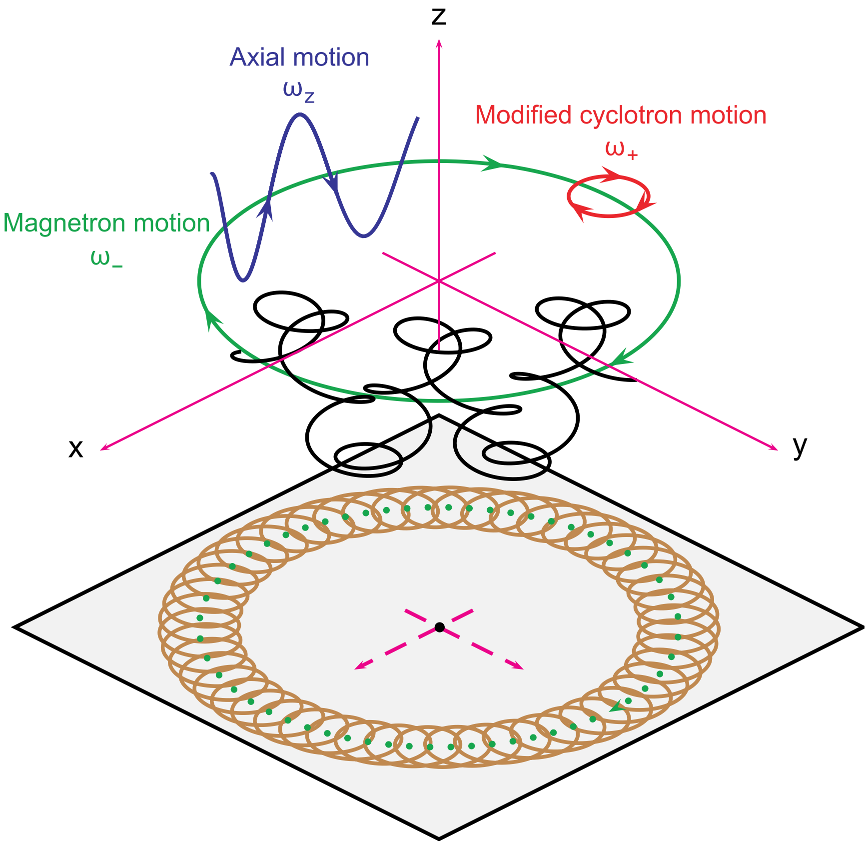

Figure 3.3: In a Penning-trap a charged particle undergoes a complicated motion which is a superposition (black curve) of three harmonic oscillating eigenmotions. The projection of the motion to the xy-plane describes an epitrochoidal trajectory. Here the oscillation amplitudes are arbitrarily chosen. (from [80])

modified to the reduced cyclotron frequency ω_+. Additionally, this circular oscillation is overlapped with a slow azimuthal $\boldsymbol{E} \times \boldsymbol{B}$ drift motion around the electrostatic trap center with the so called magnetron frequency ω_-. The magnetron and the reduced cyclotron frequency are related to the axial- and the free cyclotron frequency by the equation

$$\omega_\pm = \frac{\omega_c}{2} \pm \sqrt{\frac{\omega_c^2}{4} - \frac{\omega_z^2}{2}}. \tag{3.10}$$

Stable confinement of charged particles in a Penning-trap necessitates to fulfill certain basic stability criteria. Naturally, axial confinement is only possible if the axial depth of the electrostatic potential well (equation (3.6)) is deeper than the axial kinetic energy. The stability criterion for radial confinement follows from equation (3.10) where the discriminant can only stay positive as long as

$$\omega_c \geq \sqrt{2}\omega_z \quad \text{or} \quad B \geq \sqrt{\frac{2mV_rC_2}{qd^2}} \tag{3.11}$$

is fulfilled. Physically this means that the confining magnetic field has to be sufficiently strong to compensate for the outwards directed, radial electric field component. For typical operation conditions the three eigenfrequencies follow the hierarchy relation:

$$\omega_c > \omega_+ \gg \omega_z \gg \omega_-. \tag{3.12}$$

Furthermore, equation (3.10) implies the following useful relations which however only hold for an ideal Penning-trap:

$${\omega_z}^2 = 2\omega_+\omega_-, \tag{3.13}$$

$$\omega_c = \omega_+ + \omega_-. \tag{3.14}$$

When considering also certain deviations from the ideal trapping field configuration (as will be discussed in the next section) equation (3.14) is replaced by the more general *invariance theorem* [81]

$${\omega_c}^2 = {\omega_+}^2 + {\omega_z}^2 + {\omega_-}^2. \tag{3.15}$$

Classically the total energy of a charged particle in a Penning-trap is given by [5]

$$E = \underbrace{\frac{1}{2}m{\omega_z}^2{a_z}^2}_{E_z} + \underbrace{\frac{1}{2}m{\omega_+}^2{a_+}^2 - \frac{1}{4}m{\omega_z}^2{a_+}^2}_{E_+} + \underbrace{\frac{1}{2}m{\omega_-}^2{a_-}^2 - \frac{1}{4}m{\omega_z}^2{a_-}^2}_{E_-} \pm g\frac{\mu_B B}{2}, \tag{3.16}$$

where a represents the respective oscillation amplitude. The last term accounts for the additional Zeeman splitting in the axial magnetic field if the particle also carries a spin of $1/2$ (see equation 3.1).

From equation (3.16) and the hierarchy relation (3.12) one can see that the magnetron energy E_- is mainly dominated by the potential energy term which is decreasing for increasing particle amplitudes. Apart from collisions with contaminating particles, a spontaneous change of the oscillation amplitude is inhibited by conservation of

energy and angular momentum. Thus, the magnetron oscillation describes a metastable motion around an electrostatic potential hill in the radial plane.

---

[5] In the quantum picture it reads $E = \left(n_z + \frac{1}{2}\right)\hbar\omega_z + \left(n_+ + \frac{1}{2}\right)\hbar\omega_+ - \left(n_- + \frac{1}{2}\right)\hbar\omega_- \pm g\frac{\mu_B B}{2}$. Nevertheless, a classical treatment is legitimate since even for effective particle temperatures of $T = 2E/k_B \approx 4\text{K}$ the typical quantum numbers exceed $n > 10^5$.

Relativistic Corrections

Until now the ion motion was treated in the non-relativistic limit. Frequency shifts caused by special relativity can be intuitively understood in terms of a relativistic increase of the ion mass [6]. Using relation (3.5) the dominant contribution to the relativistic frequency shift of the free cyclotron frequency can be approximated by considering that the ion velocity is dominated by the fastest eigenmotion which (for a typical frequency hierarchy) is the reduced cyclotron mode:

$$\frac{\Delta\omega_c}{\omega_c} = -\frac{\Delta m}{m} = -\frac{m(\gamma-1)}{m} \approx -\frac{v^2}{2c^2} \approx -\frac{E_+}{mc^2}. \tag{3.17}$$

Here γ represents the Lorentz factor with $\gamma = 1/\sqrt{1-v^2/c^2} \approx (1 + v^2/2c^2 + ...)$. Although equation (3.17) is decreasing for massive HCI, which are the main measurement objects of ALPHATRAP, in general an optimization of the measurement precision requires to keep the ion energy/amplitude as small as possible. This holds especially for the reduced cyclotron mode.

Furthermore, apart from the free cyclotron frequency, for the final determination of the g-factor via a measurement of the frequency ratio $\Gamma = \frac{\omega_L}{\omega_c}$ (as introduced in chapter 3.1), the relativistic shift of the Larmor frequency of the bound electron has also to be taken into account. This can be approximated by [83, 84]:

$$\frac{\Delta\omega_L}{\omega_L} \approx (1-\gamma)\frac{\omega_c}{\omega_L} = \frac{\Delta\omega_c}{\omega_c}\frac{\omega_c}{\omega_L}. \tag{3.18}$$

Thus, compared to the free cyclotron frequency the relative shift of the Larmor frequency is suppressed by several orders of magnitude (e.g. $\omega_L/\omega_c \approx 4445$ for $^{208}\mathrm{Pb}^{81+}$) and consequently both shifts do not cancel in the final measurement of Γ.

3.2.3 Imperfections of a Real Penning-Trap

Of course, the practical implementation of an ideal Penning-trap is not feasible. In reality a finite electrode size, finite machining precision, alignment errors and other imperfections will always give rise to deviations from the ideal trapping field configuration, resulting in systematic frequency shifts of the associated particle motion. Nevertheless, within the required precision, a good approximation can be achieved by combining modern precision manufacturing techniques with a thoughtful experimental design and a detailed analysis of its limitations. In the following some important characteristics of a real Penning-trap are discussed.

---

[6] However, in general this simple picture is not equally accurate for the individual relativistic eigenfrequency shifts. A full perturbative treatment in first-order can be found in [82].

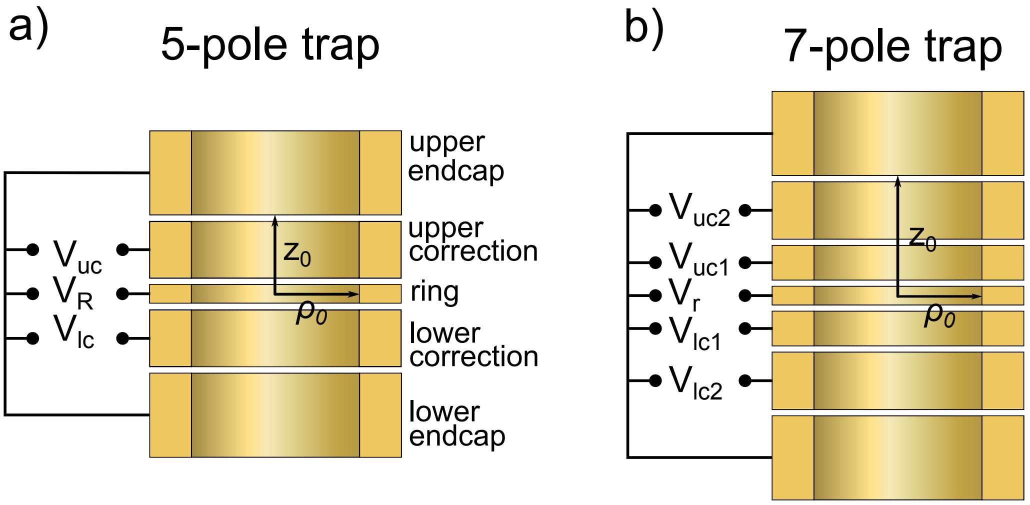

Figure 3.4: Side cut view of simplified cylindrical Penning-traps. A geometrically optimized trap can be tuned to high harmonicity ("compensated") by applying a suitable voltage to the correction electrodes (for details see text). Compared to a "classical" 5-pole trap, a 7-pole design which include two sets of correction electrodes allows to compensate for even higher order anharmonic field components. Typically the upper (u) and lower(l) electrodes are supplied with symmetrical (equal) voltages. Asymmetric voltages are applied in order to axially shift the ion position or during particle transport within a multi trap system.

The Cylindrical Penning-Trap and Electrostatic Anharmonicities

Besides the hyperbolic also a cylindrical Penning-trap of suitable inner dimensions equipped with additional correction electrodes enables a good approximation of the required harmonic[7] quadrupole potential in a finite volume near the trap center [85]. The cylindrical design is especially well suited for multi trap systems since the ring shaped electrodes can be directly stacked. This allows for an easy ion injection and transport within the trap tower. Furthermore, the open setup also enables the manipulation of the confined ion by microwave and laser irradiation from the outside (4). A cylindrical 5-pole trap is shown in figure 3.4a. Even higher harmonicities are achievable with a 7-pole configuration (figure 3.4b). Both types are used at the ALPHATRAP experiment (chapter 4.7).
Assuming perfect cylinder-symmetry [8], the harmonicity of a Penning-trap with specific dimensions can be characterized by a multipolar expansion of the corresponding

---

[7] The conditions for the harmonicity of the trapping field increase with the motional amplitude or temperature of the particle. For small amplitudes there is a number of different geometries which in first order are sufficiently harmonic.

[8] Here only the dominant cylinder symmetric imperfections are considered. In reality, deviations from cylinder symmetry are inevitable, especially because some electrodes have to be radially split in order to enable radial excitation and detection of the particle.

electrostatic Potential [79]:

$$\Phi(r,\theta) = \frac{V_r}{2}\sum_{n=0}^{\infty} C_n \left(\frac{r}{d}\right)^n P_n(\cos(\theta)), \tag{3.19}$$

where P_n are Legendre polynomials of order n, $r = \sqrt{\rho^2 + z^2}$ and $\cos(\theta) = \frac{z}{r}$. Again the characteristic trap length d is given by the inner dimensions of the trap (figure 3.4) according to equation (3.7). The potential shape and its influence on the particle motion is defined by the expansion coefficients C_n (where $C_n = 0$ for $n \neq 2$ yields the desired quadrupole part). Typically odd numbered coefficients only matter if strong deviations from the axial mirror symmetry are present. Otherwise they can be neglected. The monopolar contribution ($n = 0$) is a constant potential offset and does not affect the particle motion. Thus, the important anharmonic contributions are represented by the even numbered coefficients (C_4, C_6, C_8...). These are associated with typically undesired systematic shifts of the particles eigenfrequencies which depend on the particle oscillation amplitudes. The first order frequency shifts induced by the even numbered terms are calculated in [86]. For example, the effect of the leading anharmonic contribution C_4 is given by

$$\frac{\Delta\omega_z}{\omega_z} = \frac{C_4}{C_2}\frac{3}{4d^2}\left({a_z}^2 - 2{a_+}^2 - 2{a_-}^2\right) \tag{3.20}$$

$$\frac{\Delta\omega_+}{\omega_+} = -\frac{C_4}{C_2}\frac{3}{2d^2}\frac{\omega_-}{\omega_+ - \omega_-}\left(2{a_z}^2 - {a_+}^2 - 2{a_-}^2\right) \tag{3.21}$$

$$\frac{\Delta\omega_-}{\omega_-} = \frac{C_4}{C_2}\frac{3}{2d^2}\frac{\omega_+}{\omega_+ - \omega_-}\left(2{a_z}^2 - {a_-}^2 - 2{a_+}^2\right), \tag{3.22}$$

where a_z, a_+, a_- denote the mode oscillation amplitudes. In general such shifts can be minimized by cooling the ion to small oscillation amplitudes while keeping the anharmonic contributions as small as possible. The latter can be achieved by a thorough trap design. The C_n coefficients are defined by the inner trap dimensions and the applied electrode voltages. For a cylindrical **5-pole trap** the C_n coefficients can be decomposed into:

$$C_n = {C_n}^0 + D_n \cdot TR \quad \text{with} \quad TR = \frac{V_c}{V_r}, \tag{3.23}$$

where the so called *tuning ratio* TR is defined as the ratio of the applied correction electrode voltage V_c and the ring voltage V_r. The geometry dependend parameter D_n quantifies the effect of an applied correction electrode voltage for $V_c \neq 0$.
Correspondingly, in case of a **7-pole trap** (with two pairs of correction electrodes) two tuning ratios $TR_1 = \frac{V_{c1}}{V_r}$ and $TR_2 = \frac{V_{c2}}{V_r}$ may be defined such that:

$$C_n = {C_n}^0 + D_{n1} \cdot TR_1 + D_{n2} \cdot TR_2 \tag{3.24}$$

Apart from the electrode dimensions the *tuning ratio(s)* are additional optimization parameters which can be in situ adjusted in order to cancel dominant anharmonic contributions. In this context two important operation conditions called *orthogonality* and *compensation*, can be achieved **simultaneously:**

- **Orthogonality:** For the 5-pole trap design the electrode dimensions [9] can be chosen such, that $D_2 = 0$ which is called *orthogonality* and physically means that $\frac{d\omega_z}{dTR} = 0$ (due to equation 3.13).
  For a 7-pole trap the "double orthogonality" condition $D_{21} = D_{22} = 0$ can't be met simultaneously. Instead the "combined orthogonality" criterion ${D_2}^{comb} \equiv D_{21} \cdot TR_1 + D_{22} \cdot TR_2 = 0$ has to be fulfilled. Effectively this defines a correction voltage ratio $\frac{V_{c1}}{V_{c2}} = const.$
- **Compensation:** In a compensated 5-pole trap the dominant anharmonic coefficients C_4 and C_6 simultaneously vanish for a specific tuning ratio. Additionally, a 7-pole trap also allows to cancel the C_8 and the C_{10} terms.

Although the necessary dimensions as well as the optimal tuning ratio can be readily calculated in advance, in reality there will always be small deviation from the ideal potential e.g. caused by manufacturing tolerances. Therefore, the final optimization is performed experimentally by minimizing the observed axial frequency shift between a cold and an excited ion via an optimization of the *tuning ratio.* During this procedure orthogonality is a very useful property since it makes the axial frequency independent of the applied *tuning ratio.*

Image Charge Shift

In the previous considerations the influence of the ion on the electrostatic trapping field was not considered. It is known that a charged object which is in close proximity to a conductive surface leads to a redistribution of the surface charge density. In a Penning-trap these so called image- or mirror charges can be exploited for ion detection as will be discussed in section 3.2.4. However, the image charge also leads to a modification of the effective trapping potential, which results in a parasitic shift of the radial eigenfrequencies[10]. For a cylindrical Penning-trap the *image charge shift* can be approximated[11] by [87, 23]:

$$\Delta\omega_\pm = \mp \frac{1}{8\pi\epsilon_0} \frac{q^2}{m\omega_c r^3}. \tag{3.25}$$

which by using the invariance theorem translates into a relative cyclotron frequency shift of

$$\frac{\Delta\omega_c}{\omega_c} \approx \frac{1}{8\pi\epsilon_0} \frac{m}{r^3 B^2}, \tag{3.26}$$

---

[9] For a 5-pole trap these are the trap radius r and the length of the correction and ring electrode l_c and l_r. For a 7-pole trap the length of the second correction electrode pair is a fourth geometric degree of freedom.

[10] Because of the axial symmetry of the problem the axial mode is not affected.

[11] Here the calculation is carried out by modeling the trap as an infinite uniform cylinder [87].

where r denotes the inner trap radius. In the Mainz Experiment the image charge shift constituted the leading systematic uncertainty [83]. For this reason and because the shift is especially problematic when dealing with heavy ions, the ALPHATRAP experiment features an improved trap design with increased trap radius r (see chapter 4).

Magnetic Field Imperfections

In Penning-trap experiments the necessary strong homogeneous magnetic field is typically generated by a superconducting magnet. Usually this does not just contain a single superconducting solenoid but is equipped with a number of individually controllable "shimming" coil configurations. In principle these allow to tune the internal field within a finite volume close to perfect homogeneity. However, inside the experimental setup and its close proximity the use of magnetically susceptible materials can't be completely avoided, which can cause a considerable field distortion. In analogy to the electrostatic potential the magnetic field homogeneity can be characterized by a series expansion around the trap center. Up to the second order it is given by:

$$\boldsymbol{B}(\rho, z) = B_0\boldsymbol{e_z} + B_1\left(z\boldsymbol{e_z} - \frac{1}{2}\rho\boldsymbol{e_\rho}\right) + B_2\left(\left(z^2 - \frac{1}{2}\rho^2\right)\boldsymbol{e_z} - z\rho\boldsymbol{e_\rho}\right), \tag{3.27}$$

Already the linear term (B_1) can cause[12] undesired frequency shifts. This can be intuitively understood by considering that the radial eigenmotions of the charged particle are associated with circular currents $I_\pm = \frac{q\omega_\pm}{2\pi}$ and therefore carry the axial orbital magnetic moment

$$\mu_z^{orb} = -I_+\pi {a_+}^2 - I_-\pi {a_-}^2 \tag{3.28}$$

$$= -\frac{q}{2}\left(\omega_+ a_+^2 + \omega_- a_-^2\right). \tag{3.29}$$

In the axial linear gradient the magnetic moment experiences a constant force $F_z = \mu_z^{orb} B_1$ which axially shifts the center of the ion motion within the magnetic field gradient. As a consequence the cyclotron frequency changes according to [88]:

$$\frac{\Delta\omega_+}{\omega_+} \approx -\frac{1}{2}\left(\frac{B_1}{B_0}\right)^2\left(\left(\frac{\omega_+}{\omega_z}\right)^2 - \frac{1}{2}\right)a_+^2. \tag{3.30}$$

Typically, the dominant inhomogeneity is given by the last quadratic term in equation 3.27 which is called a magnetic bottle. Inside the magnetic bottle the particle experiences a decrease/increase of the axial magnetic field in radial/axial direction, respectively. This is also associated with particle energy/amplitude dependent shifts

---

[12] a second order effect

of the eigenfrequencies given by [86]

$$\begin{aligned}
\frac{\Delta\omega_z}{\omega_z} &= \frac{B_2}{4B_0}\frac{\omega_+ + \omega_-}{\omega_+\omega_-}\left({a_-}^2\omega_- + {a_+}^2\omega_+\right) && (3.31)\\
\frac{\Delta\omega_+}{\omega_+} &= \frac{B_2}{2B_0}\frac{\omega_+ + \omega_-}{\omega_+ - \omega_-}\left[{a_z}^2 - {a_+}^2 - {a_-}^2\left(1 + \frac{\omega_-}{\omega_+}\right)\right] && (3.32)\\
\frac{\Delta\omega_-}{\omega_-} &= -\frac{B_2}{2B_0}\frac{\omega_+ + \omega_-}{\omega_+ - \omega_-}\left[{a_z}^2 - {a_+}^2\left(1 + \frac{\omega_+}{\omega_-}\right) - {a_-}^2\right]. && (3.33)
\end{aligned}$$

It is worth noting, that in the magnetic bottle the Larmor frequency experiences the same relative shift as the modified cyclotron frequency. Interestingly, apart from the Larmor- and radial frequencies also the axial frequency is shifted, although it does not explicitly depend on the magnetic field (see equation (3.13)). This is because in the magnetic bottle the ion's orbital magnetic moment μ_z experience a force $F_z = 2\mu_z B_2 z$ which linearly depends on the axial position of the ion. Therefore the axial equation of motion (3.8) is modified to:

$$m\ddot{z} = -\left(\frac{qV_rC_2}{d^2} - 2\mu_z^{orb}B_2\right)z \qquad (3.34)$$

with

$$\omega_z^{'} = \left(\underbrace{\frac{qV_rC_2}{d^2m}}_{\omega_z^2} - \frac{2\mu_z^{orb}B_2}{m}\right)^{\frac{1}{2}} \approx \omega_z\left(1 - \frac{\mu_z^{orb}B_2}{m\omega_z^2}\right). \qquad (3.35)$$

Thus the relative shift of the axial frequency is:

$$\frac{\Delta\omega_z}{\omega_z} = \frac{\mu_z^{orb}B_2}{m\omega_z^2}. \qquad (3.36)$$

By inserting equation (3.29) into (3.36) and making use of relation (3.13) and (3.14) one finally arrives at equation (3.31). In general the magnetic bottle term and the associated systematic frequency shifts can impose a major limitation during a high-precision measurement of the free cyclotron frequency. Nevertheless, the underlying effect described by equation (3.36), i.e. the coupling of the axial frequency to a magnetic moment, has some essential applications for our experiment. In particular it enables a direct detection of the electron's spin orientation as will be discussed in section 3.2.6. Another application is the measurement of the cyclotron energy (radius) via the axial frequency.

Field Drifts

Apart from static deviations the trapping fields are also subjected to dynamic variation over time. In case of the electric field these are mainly caused by temporal fluctuations of the supply voltage but also by internal and external disturbance. Such fluctuations can be greatly reduced by dedicated ultra-stable voltage sources combined with a well-shielded detection system with ultra-low noise characteristics (see chapter 5). There are several reasons for magnetic field drifts including temperature and pressure dependent mechanical relaxation processes and susceptibility changes of internal and external components. Apart from that a certain gradual magnetic field drift is usually observable during the settling time of a newly energized superconducting magnet. Within the first 13 hours after charging the ALPHATRAP magnet showed an initial relative field drift of $\sim 5.7 \cdot 10^{-8}$ per hour.

Alignment Errors and the Invariance Theorem

Despite high-precision manufacturing techniques and an elaborate mechanical design, in a real Penning-trap experiment a certain relative misalignment (tilt) between the magnetic field direction and the symmetry axis of the trap can't be avoided. This is associated with a coupling and a dominant systematic shifts of the ideal eigenfrequencies $(\omega_+,\, \omega_z,\, \omega_- \rightarrow \omega_+^*,\, \omega_z^*,\, \omega_-^*)$. In this context, it is remarkable that the simple relation already introduced in chapter 3.2.1 as the *invariance theorem* does also apply for the corresponding shifted frequencies as shown in [81]:

$$\omega_c{}^2 = \omega_+^{*\,2} + \omega_z^{*2} + \omega_-^{*\,2}. \tag{3.37}$$

In contrast to equation (3.14) the *invariance theorem* is not influenced by systematic errors arising from field tilts and even holds for elliptic deformations of the radial electrostatic potential [81] [13]. In this way the Invariance theorem is crucial for the precise final determination of the free cyclotron frequency and consequently the g-factor via the experimental approach introduced in section 3.1.
The invariance theorem implies the following dependency on the individual measurement uncertainties of the three eigenfrequencies ω_i with $i \in \{+, z, -\}$:

$$\left(\frac{\delta\omega_c}{\omega_c}\right)_i = \left(\frac{\omega_i}{\omega_c}\right)^2 \frac{\delta\omega_i}{\omega_i}. \tag{3.38}$$

Thus, considering the typical hierarchy of frequencies (given by equation 3.12), the final relative uncertainty of the free cyclotron frequency is mainly determined by the relative measurement uncertainty of the modified cyclotron frequency ω_+, while the uncertainty contribution of the axial- and magnetron frequency are suppressed by several orders of magnitude [14].

3.2.4 Ion Detection Principle

As already mentioned one important part of a g-factor measurement is the precise determination of the free cyclotron frequency ω_c. Since ω_c is not a fundamental

---

[13] In the reverse argument this enables a measurement of the alignment angle [81]

[14] Actually, this is true for direct frequency measurements. In general the correlation of the individual uncertainties and their combined effect on the total uncertainty of ω_c depends on the measurement process.

Penning-trap frequency it has to be derived from the three eigenfrequencies (via the invariance theorem) which therefore have to be measured individually. This can be achieved by the non-destructive detection of tiny image currents which are induced into the conducting trap electrodes as a consequence of the ion motion [89].

Effective Electrode Distance

In the intuitively accessible case of a charged particle undergoing a harmonic axial oscillation $z(t) = a_z \sin(\omega_z t + \varphi)$ between the two radially extended plates of an ideal capacitor, the frequency information is stored in the induced current signal which is given by [90]:

$$I_{\text{ind}}(t) = \frac{q}{D}\dot{z}(t) = \frac{q}{D}\omega_z a_z \cos(\omega_z t + \varphi), \tag{3.39}$$

where D denotes the distance between the capacitor plates. This relation can be similarly adopted for any other electrode configuration such as a Penning-trap. Under the assumption of small ion oscillation amplitudes the electric potential at the position of the ion can be linearly approximated by

$$\Delta V(z)|_{z_{ion}} \approx \frac{\partial V}{\partial z}|_{z_{ion}} \cdot z = -E_{z_{\text{ion}}} \cdot z, \tag{3.40}$$

which allows to define the so called *effective electrode distance*

$$D_{\text{eff}} = \frac{V_{\text{test}}}{E_{z_{\text{ion}}}}, \tag{3.41}$$

where $E_{z_{ion}}$ represents the electric field at the ion's position[15] when a test voltage V_{test} is applied to a predefined signal pickup electrode while the other electrodes are set to ground potential. In this way, D_{eff} represents a trap-geometry dependent coupling parameter for the interaction between the particle and the trap where the induced current depends on the distance and size of the chosen pickup electrode.

Bolometric Ion Detection

Typically, even for HCI the induced image current does not exceed a few femtoampere. For example, in our large Precision Trap with D_{eff} =2.93 cm the axial oscillation (with $\omega_z = 2\pi\cdot 651\,\text{kHz}$) of a single $^{208}\text{Pb}^{81+}$ ion which is cooled to ~4 K, would induce a current of

$$I_{\text{rms}} = \frac{q\omega_z a_z}{D_{eff}\sqrt{2}} \approx 25.6\,\text{fA} \quad \text{with} \quad a_z \approx \sqrt{\frac{2k_B T}{m\omega_z^2}} \approx 4.4\,\mu\text{m}. \tag{3.42}$$

---

[15] Assuming that the ion is not present.

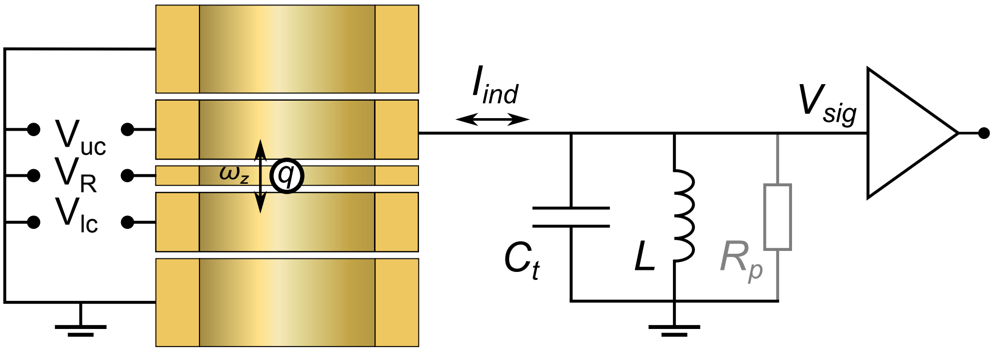

Figure 3.5: Simplified axial detection circuit. In this example the induced current signal I_{ind} is picked up from the upper correction electrode. To prevent a short circuit of the signal, the trap voltages are typically supplied via large blocking resistors which are not shown here (see chapter 5). The total capacitance C_t comprises all detector input related stray capacitances (electrode-, coil-, amplifier- and cable capacitances). The equivalent parallel resistance R_p represents the total losses of the tuned circuit (see text). The amplifier increases the signal amplitude but also decouples the tuned circuit from the low impedance signal transmission lines. In principle the resonant ion detection circuit resembles very much a simple radio receiver which is listening to the broadcast of the oscillating ion.

The detection and measurement of this tiny current signal essentially relies on Ohm's law. To this end the induced current I_{ind} is picked up and converted into a detectable signal voltage

$$\mathrm{V}_{sig} = I_{ind} \cdot Z(\omega_i) \tag{3.43}$$

across the input impedance Z of a cryogenic detector circuit. The detector is based on a parallel tank circuit (resonator), which is tuned close to the the ion's oscillation frequency ω_i and a solid state amplifier which allows recording the detected signal (figure 3.5).

The tank circuit allows to maximize the detector's input impedance (and thus the signal voltage) by compensating the parasitic capacitance of the respective pickup electrode[16] with a dedicated parallel coil-inductance L. The combined circuit and component losses can be modeled by an equivalent parallel resistance R_p (see chapter 5). Thus, the total impedance of the resonator circuit can be written as

$$Z_{Res}(\omega) \approx \left(\frac{1}{R_p} + i(\omega C - \frac{1}{\omega L})\right)^{-1} = \left(\frac{1}{R_p} + i(\frac{\omega}{\omega_r^2 L} - \frac{\omega_r^2 C}{\omega})\right)^{-1}. \tag{3.44}$$

---

[16] Actually the total capacitance of the resonator circuit is a composition of several parasitic capacitances including the trap capacitance, the intrinsic coil and amplifier capacitance and other parasitic cable capacitances.

At it's resonance frequency $\omega_r \approx \frac{1}{\sqrt{LC}}$[17] the resonator's inductive and capacitive reactances cancel each other out and the maximal impedance (and signal) is reached given by the real equivalent parallel resistance

$$Z(\omega_r) = R_p^r = Q\omega_r L. \tag{3.45}$$

The dimensionless quality factor Q of a damped oscillator is defined as the ratio of the total stored energy to the energy loss per oscillation cycle times 2π. It is related to the resonators damping constant via $\delta_r{=}\omega_r/2Q$.
After a fast fourier transformation (FFT) a "hot" ion, which is not yet in thermal equilibrium with the detector, appears as a coherent signal peak in the detector's thermal noise spectrum [91, 92]

$$V_n(\omega) = \sqrt{4k_B T \Re(Z(\omega))\Delta\nu}, \tag{3.46}$$

where $\Delta\nu$ denotes the frequency resolution bandwidth.

Detector-Ion Interaction Due to the signal voltage drop across the detector impedance (3.43), ions experience a reactive force

$$F \approx -q\frac{Z(\omega_i)\cdot I_{ind}}{D_{eff}} \tag{3.47}$$

which adds a damping term to the equation of motion according to

$$\ddot{z} = -\frac{qV_rC_2}{md^2}z - \underbrace{\frac{q_i^2 Z(\omega_i)}{mD_{eff}^2}}_{2\gamma}\dot{z}. \tag{3.48}$$

Here it must be noted that γ is a complex damping constant. This has two important consequences for the ion motion:

- **Resistive Cooling**: The real part of the detector's input impedance is responsible for an exponential damping of the ion energy with the so called *cooling time constant.*

  $$\tau = \frac{mD_{eff}^2}{q^2\Re(Z(\omega))}. \tag{3.49}$$

  The resisitive cooling is most effective when the ion is in resonance with the detector.

---

[17] The Thomson formula is only exact for an ideal tuned circuit. If damping effects are taken into account the resonance frequency is modified according to $\omega \approx \omega_r\sqrt{1-1/2Q}$. Thus, already for a resonator with $Q = 100$ the correction is smaller then 1%.

- **Image Current Shift** : Due to the interaction with the imaginary part[18] of the detector impedance, the ion frequency is shifted according to[19] [93]

$$\Delta\omega_i^{IC} = \frac{\delta_r \delta_i}{4} \frac{\omega_i - \omega_r}{(\omega_i - \omega_r)^2 + \delta_r^2/4}, \tag{3.50}$$

  where δ_r and δ_i are the resonator's and ion's damping constant respectively with $\delta_i = 1/\tau(\omega_r)$. The term $(\omega_i - \omega_r)$ denotes the detuning of the ion- and resonator frequency. From (3.50) it follows that for a given detuning the ion frequency is pushed away with respect to the resonator center. For this reason the *image current shift* is sometimes referred as frequency pulling/pushing. The *image current shift* should not be confused with the *image charge shift* (introduced in section 3.2.3) which is a direct consequence of the ion interaction with the metallic trap electrodes and does not dependent on the connection or the properties of a detector circuit.

Thermalized Ion Detection

In principle, the interaction between the ion and the resonator can be intuitively understood from linear circuit theory by modeling the ion as a series LC circuit. To this end the damped equation of motion (3.48) can be rewritten in terms of the induced current given by equation (3.39):

$$\frac{mD_{eff}^2}{q^2}\ddot{I} + Z(\omega_i)\dot{I} + \frac{m\omega_i^2 D_{eff}^2}{q^2} I = 0. \tag{3.51}$$

By comparing this with the differential equation of a series tuned circuit

$$L\ddot{I} + R\dot{I} + \frac{1}{C}I = 0 \tag{3.52}$$

the equivalent lumped circuit parameters of the ion can be identified as:

$$L_{ion} = \frac{mD_{eff}^2}{q^2}, \quad R = Z(\omega_i), \quad C_{ion} = \frac{q^2}{m\omega_i^2 D_{eff}^2}. \tag{3.53}$$

From this the total impedance of the equivalent circuit of the ion and the resonator as shown in figure 3.6 can be calculated

$$Z_{tot} = \left(\underbrace{\frac{1}{R_p} + i(\frac{\omega}{\omega_r^2 L} - \frac{\omega_r^2 C}{\omega})}_{Z_{Res}^{-1}} \underbrace{-i\left(\frac{\omega}{\omega_i^2 C_{ion}} - \frac{\omega_i^2 L_{ion}}{\omega}\right)^{-1}}_{Z_{ion}^{-1}} \right)^{-1}. \tag{3.54}$$

---

[18] In general the real part causes a negligible frequency shift.

[19] This applies for the weak coupling regime, i.e. when the induced ion damping is small compared to the damping of the Resonator.

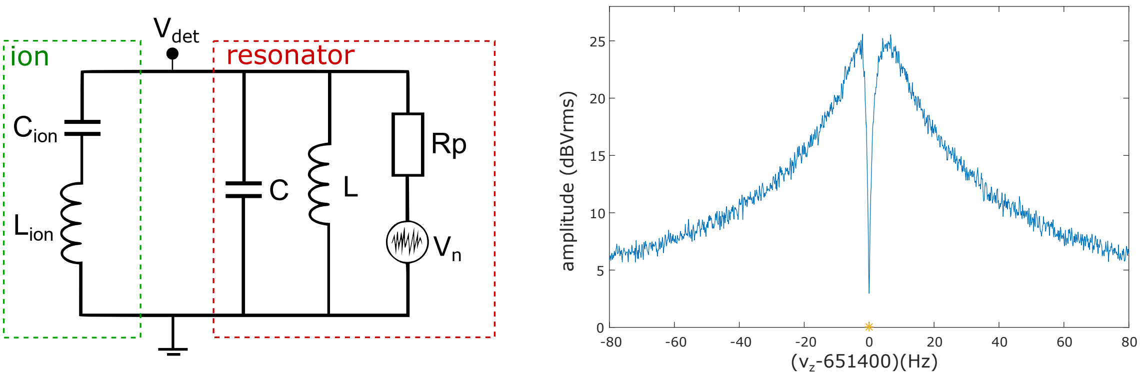

Figure 3.6: Left side: Equivalent lumped circuit model of ion and resonator. The ion can be modeled as a series LC circuit (see text) which shortens the resonator impedance at the ion's eigenfrequency. The detected thermal noise is generated by the real part of the total impedance of the equivalent circuit (see text). Right side: Typical noise spectrum of a single Ar^{13+} ion which is in thermal equilibrium with the axial PT detector. Modified from [76].

Since a series LC circuit has it's minimum impedance at it's resonance frequency, an ion which is in thermal equilibrium with the detector effectively shortens [20] the detector impedance at the ion's oscillation frequency ω_i. Thus, it appears as a sharp dip feature in the total thermal noise spectrum $V_n(\omega) = \sqrt{4k_B T \Re(Z_{tot}(\omega))\Delta\nu}$. In resonance with the detector the dip can be characterized by it's 3dB linewidth (dipwidth) [94]

$$\delta\nu_{dip} = \frac{N}{2\pi}\frac{1}{\tau} = \frac{N}{2\pi}\frac{q^2 R_p}{m D_{eff}^2}, \tag{3.55}$$

which can be used to determine the number N of identical ions stored in the trap. Measuring the eigenfrequency of a thermalized ion of mass m and charge q via the incoherent dip technique has the advantage of small oscillation amplitudes and is consequently less affected by systematic frequency shifts due to trap imperfections. Nevertheless, a drawback of this method is that the measurement uncertainty scales with the dip width, which is especially problematic when dealing with highly charged ions.

3.2.5 Ion Excitation and Sideband Coupling

The motion of an ion in a Penning-trap can be accurately controlled by applying suitable radio frequency excitations to one or more predefined trap electrodes. In the following two important excitation techniques are introduced which are frequently used at the ALPHATRAP experiment.

---

[20] The ion's amplitude and phase are opposed to the incoherent noise in order "not to be excited".

Dipole Excitation

A dipole excitation is a purely temporal variation of one component of the electric trapping field. It can be used to individually excite the three independent ion eigenmotions at their corresponding resonance frequencies. For example, a dipole excitation of the axial frequency can be realized by connecting an excitation signal (with amplitude V_{Dz} and frequency $\omega_{rf} \approx \omega_z$) to either a correction or an endcap electrode. In first order this creates the electric driving field

$$\mathbf{E}_{Dz}(t) = \frac{V_{Dz}}{D_{eff,z}} \sin(\omega_{\mathrm{rf}} t + \Phi_{\mathrm{rf}}) \begin{pmatrix} 0 \\ 0 \\ 1 \end{pmatrix}, \tag{3.56}$$

where $D_{eff,z}$ denotes the effective electrode distance of the respective excitation electrode. Analogously, a dipolar excitation of the radial vibrational modes requires a radially directed driving field. This can be achieved by applying a separate excitation signal between the halfs of a vertically[21] bisected/split ring electrode.

Dipolar excitations can be used for trap cleaning purposes e.g. by exciting unwanted ion species to high axial amplitudes and subsequently lowering the trapping potential. In general, with a dipolar excitations it is possible to imprint a certain amplitude and phase to an eigenmotions which is especially important for coherent peak- and phase detection techniques.

Quadrupole Excitation

While a dipolar excitation is specifically addressing individual eigenmodes of the ion motion, an excitation in a quadrupolar field configuration enables a coupling and energy/action exchange between two otherwise independent eigenmodes. A quadrupole excitation generally involves an electric field variation in time and space. For example, the very frequently used coupling between the axial and a radial mode is typically realized by applying an excitation signal to a vertically split correction electrode. This creates a tilted electric driving field along the xz-direction:

$$\mathbf{E}_{Qxz}(t) = \frac{V_{Qxz}}{D^2_{eff,xz}} \sin(\omega_{\mathrm{rf}} t + \Phi_{\mathrm{rf}}) \begin{pmatrix} z \\ 0 \\ x \end{pmatrix}. \tag{3.57}$$

A coupling between the axial and one of the radial modes generally requires the excitation signal frequency ω_{rf} to be tuned (close) to one of the sideband frequencies $(\omega_+ \mp \omega_z)$ or $(\omega_z \mp \omega_-)$. The equations of motion describing the dynamics of two coupled modes in a Penning-trap are similar to those of a driven two-level system in quantum mechanics [95]. A detailed discussion can be found in [79, 96].

Depending on which sidebands are used for coupling one can distinguish between the following important applications.

---

[21] Vertically here means, that the cut is made along the rotational symmetry axis of the electrode.

Sideband Cooling and Radial Mode Detection At the "red" sideband frequencies $\omega_{rf} = (\omega_z + \omega_-)$ and $\omega_{rf} = (\omega_+ - \omega_z)$ the respective modes undergo an amplitude modulation of the form [95]

$$z(t) = a_z \sin\left(\frac{\Omega}{2}t\right) \sin(\omega_z t + \Phi_z) \tag{3.58}$$

$$r_\pm(t) = a_\pm \cos\left(\frac{\Omega}{2}t\right) \sin(\omega_\pm t + \Phi_\pm). \tag{3.59}$$

The energy transfer rate of these Rabi-like oscillations is given by the double modulation frequency (Rabi frequency) [95, 96]

$$\Omega = \frac{qV_{Qxz}}{2mD_{eff,xz}\sqrt{\omega_z\omega_\pm}}. \tag{3.60}$$

By using sideband coupling it is possible to dissipate excessive energy in the radial modes via the axial tank circuit[22]. While the sideband drive $\omega_{rf} = (\omega_z + \omega_-)$ or $\omega_{rf} = (\omega_+ - \omega_z)$ is applied, the corresponding thermal averaged[23] mode quantum numbers approach an equilibrium state with $\langle n_z \rangle = \langle n_- \rangle$ or $\langle n_z \rangle = \langle n_+ \rangle$ respectively. Consequently, the so called cooling limit of the associated averaged mode energies/temperatures can be derived [79]:

$$\langle E_\pm \rangle = \pm\hbar\omega_\pm \left(\langle n_\pm \rangle + \frac{1}{2}\right) = \pm\frac{\omega_\pm}{\omega_z}\hbar\omega_z \left(\langle n_z \rangle + \frac{1}{2}\right) = \pm\frac{\omega_\pm}{\omega_z} \langle E_z \rangle . \tag{3.61}$$

Sidebandcooling is especially important for the metastable magnetron motion. Since the magnetron mode energy is negative, a "conventional" i.e. dissipative process, as resistive cooling (introduced in 3.2.4) would increase the magnetron radius and eventually lead to particle loss. In contrast, sidebandcooling decreases the magnetron radius by adding energy and thus pushing the particle on top of the repulsive radial potential hill [79]. In this way, the term "cooling" can be misleading since it here refers to the reduction of the particle oscillation amplitude/radius.

Double-dip Detection of the Radial Modes Apart from sideband cooling, the "red" sideband frequencies $\omega_{rf} = (\omega_z + \omega_-)$ and $\omega_{rf} = (\omega_+ - \omega_z)$ can also be used to determine the radial mode frequencies with only a single axial detector circuit. In the following this will be discussed exemplarily for the detection of the reduced cyclotron mode.

The coupled axial motion given by equation (3.58) implies a splitting of the single axial dip feature into two neighboring dips (double-dip) at the (left and right) frequencies $\omega_{l,r} = \omega_z \mp \Omega/2$. In analogy to Rabi oscillations in quantum mechanics, a certain detuning from the ideal (resonant) coupling frequency with

---

[22] Naturally, this is most effective when the axial mode is in resonance with the axial tank circuit.

[23] As already noted the axial resonator represents a thermal reservoir. Thus, during sideband coupling not only the axial- but also the radial mode energies are thermally distributed [79].

$$\delta = \omega_{rf} - (\omega_+ - \omega_z), \tag{3.62}$$

leads to a modification of the Rabi frequency [95, 96]:

$$\Omega' = \sqrt{\Omega^2 + \delta^2}. \tag{3.63}$$

Consequently, also the double-dip frequencies are shifted according to a classical avoided crossing [95, 96]:

$$\omega_{l,r} = \omega_z - \frac{1}{2}(\delta \pm \Omega'). \tag{3.64}$$

By combining equations (3.62) and (3.64) it is possible to extract the reduced cyclotron frequency by measuring the double-dip frequencies if simultaneously the axial frequency is known

$$\omega_+ = \omega_{rf} - \omega_z + \omega_l + \omega_r. \tag{3.65}$$

Correspondingly, by using a coupling drive with $\omega_{rf} = (\omega_z + \omega_-)$, the magnetron frequency can be determined via

$$\omega_- = \omega_{rf} + \omega_z - \omega_l - \omega_r. \tag{3.66}$$

During the averaging time of a double-dip measurement the axial frequency is subjected to systematic drifts caused by fluctuations of the trapping voltage. For this reason the axial frequency is typically determined from the average of two separate measurements, taken before and after the double-dip measurement. An alternative way is to use a "toothed" measuring sequence as describe in [88, 95].

Coherent Amplification and Phase Transfer When applying a quadrupole drive at the "blue" sideband frequencies $\omega_{rf} = (\omega_z - \omega_-)$ and $\omega_{rf} = (\omega_+ + \omega_z)$ both coupled modes are excited exponentially. Additionally, the motional phases of the excited modes now depend on the initial phases of the modes, i.e. before the coupling [23]. Actually, it is possible to transfer the phase information of one mode into the other (during excitation), an important feature of the advanced phase sensitive measurement technique "PnA" developed by Sven Sturm et al. [22].

3.2.6 Larmor Frequency Determination: Continuous Stern-Gerlach Effect

The famous Stern-Gerlach Experiment [97, 98] is considered to be the most directly observable manifestation of the discrete nature of quantum mechanics. In the original experiment the directional quantization of angular momenta was observed via the splitting of a beam of neutral, spin-carrying silver atoms in a magnetic field gradient. However, due to the additional deflection by the comparably strong Lorenz force it was not applicable for ions or charged particles [24]. This was resolved by Van Dyck, Schwinberg and Dehmelt [100, 101] in 1986 by introducing the Continuous Stern-Gerlach Effect (CSGE), a related technique for continuous spin state detection of single ions in a Penning-trap. The first observation of the Continuous Stern-Gerlach effect on a bound electron in an atomic ion was made by Nikolaus Hermanspahn et al. in 1999 [102].

In principle the CSGE makes use of the (generally unwanted) coupling of the axial frequency to a magnetic moment mediated by the magnetic bottle term of an imperfect magnetic trapping field. In chapter 3.2.3 the corresponding axial frequency shift due to the total orbital magnetic moment μ_z^{orb} of the ion was derived and is given by equation (3.35). When additionally considering the quantized electron spin magnetic moment $\mu_s = \pm\frac{g\mu_B}{2}$ the equation reads:

$$\omega_z^{'} \approx \omega_z \left(1 - \frac{B_2}{m\omega_z^2}\left(\mu_z^{orb} \pm \frac{g\mu_B}{2}\right)\right). \tag{3.67}$$

From this it can be seen that a transition between the two discrete spin states $\pm\frac{1}{2}$ (spin-flip) is associated with a shift of the axial frequency

$$\Delta\omega_z^{SF} = \frac{B_2 g\mu_B}{m\omega_z}. \tag{3.68}$$

This result opens up the possibility to determine the Larmor frequency with a spectroscopic method: To this end the spin transition can be interrogated (scanned) with a suitable radio frequency excitation (in our case in the millimeter waves regime), while the axial frequency indicates whether a transition was successful or not.

3.2.7 Double Trap Technique

From equation (3.68) it can be seen that for an efficient spin-flip detection a high B_2 term is favorable. However, this contradicts the requirement of a homogeneous magnetic field which is indispensable for a high-precision determination of the three fundamental trap frequencies and consequently the free cyclotron frequency. For this reason it is common practice to distribute the measurement process between two spatially separated traps (known as the double trap technique), which are appropriately optimized for their individual field of use. The precision measurement of the free cyclotron frequency as well as the spin-flip spectroscopy are carried out in the highly homogeneous magnetic field of a precision trap (PT). The spin state detection is performed in an analysis trap (AT). Here, the magnetic bottle term is purposely increased by using a ferromagnetic ring electrode. At ALPHATRAP (see chapter 4) the AT ring electrode is made out of a highly permeable cobalt-iron alloy which enables a strong magnetic bottle of $B_2 \approx 45\,000\,\mathrm{T/m^2}$. This is more than four times higher than in the predecessor g-factor experiment in Mainz ($B_2^{Mainz} \approx 10\,000\,\mathrm{T/m^2}$ [83]). Nevertheless, as can be seen from table 3.1, the detection of an axial frequency

---

[24] Actually, this is argued in [99].

jump is still challenging, especially when dealing with heavy, boronlike ions. In order to correctly identify the spin-flip induced frequency jumps the axial frequency must be kept sufficiently stable. On the one hand this imposes high demands on the ring voltage stability

$$\frac{\Delta V_r}{V_r} << 2\frac{\Delta\omega_z^{SF}}{\omega_z} \approx 10^{-6}. \tag{3.69}$$

On the other hand it is important to keep in mind that the strong magnetic bottle in the AT also increases the axial frequency dependence on the orbital magnetic moment. To prevent unwanted frequency drifts the radial mode energy (especially E_+) must be kept as constant as possible, which is challenging because of possible spurious noise signals appearing at the radial frequencies. In addition, the cyclotron heating rate (and thus the sensitivity to noise) increases with the average quantum number of the cyclotron mode [95, 103]. Therefore, next to adequate noise filtering, care must be taken that the radial modes, especially the reduced cyclotron mode, are sufficiently cold.

	$\Delta\omega_z^{SF}/2\pi$ (Hz)	
Ion	Mainz Experiment	ALPHATRAP
^{12}C^{5+}	0.58	3.1
^{28}Si^{13+}	0.24	1.3
^{40}Ar^{13+}	0.056	0.3
^{132}Xe^{53+}	n.a.	0.28
^{208}Pb^{81+}	n.a.	0.18
^{208}Pb^{77+}	n.a.	0.066

Table 3.1: Comparison of the calculated axial frequency shifts in the different analysis traps of the Mainz- and the ALPHATRAP experiment. The ALPHATRAP AT design is optimized for spin-flip detection of the heaviest HCI which are not accessible (n.a.) by the Mainz experiment. Even more demanding than hydrogen-like systems are measurements of boron-like HCI such as ^{208}Pb^{77+} since their Landé-g-factor and therefore the spin-flip induced shift is further reduced by about a factor of 3.

Measurement Process

In one g-factor measurement cycle the ion's free cyclotron frequency ω_c is measured in the PT while simultaneously the electron spin transition is being probed via a radio-frequency (millimeter wave) excitation ω_{mw} close to the expected Larmor frequency. Then the ion is transported to the AT where the spin state is analyzed and compared to the previous state (i.e. before the application of the spin excitation drive). Then the ion is transported back to the PT to initiate the next measurement cycle. This process is repeated multiple times for different excitation drives around the anticipated Larmor frequency. This results in a distribution of the spin transition probability as a function of the self consistent and time independent frequency ratio ω_{mw}/ω_c. A line shape fit to the distribution [83, 104] allows to extract the sought after gamma ration $\Gamma = \omega_L/\omega_c$ and consequently the g-factor via equation 3.3. More detailed information on the g-factor measurement scheme can be found in [83, 104, 105].

4 Experimental Setup

The ALPHATRAP experiment is largely based on it's predecessor g-factor experiment in Mainz. In the Mainz experiment the only possibility for the generation of HCI is in situ, via electron bombardement of a target material with a dedicated electron beam ion source (EBIS), which was part of the trap assembly (section 6.1). This constituted a major limitation in the generation of HCI with ionization energies higher than $\sim$5 keV. For this reason ALPHATRAP was planned in order to extend the range of accessible systems to the high Z regime. In this regard the major difference to the Mainz experiment is the access to potent external ion sources as the large cryogenic Heidelberg EBIT [106] which is capable of ionization energies on the order of 100 keV. Furthermore, the possibility to build the whole experiment from scratch allowed to incorporate already approved techniques together with new design ideas. This chapter serves to introduce the general experimental setup and elaborate on important components of the ALPHATRAP experiment. In this context it also will illuminate the similarities and major differences of both experiments and this way give an additional motivation for the necessity of a new g-factor experiment. Parts of the information given in this chapter can be also found in [65].

4.1 Overview of the Experiment

The complete ALPHATRAP setup is distributed over two floors of the large experimental hall at the MPIK (figure 4.1). For external generation of HCI it can be coupled to multiple ion sources located on the ground floor including the HD EBIT [106], which is foreseen to supply highly charged ions up to $^{208}\mathrm{Pb}^{81+}$ in the final stage of the experiment. Furthermore a small table-top permanent magnet EBIT [32] capable of producing HCI of medium mass up to $^{40}\mathrm{Ar}^{16+}$ or $^{129}\mathrm{Xe}^{25+}$ [107] as well as a laser ablation ion source [31] are available. The ions with charge q can be bunched, transported and decelerated to kinetic energies of $<$100 qV in an ultra-high vacuum beamline [107, 108] before they are injected into the heart of the ALPHATRAP apparatus, which is the double Penning-trap tower. It is housed in a cylindrical cryogenic vacuum chamber which is positioned in the homogeneous magnetic field region of a vertical bore superconducting magnet situated in the basement of the experimental hall. The trap chamber and the cryogenic detection electronics are enclosed and cooled to liquid helium temperatures by a purpose-built cryostat which sits on top of the magnet. The complete setup is carried by a height adjustable support structure on rails. This way it can be lifted and coupled to the beamline (section 4.3.1) while allowing for free microwave- and laser-access from below the magnet (section 4.7.4). For better accessibility of the cryo-setup the magnet is lowered and moved to the side during maintenance work.

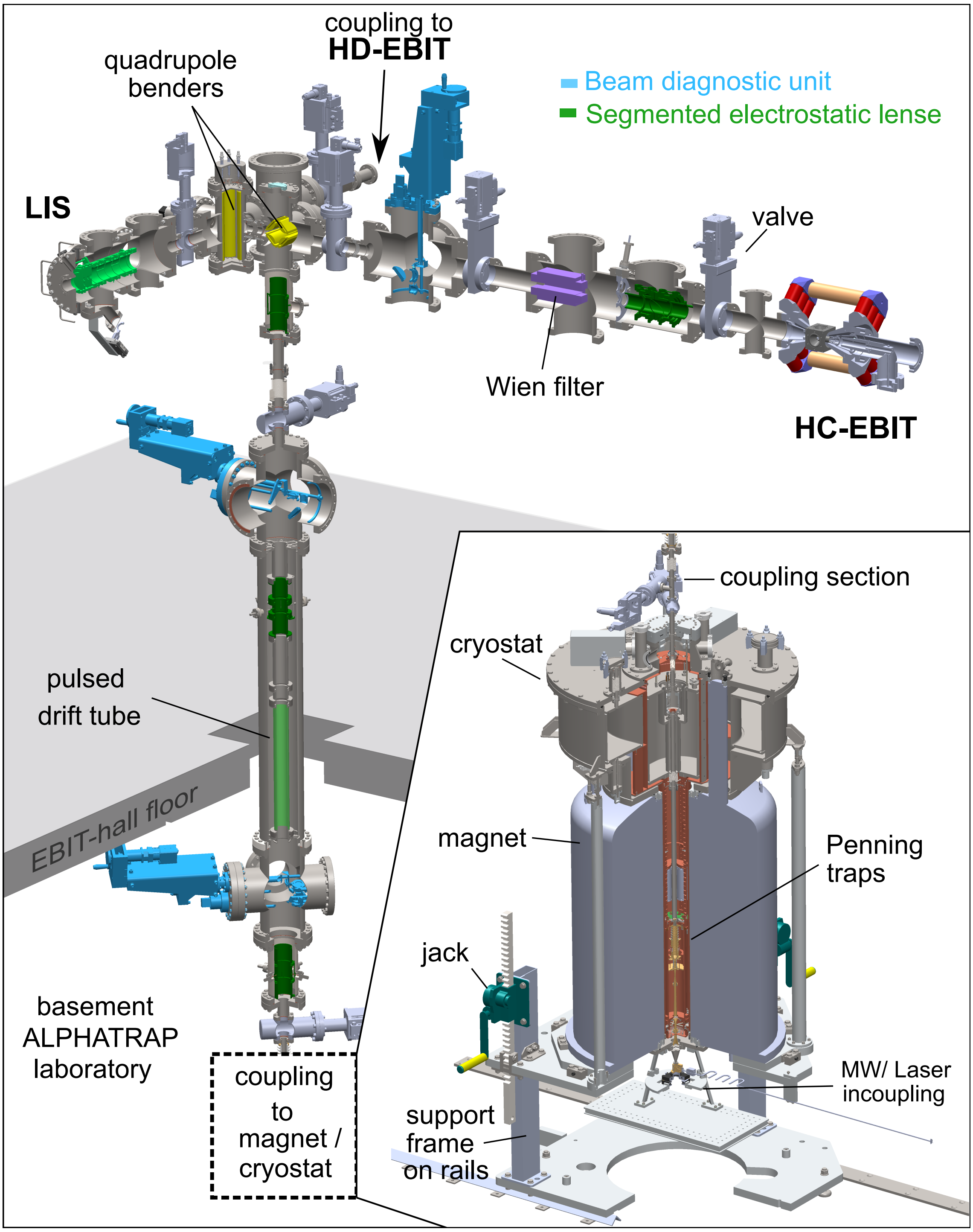

Figure 4.1: ALPHATRAP is distributed over two floors of the large experimental hall at the MPIK. In the beamline two quadrupole benders allow to inject ions from three different sources (see text). Electrostatic ion optics provide beam steering and focusing. Before injection, the pulsed ion beam is slowed down in a pulsed drift tube. The superconducting magnet and cryostat are supported by a movable frame and can be decoupled from the beamline without harming the vaccum. Pumps are not shown here.

4.2 External Ion Sources

4.2.1 EBIT-Sources

Electron Beam Ion Traps are efficient tools for generating HCI which are otherwise only accessible with large accelerator facilities. Figure 4.2 illustrates the operating principle. In an EBIT a target material (typically in the gas phase) is ionized by successive electron impact ionization with an intense electron beam. In order to increase the current densities and thus the ionization rate the electron beam is radially compressed by a strong axial magnetic field. During the ionization (breeding) process the positive ions are radially confined by the negative space charge in the electron beam. Similar to a Penning-trap, axial confinement is provided by creating a potential well with a set of hollow cylindrical electrodes (drift tubes) consisting of at least two endcaps and a central electrode (figure 4.2). From this potential well ions can be extracted in bunches[1], by pulsing down one of the endcap potentials below the central drift tube potential[2]. The achievable charge states are mainly determined by the electron beam energy and the breeding time. The breeding is counteracted by radiative recombination with electrons and charge exchange processes. A detailled discussion on the evolution of ion charge states in an EBIT can be found in [109].

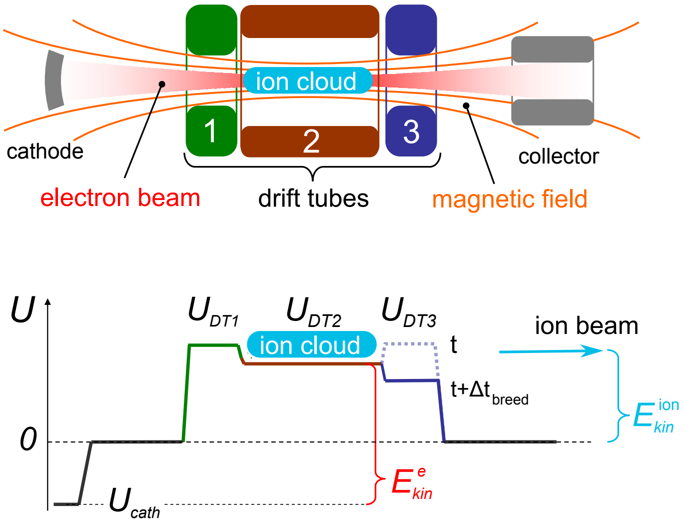

Figure 4.2: The upper picture illustrates the essential building blocks of an EBIT (see text). The lower picture shows the typical potential configuration. During breeding the ion cloud is confined in a potential well between the outer drift tube electrodes. After the breeding time Δt_{breed} the ions can be extracted as a bunch by pulsing down the last drift tube electrode. Picture taken and modified from [110].

---

[1] The ions can be also extracted as a continuous beam by setting one of the endcap electrodes to a slightly lower potential than the other. This is referred as "leeky mode" extraction.

[2] Actually, at ALPHATRAP the HC-EBIT is emptied by switching the central DT to a higher potential than the last electrode.

HD-EBIT

The large Heidelberg EBIT is expected to supply ALPHATRAP with HCI of the heaviest elements. So far electron beam currents of 500 mA and beam energies of up to 100 keV have bean achieved [106], which is enough to produce hydrogenlike lead ions. The magnetic field of up to 9 T is produced by superconducting magnet coils cooled with liquid helium. Ion extraction energies are on the order of 10 keV/q. The beamline coupling section between the HD-EBIT and the ALPHATRAP setup is currently being prepared[3].

HC-EBIT

The HC-EBIT (Heidelberg Compact Electron Beam Ion Trap) is a tabletop prototype[4] device developed at the MPIK and described in [32]. In contrast to the superconducting HD-EBIT the magnetic field is produced by 48 N45 grade NdFeB cylinder magnets and guided by a highly permeable soft iron yoke structure. This construction enables a magnetic flux density of 0.74 T within the trapping region. The electron beam is generated by a heated barium impregnated tungsten cathode and absorbed by an actively cooled collector electrode at ground potential. Electron beam energies are on the order of 3.5 keV. At ALPHATRAP so far HCI up to $^{40}\mathrm{Ar}^{16+}$ have been produced. The target gas can be injected through a needle valve. Ion extraction energies are on the order of 2 keV/q. Argon ions from the HC-EBIT have also been used for commissioning of the beamline setup and the first time injection into the trap tower in the course of this thesis.

4.2.2 Laser Ion Source

For the production of $^{9}\mathrm{Be}^{+}$ ions which are needed for sympathetic laser cooling of HCI, ALPHATRAP is equipped with a dedicated laser ion source (LIS) [31]. The ions are produced by laser ablation from a solid target material (e.g. AlBe) by short (∼7ns) high intensity ($\sim 10^{8}\,\mathrm{W/cm^{2}}$) laser pulses. The pulses are generated by a frequency doubled Nd:YAG laser and guided through a view-port into the ablation chamber where the focused beam impinges on the target. As a consequence, atoms from the target surface are evaporated and ionized. The ions are extracted in bunches by three acceleration stages including electrostatic focusing and steering elements. So far ion yields of up to $2.6 \cdot 10^{7}$ $^{9}\mathrm{Be}^{+}$ ions have been measured. For detailed information on the ALPHATRAP LIS the reader is referred to [31].

---

[3] PhD thesis by T. Sailer, in preparation.

[4] Meanwhile, an improved series of table-top EBITs with electron beam energies of up to 10 keV is available [111].

4.3 Beamline

HCI coming from the external ion source are guided towards the cryogenic trap system via the ALPHATRAP room temperature beamline shown in figure 4.3. Prior to installation at it's final destination in the EBIT hall, the room temperature beamline was separately test assembled and commissioned in an offline test setup with the HC-EBIT as described in [107, 108].

Vacuum Setup The handling of highly charged ions sets high demands on the achievable vacuum conditions within the whole experiment. This is also because the cross section for electron exchange with restgas molecules increases with the charge state of the ion [112, 113]. In principle the effect of cryopumping [114], i.e. the condensation of rest-gas on a cold surface, enables a vacuum of better than 10^{-16} mbar inside a hermetically sealed trap chamber at cryogenic temperature of 4.2K. This corresponds to single ion storage times (life times) in excess of several months [115]. However, in contrast to the Mainz experiment, the ALPHATRAP trap chamber is not permanently sealed but subjected to the steady flow of restgas, mainly hydrogen[5] , entering through the room temperature beamline coupling. In order to suppress the gas flow into the trap chamber, two measures were undertaken. On the one hand a dedicated cryogenic valve [113] was installed into the cryogenic beam tube (see section 4.8). On the other hand the beamline was designed and prepared with a low background pressure on the order of 10^{-10} mbar. This was achieved by using explicitly materials with low vapor pressures. Additionally, vacuum firing of stainless steel components prior to installation helps to reduce hydrogen outgassing. For evacuation a set of 7 magnetically levitated turbo molecular pumps is supported by an ion getter pump (IGP) and two non-evaporative getter pumps (NEG) which are installed in the vertical beamline branch. The whole beamline setup was baked in situ to ∼200 °C during offline commissioning which allowed for background pressures on the order of 10^{-11} mbar in the offline setup. If necessary, the same process can be repeated also for the online setup in the future. More information on the ALPHATRAP beamline and the vacuum system can be found in [107, 108]

Ion Transport For ion transport the ALPHATRAP beamline is equipped with various ion optics. Beam focusing is provided by electrostatic einzel lenses. Steering is accomplished by applying suitable voltages to special segmented lenses. Two quadrupole benders (one vertical and one horizontal) allow to choose between the ion sources and guide the ion beam into the vertical beamline section which is coupled to the cryogenic assembly containing the trap tower. Ions coming from the HC-EBIT can be additionally preselected by a velocity filter (Wien filter) [116] according to their charge-to-mass (q/m) ratio. During beam adjustment the beam shape and position can be monitored with 5 diagnostic units installed at suitable

---

[5] Due to their small atomic masses cryopumping is not as effective for hydrogen and helium but the freeze out is limited to a few atomic layers [114].

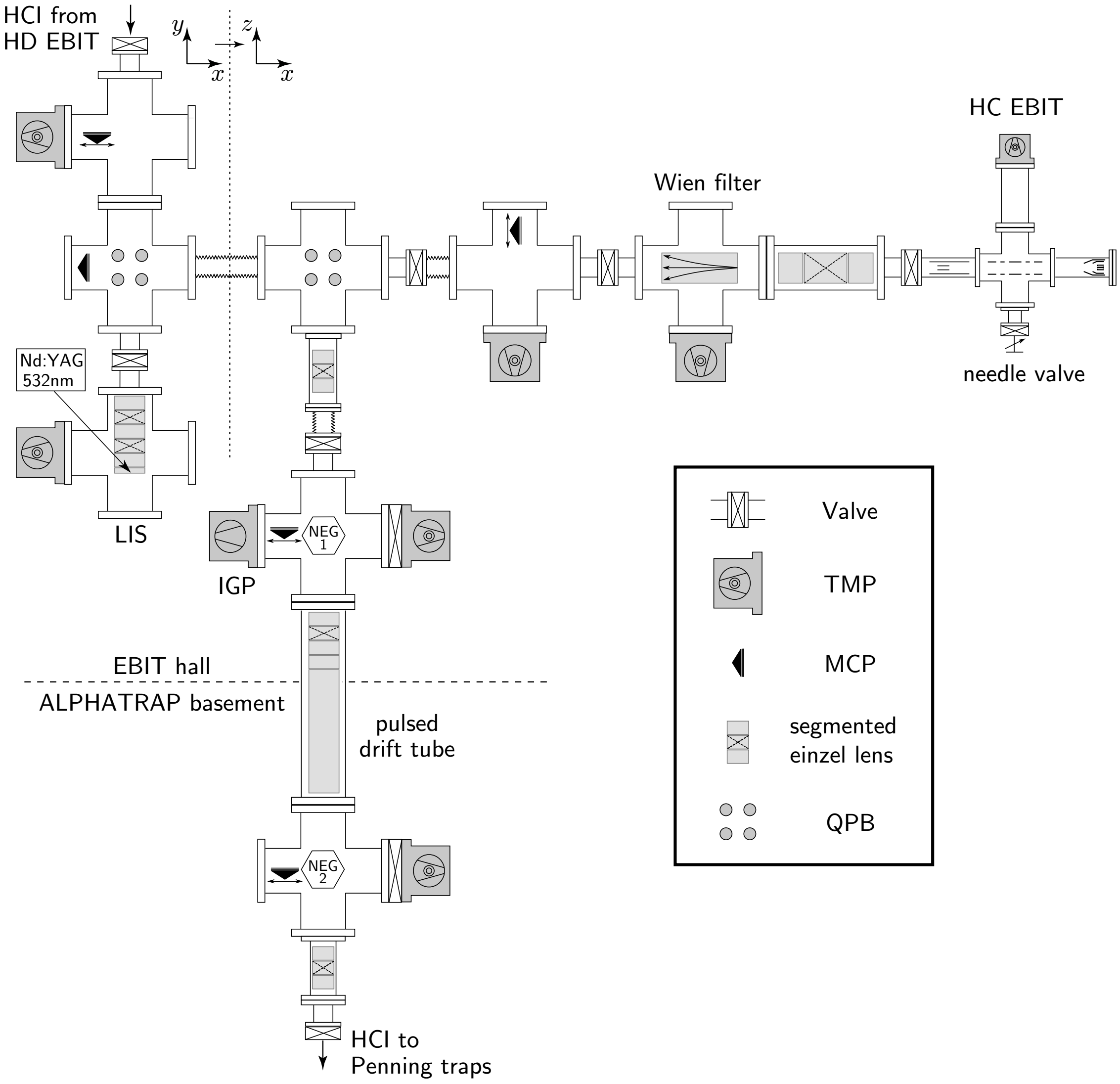

Figure 4.3: Overview of the beamline setup. The location of pumps is also shown. The LIS and the coupling to the HD-EBIT are situated opposed to each other in the same branch of the horizontal beamline. Two quadrupole benders allow to choose between the three ion sources. Prior to injection into ALPHATRAP, the ions are decelerated with a pulsed drift tube (see text). Modified from [65].

locations. Each diagnostic unit consists of a micro channel plate (MCP) detector equipped with a phosphor screen and a CCD[6] camera. For final ion deceleration and capturing the trap tower includes a dedicated capture section (chapter 4.7.1) with a maximum blocking voltage of 1200 V. However, considering ion transfer energies of up to 10 keV/q coming from the HD-EBIT, the ion bunches have to be pre-decelerated already in the beamline, before they can be injected into the capture section. For this purpose the vertical beamline includes a 0.5 m long pulsed drift tube electrode which is pulsed from a high to a low (ground) potential as soon as the ion bunch is inside the field free region of the drift tube. This way, successful ion capturing with final injection energies below 100 electronvolt/q has been achieved in the course of this thesis.

4.3.1 Beamline Coupling

The room temperature beamline and the cryogenic vacuum setup inside the magnet are connected via a vacuum coupling section situated above the cryostat (see figure 4.1). It is enclosed between two gate valves and thus can be sealed off from the rest of the beamline. A third valve on a separate port[7] allows for pressurization/evacuation of this section. This construction enables to couple and decouple the cryogenic vacuum assembly and the room temperature beamline without harming the respective vacuum conditions. Furthermore the coupling section includes a flexible membrane bellow and a ceramic insulation tube which provides galvanic insulation from electronic noise entering from the beamline setup. After the coupling section the beamline is extended down through the magnet and connected to the cryogenic trap chamber via a cryogenic beam tube with 0.8 cm radius. To enter the trap tower/chamber the beam has to pass through a 3 mm diaphragm/pumping barrier which also serves as a Faraday cup (see section 4.7.1). It is important to note, that the 1.7 m long transition region, starting at the last steering element of the room temperature beamline above the magnet and ending at the diaphragm, does not include any steering elements but the beam is guided (and simultaneously compressed) only by the field lines of the superconducting magnet.

4.4 Superconducting Magnet

At ALPHATRAP the strong homogeneous magnetic trapping field is generated by a superconducting, vertical bore NMR[8] magnet manufactured by Oxford Instruments. Prior to ALPHATRAP the same magnet was already successfully used by the former Penning-trap mass spectrometer SMILETRAP [117]. A comparable model is also part of the Mainz experiment. In 2016 the ALPHATRAP magnet was initially charged to

---

[6] charge coupled device

[7] The third port is provided by a conflat(CF) Tee piece.

[8] nuclear magnetic resonance

~4.02 T and shimmed to a spatial homogeneity of $\frac{\delta B}{B} < 3 \cdot 10^{-7}$ [9] in a volume of 1.5 cm^3. The chosen magnetic field of $\sim$ 4T corresponds to a Larmor frequency of $\sim$ 112GHz for hydrogenlike systems and is mainly determined by the currently available microwave source. The magnet features a warm bore, meaning that the homogeneous magnetic field region is accessible at room temperature without getting in contact with the cryogenic liquids (liquid helium) of the magnet cryostat. Therefore, in order to still be able to use the advantages of a cryogenic environment, the experimental section including the trap chamber and the cryogenic electronics must be cooled with a separate cryostat described in the following section. Although this solution increases the overall mechanical intricacy it has some important advantages compared to a cold bore magnet type. For instance, the cryogenic experimental setup includes large copper parts (trap chamber) and also type-II superconducting material[10] in the electronic section (resonators, see chapter 5). With an independent cryostat these parts can be cooled below their critical temperature after being positioned in the magnetic field. During insertion this greatly reduces the stress on the magnet coils caused by eddy currents and the Meissner effect. The warm bore limits the available space for the experiment to a maximum diameter of 13 cm.

4.5 Cryogenic Setup

The cryogenic setup of the ALPHATRAP experiment is cooled by a homebuilt bath type cryostat with an inner liquid helium (LHe) stage and an outer liquid nitrogen (LN2) stage. Prior to presenting the ALPHATRAP cryostat in detail, a few general design concepts of a bath type cryostat will be briefly discussed.

4.5.1 Cryostat Design Concept

The working principle of a bath type cryostat is based on the evaporation of cryogenic liquids which keeps the cryostat stages on the respective boiling temperatures (4.2K for LHe and 77K for LN2). Depending on the volume of the cryogenic vessels and the thermal load, the cryogenic liquids have to be topped up after a certain time[11]. The refill procedure is typically associated with temperature and pressure fluctuations inside the cryostat, which also affects the frequency stability of the particle. To keep the number of interruptions during the measurement process small the cryostat design is optimized for a maximum refilling period/cycle of the helium and nitrogen vessel. This is achieved by keeping the total heat transport to the cryostat as small as possible. The total thermal load acting on the cryostat stages originates from **convection**, **thermal radiation** and **thermal conduction** processes.

---

[9] 47 Hz of the proton line (171 MHz)

[10] Type-II superconductors do not show a full Meissner effect but allow for a certain quantized flux penetration between two critical temperatures, the so-called Shubnikov phase.

[11] Presently, there is no closed cycle He-liquifier available for ALPHATRAP.

Convection In most cryostat designs convection and conduction losses by air are greatly suppressed by the use of an evacuated chamber (vacuum vessel) which surrounds the cryostat stages. At a typical insulation vacuum pressure of $\sim 10^{-6}$ mbar convection losses are negligible compared to the other (radiation and conduction) loss mechanisms[12] [118].

Thermal Radiation A considerable part of the thermal load is introduced by thermal radiation from warm surfaces surrounding the cryostat stages (e.g. the vacuum vessel, which is at room temperature). The heat radiation emitted by a surface area A with temperature T is given by the Stefan-Boltzmann law:

$$\dot{Q}_R = \epsilon \sigma A T^4 \tag{4.1}$$

with the Stefan-Boltzman constant $\sigma = 5.67 \times 10^{-8}\,\mathrm{W/m^2K^4}$. The material dependent quantity ϵ denotes the emissivity of the surface compared to an ideal black body with the maximal emissivity $\epsilon = 1$.

Due to the small heat of evaporation of LHe ($\Delta Q_V^{He} = 2.7\,\mathrm{kJ/l}$) a direct exposure of the LHe stage to the 300 K room temperature heat radiation should be avoided. This can be achieved with the help of a nitrogen-cooled radiation shield (active shield) surrounding the experiment. This way the radiative load acting on the LHe stage can be reduced by a factor of (at least) $(33\mathrm{K}/77\mathrm{K})^4 \approx 230$. Per unit volume liquid nitrogen has a $\sim$60 times higher heat of evaporation ($\Delta Q_V^{N2} = 161\,\mathrm{kJ/l}$) than liquid helium and can therefore withstand the room temperature radiation correspondingly longer[13]. In general the effectiveness of a radiation shield also depends on it's emissivity ϵ with [119]

$$\epsilon \propto \sqrt{\frac{16\pi\epsilon_0 \rho c}{\lambda}}, \tag{4.2}$$

where ϵ_0 is the vacuum permittivity, c is the speed of light, ρ is the electrical resistivity of the shield material and lambda is the wavelength of the emitted radiation. According to Wien's displacement law the emitted black body radiation wavelength maximum is inversely proportional to the temperature. This way the shielding effect even surpasses the initially assumed T^4 scaling. Relation (4.2) suggests the use of good conductors as shielding material. However, the emissivity also strongly depends on their surface characteristics such that clean and polished surfaces are preferred.

Apart from actively cooled shields, passive or so called floating shields offer an additional possibility to reduce the radiative load. Floating shields consist of one ore more separated highly reflective layers which are arranged in an onion-like manner and with little thermal contact around the surface to be screened. Such shields are available for example in the form of super insulation sheets. These consist of several

---

[12] In general this only applies for sufficiently large isolation distances within the cryostat.

[13] This approach is also more economical because of the comparably higher pricing of liquid helium.

layers of metal coated plastic film which is thermally decoupled from each other by poorly heat-conducting polyester fabric. For example a stack of N layers placed between two concentric cylindrical surfaces with temperatures T_h and T_c will reduce the heat radiation impinging on the inner cold stage according to [120]

$$\dot{Q}_R = \frac{\sigma(T_h - T_c)}{\frac{1}{A_c\epsilon_c} + \frac{1}{A_h}\left(\frac{1}{\epsilon_h} - 1\right) + \left(\frac{2}{\epsilon_s} - 1\right)\sum_{i=1}^{N}\frac{1}{A_i}}, \tag{4.3}$$

as long as all insulation layers have the same emissivity ϵ_s. Assuming that the surfaces are very close to each other such that $A_h \approx A_c \approx A_i$, equation (4.3) can be simplified to

$$\dot{Q}_R = \frac{\sigma A(T_h - T_c)}{\frac{1}{\epsilon_c} + \frac{1}{\epsilon_h} - 1 + N\left(\frac{2}{\epsilon_s} - 1\right)}. \tag{4.4}$$

Thermal Conduction The heat flux which is conducted through a material between points of different temperature is described by Fourier's law. In it's simple one-dimensional form it is written as:

$$\dot{Q}_C = -\lambda(T)A\frac{dT}{dx}. \tag{4.5}$$

where A is the cross sectional area and $\lambda(T)$ is the material and temperature dependent thermal conductivity. The heat flow through a body with length l connecting two heat reservoirs with temperatures $T_{h(ot)}$ and $T_{c(old)}$ can be calculated as

$$\dot{Q}_C \int_0^l \frac{dx}{A(x)} = \int_{T_c}^{T_h} \lambda(T)dT, \tag{4.6}$$

and for a uniform body with $A = const.$ one gets

$$\dot{Q}_C = \frac{A}{l}\left(\int_0^{T_h} \lambda(T)dT - \int_0^{T_c} \lambda(T)dT\right). \tag{4.7}$$

The last bracket contains the so called thermal conductivity integrals (or "thermal potentials") $\theta_T \equiv \int_0^T \lambda(T)dT$ of the respective materials. In table 4.1 the thermal conductivity integrals of some selected materials are listed. From this it can be seen that all parts of the cryostat which must be cooled, should consist of highly conductive metals such as copper while necessary mechanical connections between the cryostat stages should consist of plastics or stainless steel.

Furthermore, direct connections between the room temperature section and the inner liquid helium stage should be suitably coupled/thermalized at the liquid nitrogen stage. Depending on the position of this coupling the thermal load onto the 4K stage will be reduced at cost of the liquid nitrogen consumption. For example, a uniform rod of length l which connects the 300K and 4K stage and is halfway anchored to the 77K shield would reduce the thermal load on the 4K stage by

$$\frac{\theta_{77K} - \theta_{4K}}{l/2} \cdot \frac{l}{\theta_{300K} - \theta_{4K}} \approx 2 \cdot \frac{\theta_{77K}}{\theta_{300K}}. \tag{4.8}$$

	$\theta_T = \int_0^T \lambda(T)dT$ (W/m)		
Material	θ_{4K}	θ_{77K}	θ_{300K}
OFHC (RRR=100)	1300	10^5	$2 \cdot 10^5$
manganin	0.85	600	4000
stainless steel	0.5	300	3000
epoxy G-10	0.35	20	126
PTFE Teflon	0.05	13	70
polyimid Vespel	0.02	5.7	43

Table 4.1: Thermal conductivity integrals of selected materials used at the ALPHATRAP cryosetup (see text). Data collected from [121, 122]

.

4.5.2 ALPHATRAP Cryostat

The ALPHATRAP cryostat is shown in figure 4.4. The homebuilt bath type cryostat includes a LHe and a LN2 stage which are surrounded by an insulation vacuum vessel. The cryostat is sitting on top of the magnet. Since the magnet is limited to a maximal payload of 100 kg the cryostat weight of about 400 kg is distributed between the magnet and three additional support poles. For a uniform weight distribution each pole is variable in length and equipped with a compression force sensor. In the following the individual building blocks of the cryostat will be presented.

Vacuum Vessel In order to avoid thermal conduction and convection losses by air, the cryostats LHe and LN2 stage are enclosed in a large insulation vacuum vessel. The cryostat insulation vacuum also serves as a prevacuum for the trap chamber. An adapter flange provides a hermetical seal between the vacuum vessel and the magnet bore which is part of the prevacuum chamber. Prior to cooling down the experiment, the prevacuum chamber is pumped to $\sim 10^{-3}$ mbar. During cryogenic operation a prevacuum of $\sim 10^{-6}$ mbar (measured in the room-temperature section) is achieved by cryopumping. Because of it's size the vacuum vessel is prone to deformation due to the atmospheric pressure variations[14]. This is especially problematic considering that the cryogenic 4K insert (see below) including the trap setup is supported by the vacuum vessel lid. Thus, short term atmospheric pressure variations on the order of ~1 mbar directly affect the position of the trap tower (containing the AT ferromagnetic ring) in the magnetic field and this way may degrade the frequency stability. Therefore, the mechanical design of the vacuum vessel has been optimized for the highest possible rigidity[15]. Pressure induced displacements can be additionally compensated by a set of piezo actuators installed in the 4K insert suspension.

---

[14] The atmospheric force acting upon the vacuum vessel lid which has a diameter of 0.8 m, corresponds to ~500 kg.

[15] A pressure change of ~1 mbar corresponds to a simulated vertical displacement of only 27 nm.

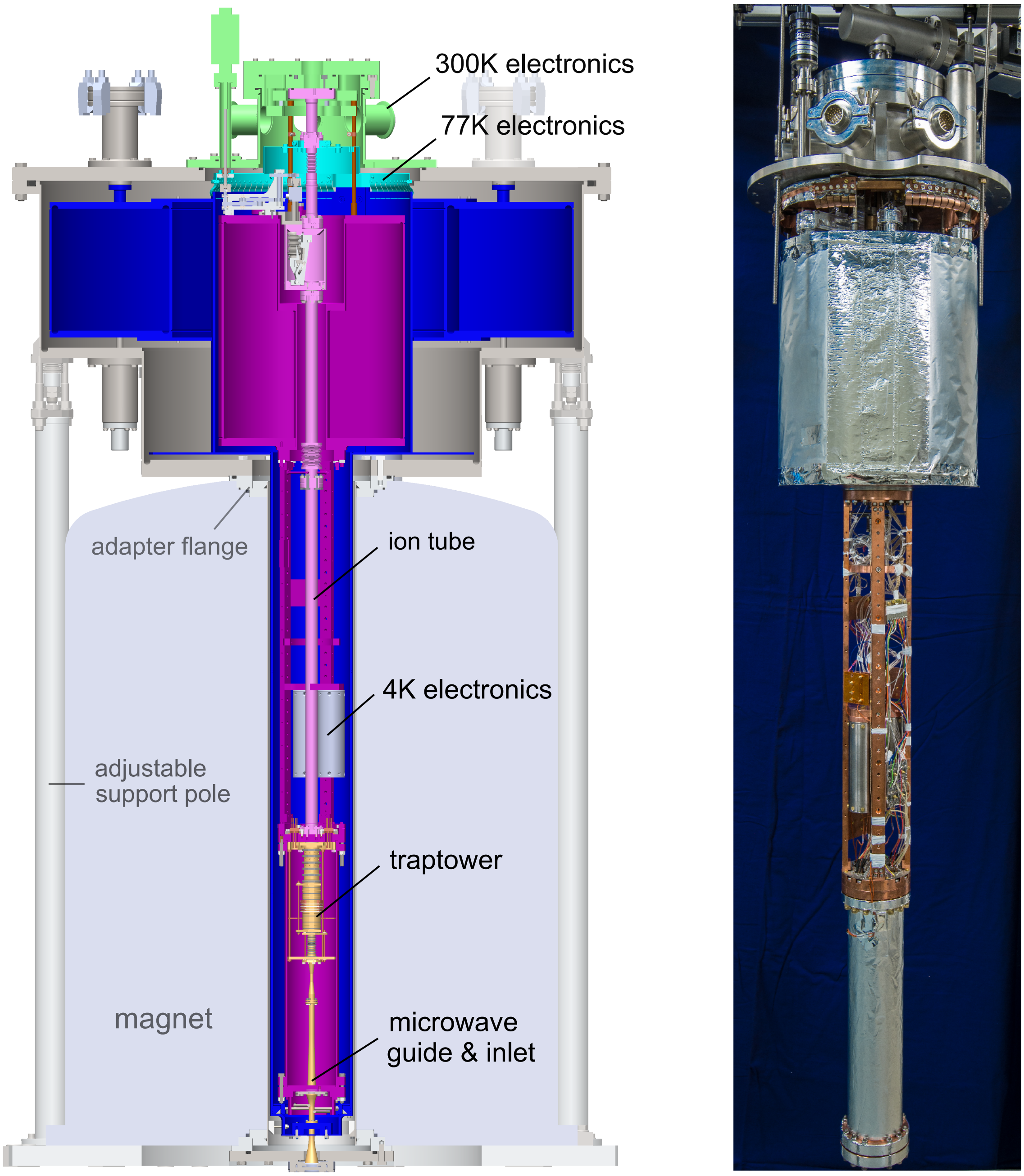

Figure 4.4: The homebuilt cryostat is sitting on top of the magnet. The vacuum vessel is fixed with an adapter flange to the magnet bore which is part of the prevacuum chamber. The liquid nitrogen vessel and the 77K shield are shown in blue. The assembly, consisting of trap chamber, 4K electronic section and helium cryostat, form the cryogenic 4K insert (pink). It is suspended via low-conductance rods (light brown) from the so-called hat (green). The 77K shield is completed by the hat shield (light blue) which is part of the 4K insert. For maintenance purposes the cryogenic insert including the hat shield can be pulled out of the magnet as shown in the photograph on the right.

77K Stage The 77K stage serves as an actively cooled radiation shield which screens the 4K stage from the 300K room temperature radiation[16]. The cooling is provided by a large stainless steel liquid nitrogen reservoir with a capacity of 55 l. It is firmly connected (screwed) to the radiation shield which conists of 3 mm thick copper. To enclose the complete 4K stage the radiation shield extends down into the magnet bore in form of a copper tube with 122 mm outer diameter. The whole 77K stage is wrapped in ∼20 layers superinsulation foil (Coolcat2NW) from the company RUAG Space. Great care was taken to support the 77K stage with the least possible contact within the 300K vacuum vessel. Still, there are three sources of direct heat conduction which are hard to avoid:

- **LN2 Reservoir Support:** The LN2 reservoir sits on three adjustable hollow rods made from stainless steel which support it's weight including the attached shield assembly. Each rod is 11.5 cm long and 1 cm in diameter.

- **Shield Tube Fixation:** To efficiently use the available space inside the magnet bore the distance between the inner magnet bore wall and the shield tube measures only 4 mm on a length of 1m. To prevent misalignment (especially during cool-down) and thus the risk of a direct metallic contact/heat-bridge, the lower end of the LN2 shield tube is purposely centered within the magnet bore (figure 4.5) via three rods made out of Vespel SP1, a high-performance polyimide-based plastic which combines low thermal conductivity and good mechanical stability at cryogenic temperatures.

- **LN2 Filling Ports:** The LN2 reservoir is equipped with three ports which are used for liquid nitrogen filling, pressure equalization and level monitoring. The ports are led out of the insulation vacuum via bellows which are hermetically sealed against the vacuum vessel. For this purpose flexible bellows with a high number (40) of membranes were chosen in order to ensure a long connection distance and thus a high heat resistance.

---

[16] Apart from the 77K radiation shield the Mainz experiment also included a 20K shield which was actively cooled by the evaporating cold helium gas. Due to space constraints inside the magnet bore the ALPHATRAP cryostat lacks a 20K shield. Instead the helium reservoir capacity was adequately scaled from 5l(Mainz) to 15l(ALPHATRAP).

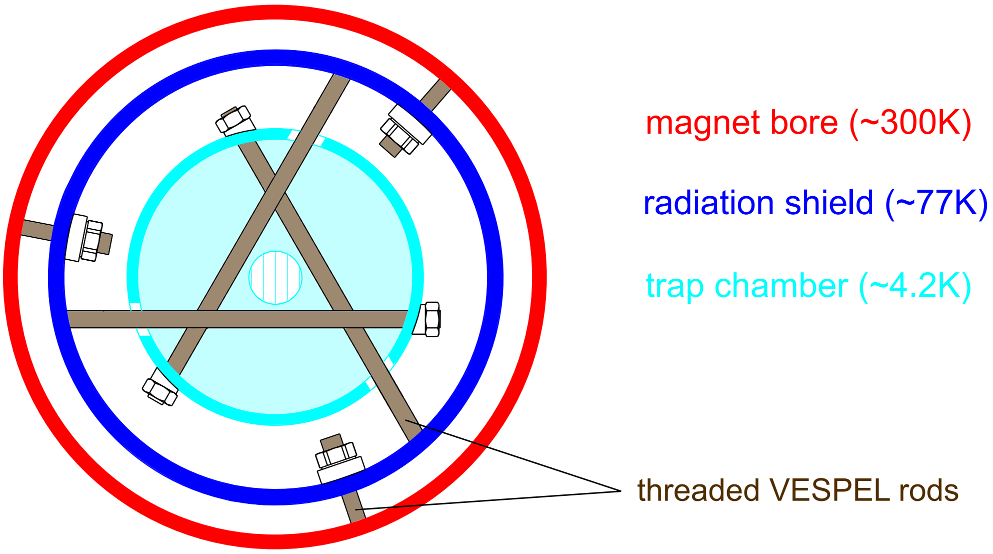

Figure 4.5: Simplified illustration of the cryogenic fixation (bottom view, not to scale) which centers the radiation shield and the trap chamber inside the lower end of the magnet bore. The different temperature stages are interconnected by poorly heat conducting VESPEL rods (see text). The noteworthy arrangement of the trap chamber fixation provides particularly low heat conductance and allows central access for the microwave/laser incoupling (small inner circle).

4K Insert The cryogenic trap chamber and electronics are cooled by the inner LHe stage to nominally 4.2K. The trap chamber is made from oxygen-free high (thermal) conductivity copper (OFHC). It is attached to the ion-tube and an OFHC structure which includes the cryogenic electronics and provides the thermal coupling to the liquid helium reservoir with a volume of 14.5 l. This assembly, termed “cryogenic 4K insert” is shown on the photograph in figure 4.4. It is suspended from the vaccum vessel "hat"-flange down into the magnet bore. It can be completely decoupled from the room temperature beamline and lifted out of the magnet for maintenance purposes. Bellow the 300K "hot" hat flange the cryo insert includes the so called 77K hat flange shield. This is a separate piece of the 77K radiation shield which is pulled out of the magnet together with the cryo insert. The hat shield is reconnected to the rest of the 77K shield (which is permanently mounted inside the vacuum vessel) via copper braids and copper-beryllium springs during lowering of the 4K insert. In order to provide additional shielding from the 77K radiation the 4K insert is wrapped with a special single layer superinsulation foil (Coolcat4K) from RUAG Space. Direct heat conduction between the 4k insert and the warmer 77K and 300K stage is mainly caused by:

- **4K Insert Suspension:** The 4K insert is suspended from the room temperature hat flange via three 13 cm long and 6.3 mm thick VESPEL SP1 rods. Each rod is thermally anchored to the 77K hat shield with a copper braid.

- **4K Insert Fixation:** The 4K insert is hanging freely from the VESPEL rods into the 77K shield tube which sits inside the magnet bore. By using a fixation of 3 vespel rods attached to the lower trap chamber flange, the 4K insert is centered within the shield tube in a similar manner as the shield tube is centered within the magnet bore (4.5.2). The complete fixation is shown in figure 4.5.

- **LHe Filling Ports:** The LHe reservoir is equipped with two filling ports. These are guided out and sealed against the insulation vacuum chamber in a similar manner as for the 77K reservoir. The heat introduced through the filling ports is reduced by using a combination of thin walled (0.23 mm) elongation tubes and membrane bellows which are also anchored to the 77K hat shield[17].

- **Cryogenic Cabling:** The trap and the cryogenic 4K electronics are supplied with about 50 DC-lines made from 0.1 mm thick manganin wire. The AC signals are transported via 13 cryogenic coaxial cables made from stainless steel. All wires are introduced through vacuum feedthroughs in the hat flange and are thermally anchored to the 77K hat flange shield before they are guided down into the 4K electronic section.

Temperature Sensors

For temperature monitoring, the ALPHATRAP experiment is equipped with 6 self-made and calibrated temperature sensors. To this end, the temperature dependence of carbon-composition resistors was exploited (carbon resistance thermometer or CRT). Particularly suitable for this purpose are resistors of the manufacturer Allen Bradly which have a comparatively uniform thickness of the carbon layer [123]. In addition to a low price, CRT sensors are characterized by a good sensitivity at low temperatures. The temperature behavior can be approximated by the polynomial [123]

$$\frac{1}{T} = \sum_{i=1}^{n} a_i \left(\log R\right)^i , \tag{4.9}$$

where the coefficients a_i are free fit parameters to the calibration data. Prior to calibration all sensors were temperature cycled[18] several times. The calibration of each sensor was carried out with a commercial Cernox sensor from Lake Shore Cryotronics. Figure 4.6 shows a typical interpolated calibration curve as well as the

---

[17] Additionally, the thermal conductivity is reduced by the cold gas stream of the evaporating LHe.

[18] Due to carbon granule rearrangement during the first cooling cycles an increase on the order of 6% in the resistance value was observed.

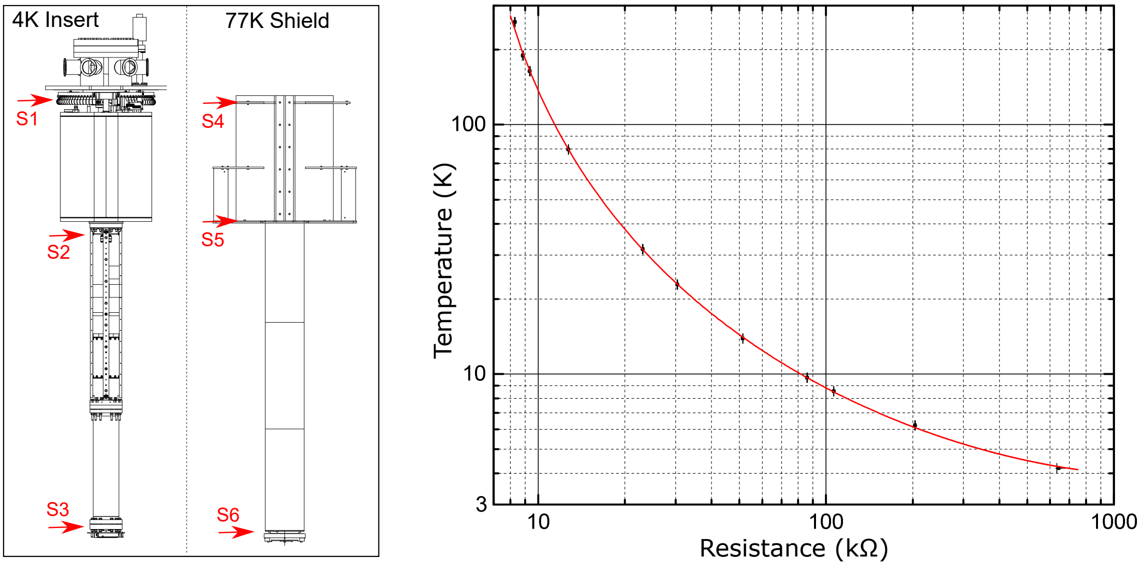

Figure 4.6: Left side: Temperature sensor locations (red arrows) in the 4K and 77K stage of the cryostat. Right side: Exemplary calibration curve of a CRT sensor. The sensitivity is increasing with decreasing temperature ranging from $\sim 0.1\frac{\mathrm{k}\Omega}{\mathrm{K}}$ at 77K to $\sim 800\frac{\mathrm{k}\Omega}{\mathrm{K}}$ at 4K.

sensor mounting positions in the cryostat. The absolute temperature error due to the calibration procedure and interpolation is estimated to $<\pm 0.15\,\mathrm{K}$ at $4.2\,\mathrm{K}$ and $<\pm 1\,\mathrm{K}$ at $77\,\mathrm{K}$ which is completely sufficient for our purposes especially considering the good sensitivity.

4.5.3 Heat Load Estimation and Measurement

The thermal load acting on the ALPHATRAP cryostat stages are estimated using the principles introduced earlier and taking into account the cryostat geometries and previously described design specifications. In table 4.2 the result of such an estimation is summarized. Considering the complexity of the problem and the large number of unknown parameters[19] the calculated values are not intended to be accurate but rather should give an idea of the magnitude of the individual heat losses. For comparison the actual holding times are determined by extrapolating the monitored cryogenic liquid levels during one refilling cycle as shown in figure 4.7. The measured holding times are ~ 4.4 days for LHe and ~ 5.1 days for LN2. It must be noted that the amplifier losses are not included in the comparison since the cryo amplifiers were switched off during the measurement. Assuming the amplifiers are permanently powered during a measurement the LHe reservoir has to be refilled every 4 days.

---

[19] For example material properties such as quality and structure of radiating surfaces, heat conductance of compressed superinsulation a.s.o.

		4K stage	77K stage
reservoir capacity		14.5 l	55 l
conduction losses	suspension/support	10mW	2.75W
	lower fixation	5mW	50mW
	filling ports	15mW	200mW
	cabling	30mW	
	amplifiers	(10mW)	
radiation losses		35mW	23W
total estimate (w.o. amplifiers)		95mW	26W
≡ holding time		4.7 days	4 days
measured holding time		4.4 days	5.1 days

Table 4.2: Estimation of the total heat load acting on the cryostat stages in comparison to the measured heatload. The different loss sources are listed individually. Note that the cabling of the cryogenic electronics as well as the power loss of the cryogenic amplifiers contribute about 40 % of the total heat load of the 4K stage. The cryo amp losses are not included in the total heat load estimate because the cryo amplifiers were switched off during the measurement.

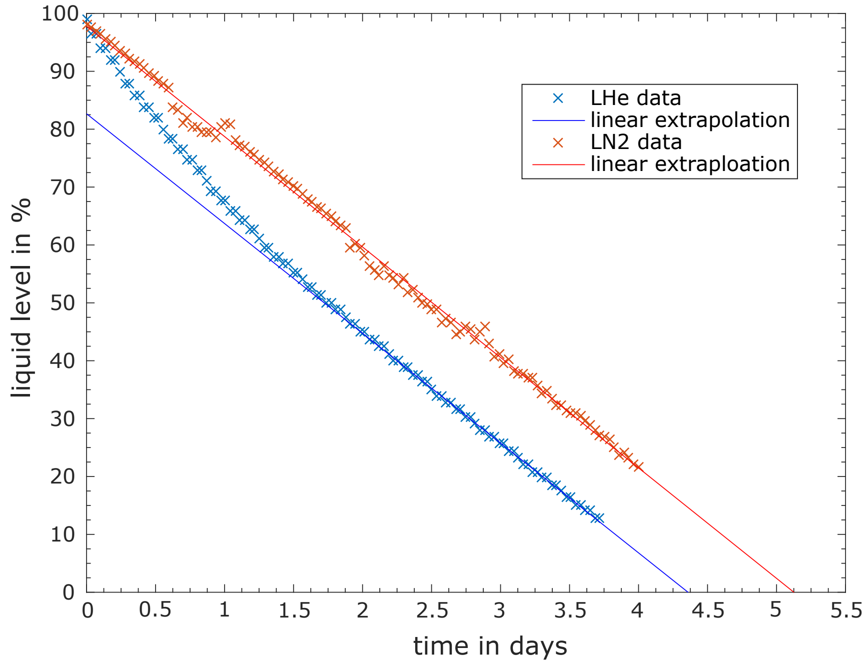

Figure 4.7: Measured cryogenic liquid levels in the LHe (blue) and the LN2 (red) reservoir during one filling cycle. The hold up times are determined from linear extrapolations and are ∼ 4.4days for LHe and ∼ 5.1days for LN2. The sporadic jitter in the LN2 data is probably due to air ice or other contaminants floating in the LN2 vessel. The initial kink in the LHe curve is caused by the non-uniform cross-sectional area of the LHe reservoir along the filling height.

4.6 Cryogenic Valve

For external ion injection the trapchamber is connected to the room temperature ALPHATRAP beamline which provides a vacuum on the order of 10^{-11} mbar after baking. To minimize the external gas flow from the beamline as well as direct heat radiation into the trap chamber, a dedicated cryogenic valve described in [113] was included into the cryogenic 4K part of the ion guide. It is mechanically actuated from the outside and can be closed during normal operation, i.e. after successful ion injection into the trap. The full cryo-valve drive mechanism is shown in figure 4.8.

Gear System The direct operation of the cryogenic valve requires a considerable amount of torque which is passed on to the liquid helium cryostat and the cryogenic insert. Although the VESPEL rods which suspend the cryogenic insert, provide a high tensile strength even at cryogenic temperatures[20], the geometry is not rigid with respect to torsion. In the worst case, the suspension could break or cause a displacement of the cryo-insert and consequently the trap setup. In order to reduce the torque on the cryogenic insert and allow for easier handling, the cryo-valve is operated via a dedicated cryogenic gear system which provides a reduction of $\sim 1/4.38$ and sits on top of the LHe reservoir.

Manipulator System The cryo-valve is actuated manually via a magnetically coupled[21] vacuum manipulator which allows for rotational and translational movement of the manipulator shaft. Since the manipulator is on room-temperature, the following precautions were taken in order to reduce the additional heat load on the 4K stage:

- The manipulator shaft is extended with a poorly heat conducting 7 cm long, thin walled G10 tube (see table 4.1).
- The manipulator shaft and the gearbox are not permanently connected, but can be coupled on demand using a self aligning hex-key type coupling mechanism. After operation (opening or closing of the valve), they are separated again.
- The manipulator shaft is introduced through a hole in the 77K hat-shield. The shaft is thermally anchored to the LN2 hat shield via a specially shaped copper beryllium spring. It screens the room temperature radiation which would otherwise enter through the cut out hole. Essentially, the spring functions as a friction bearing, meaning that it stays in mechanical/thermal contact with the shaft while allowing for free rotational and translational movement of the shaft.

---

[20] Prior to installation the tensile strength of the VESPEL rods at liquid nitrogen temperatures was verified by applying a force of ~1500 N to a single rod.

[21] The absolute magnetic field produced by the magnetic handle is $<50\,\mu$T at the position of the ion tube and does not influence the ion injection into the experiment.

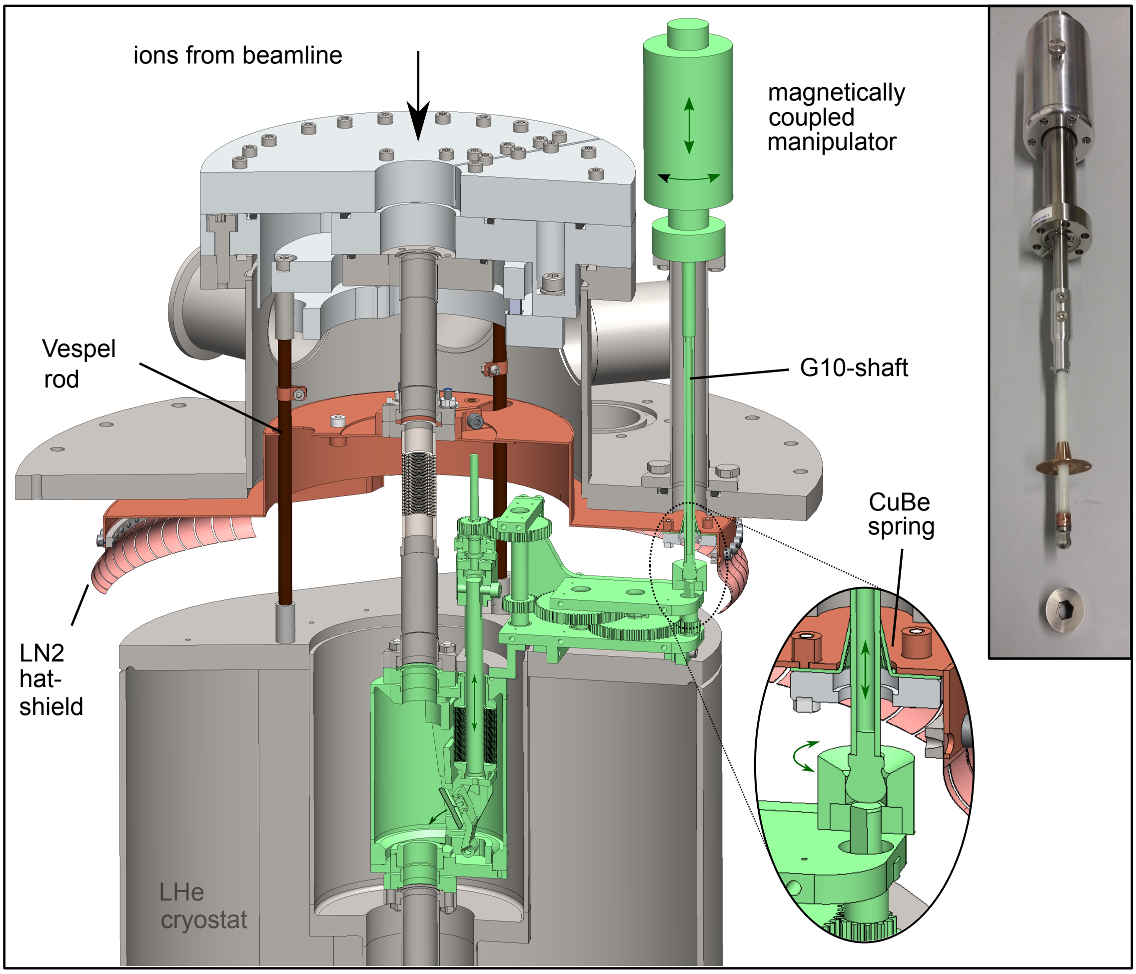

Figure 4.8: Cut view showing the elaborate mechanical design of the upper cryogenic insert and hat. For thermal decoupling the LHe cryostat is suspended only by three thin Vespel rods of which two are visible. The cryo-valve and the drive mechanism are highlighted in green. The cryo-valve is sealed to reduce the torque on the cryostat suspension, the cryo-valve is actuated via a gear system (see text). The gear is operated by a magnetic manipulator allowing for rotational and translational movement. To open/close the valve the manipulator shaft can be coupled to the gear via a self aligning hex-key mechanism. Afterwards the manipulator is decoupled from the gear in order to reduce LHe consumption. Additionally the manipulator shaft is thermaly anchored to the 77K hat shield with a dedicated CuBe spring. The photograph shows the manipulator system separately.

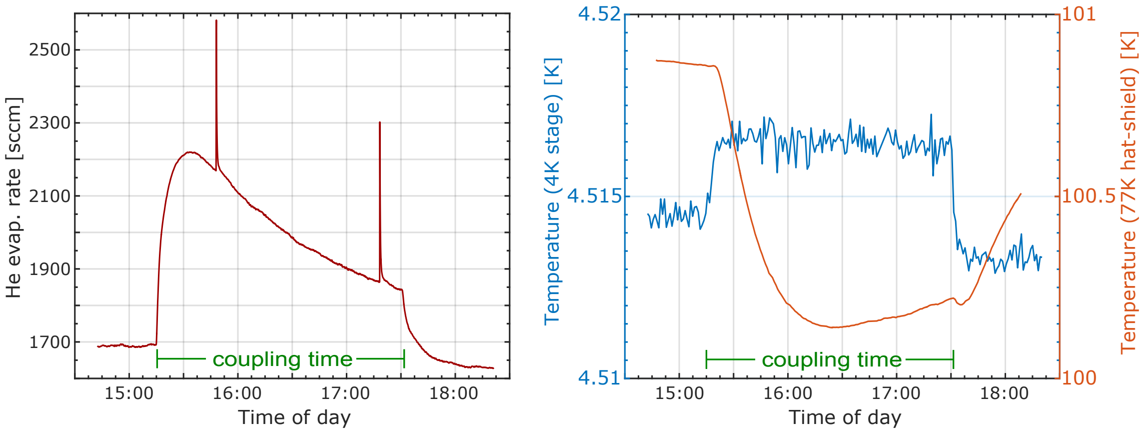

Figure 4.9: LHe consumption/flow (left) and cryostat temperatures (right) during cryo-valve coupling. The two sharp spikes in the evaporation curve are caused by the LHe level sensor which samples every 90 minutes. They are not visible in the temperature data because of a different sampling rate of the temperature data logger.

While the manipulator is coupled to the cryo-valve gear it contributes an estimated heat load on the order of 15 mW. The LHe consumption during coupling of the manipulator and the cryo-valve gearbox was determined by measuring the helium evaporation rate with a MKS gas flow meter. Additionally, the temperatures of the 77K hat shield (Sensor 1 in figure 4.6) and inside the 4K electronic section (Sensor 2 in figure 4.6) were monitored. The results are plotted in figure 4.9. While the manipulator is not coupled, the average helium gas flow[22] is ~1700 sccm [23]. Considering an expansion ratio of 1/757 for helium, the flow rate corresponds to a liquid helium consumption of ~3.2 l per day and is in accordance with the measured holding time. After coupling the manipulator to the cryo-valve gear the consumption rises by ~550 sccm which corresponds to an additional heat load of ~33 mW. The cryo-valve and drive are directly mounted to the LHe reservoir which serves as a local heat sink. Thus, the additional heat which is introduced through the manipulator has only a little effect on the 4K section temperature. During coupling the temperature in the 4K section rises by only ~5 mK. Interestingly, after the initial rapid increase the evaporation rate begins to drop again. This can be attributed to a number of effects. For instance after the first touch the manipulator thermalizes and its thermal energy is rapidly released. After that the additional load is caused by the thermal conductivity of the manipulator rod which is decreasing while the rod is cooling in. Furthermore, the manipulator is anchored to the LN2 hat shield. During coupling of the manipulator the hat shield is cooled below its steady state

---

[22] The helium evaporation rate during one filling cycle is not constant but follows an exponential decrease. The plot offset in figure 4.9 is calibrated to the time averaged evaporation rate.

[23] 1sccm = 1 standard cubic centimeter per minute

temperature[24], which reduces the thermal radiation onto the LHe stage. Another effect which reduces the initial heat load during coupling is directly linked to the increased helium evaporation rate. The filling/exhaust bellows of the LHe reservoir are cooled by the cold gas stream which decreases their thermal conductivity. All these effects come with a certain delay. Thus, after decouplig the evaporation rate even falls below the initial value (before the coupling). The same is true for the temperature in the 4K section[25]. The additional LHe consumption during the whole coupling time of about 2.25 hours is only ~60 ml. This is negligible when considering coupling times of only ~5 minutes which is typically needed for opening/closing the valve.

4.7 Trap Setup

In the following, the Penning-trap tower, which is the heart of our experiment, will be briefly introduced. A detailed discussion of the ALPHATRAP trap tower with a special focus on the trapping field optimization was carried out in [105].
In figure 4.10 an overview of the trap assembly is shown. It is housed in an indium sealed OFHC chamber and mounted to the upper trap chamber flange. The bias, excitation and signal voltages are carried through the upper flange via six individually exchangeable 6-pin feedthroughs[26] which is enough to individually supply every single of the 35 trap electrodes[27] including the microwave guide. HCI coming from the room temperature beamline are captured and stored in a capture trap (CT). The actual g-factor measurement is carried out in the precision trap (PT) and the analysis trap (AT) via the double-trap technique, which was described in section 3.2.6. Millimeter waves are introduced through a quartz-glass window in the lower trap chamber flange. Transport electrodes enable an adiabatic transport between the traps. All electrodes (except the AT ring electrode) are precision machined (lathed) from low susceptibility OFHC copper with a manufacturing tolerance of ±10 µm. The electrodes are separated by ring insulators made from sapphire (Al_2O_3) and quartz-glass. To prevent oxidation and reduce the impact of patch potentials[28] all electrodes are galvanically coated with a 10 µm gold layer. Diffusion of the gold layer is inhibited by an underlying 1 µm thick silver layer which acts as a diffusion barrier. The thickness of the coating layers as well as the shrinking of the electrodes during cooldown are considered in the design and optimization process.

---

[24] At the moment the thermal coupling of the LN2 hat shield to the rest of the LN2 stage is insufficient. It thus reaches only 100K instead of 77K.

[25] Naturally, the temperature and flow rate returned to their initial values. This is not shown in figure 4.9 because the measurement was stopped by a device error.

[26] Ceramic feedthroughs are typically very sensitive to soldering and bending of the pins. At ALPHATRAP each 6-pin feedthrough is indium sealed and can be easily exchanged in case of a leak.

[27] Splitted electrode pieces are counted individually.

[28] Patch potentials are caused by local charge accumulations on the electrode surfaces which can occur due to dielectric impurities or a varying work function of the electrode surface material.

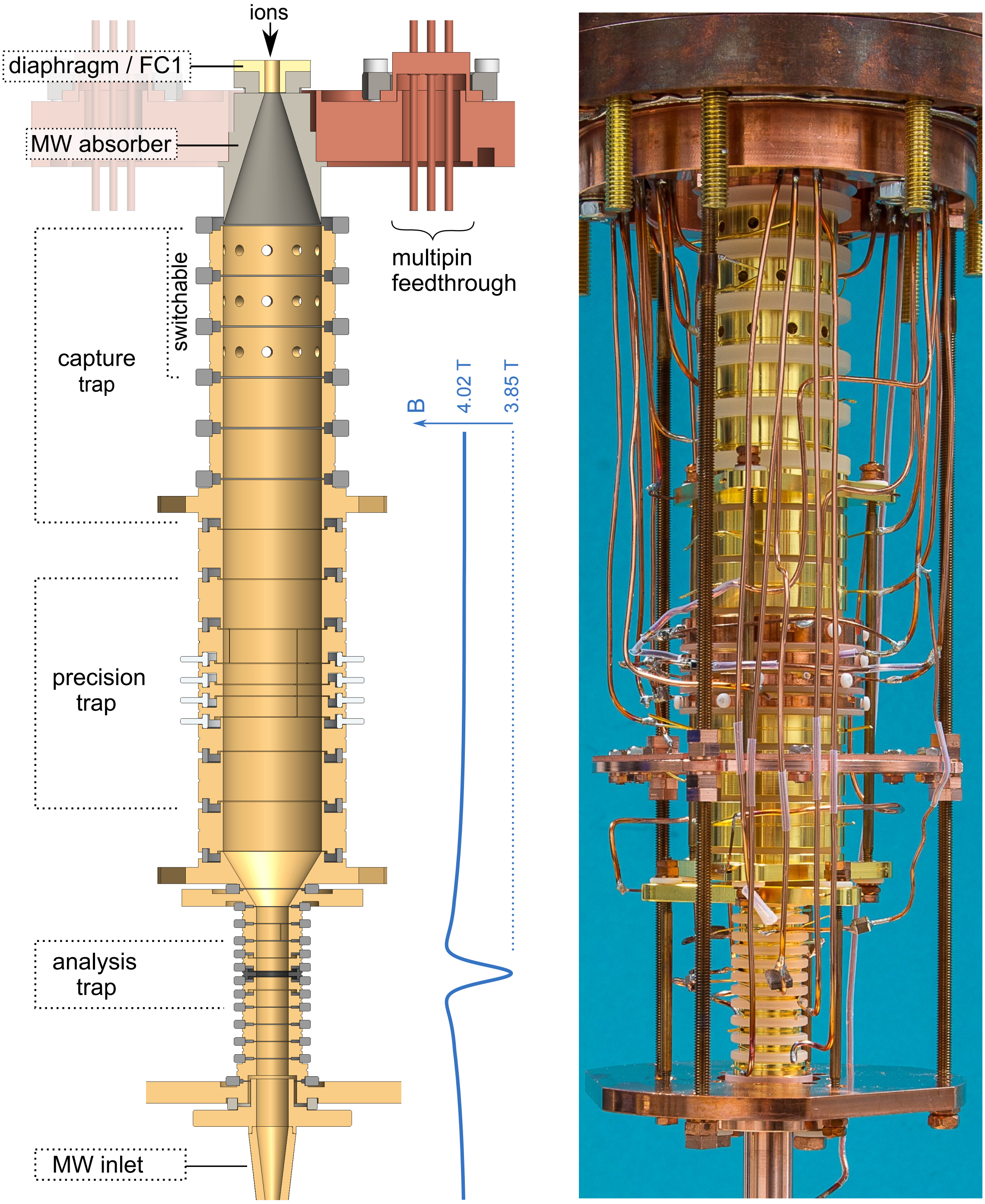

Figure 4.10: Simplified drawing and photography of the completely wired trap tower (see text for detailed description). All electrodes are gold plated. The holes in the first three capture trap electrodes increase the effective pumping cross-section of the trap chamber which is initially evacuated through the connected ion tube (not shown). The axial magnetic field in the trap tower is plotted in the middle blue graph.

4.7.1 Capture Section

HCI which were generated in one of the external ion sources are transported in bunches via the room temperature beamline. After a first deceleration by the pulsed drift tube the ion bunches are injected into the trap tower through a 3-mm diaphragm. It is located at the end of the cryogenic beam line and serves as a pumping barrier and dump for ions with excessive radial amplitudes. It is also used as a Faraday-cup for measuring the arrival time of an ion bunch (chapter 5). After passing the diaphragm, the ion bunch enters the capture section. It consists of six individually controlled electrodes. The first three electrodes are equipped with fast diode pair filters and can be switched between two voltages within 1 µs (chapter 5). To capture an ion bunch a suitable blocking voltage is applied to the lower capture electrodes. Subsequently the bunch is trapped in a potential well by rapidly switching the upper capture electrodes to a high potential. A more detailed description of the capture process is given in chapter 6. After a successful injection the capture section is used as a long term reservoir from which ions can be extracted and transported into the PT e.g. during offline operation. Additionally, the capture section can be switched to a battery supply. This considerably decreases the noise contribution during precision measurements in the adjacent PT and allows to store ions even during power cuts.

4.7.2 Precision Trap

The high-precision measurement of the free cyclotron frequency and the probing of the Larmor frequency is performed in the precision trap. The access to a wide range of ion species up to the heaviest highly charged ions imposes special demands on the ALPHATRAP PT. The design is based on the *Mainz Proton mass Trap* (now *Light Ion Trap*) discussed in [104]. It is also an orthogonal and compensated 7-electrode setup which (compared to a 5-electrode setup) enables compensation of higher order unharmonic field components as was already discussed in chapter 3.2.3. The higher harmonicity allows for larger motional amplitudes of the ion which increases the signal-to-noise ratio and decreases the phase detection uncertainty in favor of phase sensitive measurement techniques such as PnA [22]. Another important feature of our PT is the conspicuously large trap radius of $r = 9\,\mathrm{mm}$. Thus, compared to the old precision trap from the Mainz g-factor experiment with $r = 3.5\,\mathrm{mm}$, the image charge shift $\frac{\Delta\omega_c}{\omega_c} \propto \frac{m_{ion}}{r^3}$ (see chapter 3.2.3) is reduced by more than an order of magnitude, which is especially important when dealing with heavy ions. The larger trap radius also reduces systematic shifts caused by possible patch potentials on the inner electrode surface.

For radial (and quadrupole-xz) excitation and readout of the radial signal, the ring as well as the inner correction electrodes are vertically bisected. Additionally, a quadrupolar xy-excitation can be applied to one of the outer correction electrodes, which is quarter split for this purpose. The split electrode pieces are separated by small sapphire plates and surrounded by fixation rings which keep them from falling apart. To avoid deterioration of the quality factor of the connected detector circuits, the insulator rings between the PT correction and ring electrodes are made from quartz-glass[29] while the other insulators consist of sapphire. In order to achieve a concentric alignment during cool-down all PT electrodes are shrinking onto the **outer** surface of the insulator rings. This prevents highly unwanted misalignments which, considering the large size of the PT, otherwise could amount up to 80 µm per electrode.

4.7.3 Analysis Trap

The analysis trap serves as a spin-state detector utilizing the Continuous Stern-Gerlach Effect (see chapter 3.2.6). To increase the spin flip induced axial frequency shift (equation 3.68) and thus enable an unambiguous spin flip detection (especially for heavy and/or boron-like systems) the ALPHATRAP AT features a strong magnetic bottle term of $B_2 \approx 45\,000\,\mathrm{T/m^2}$ exceeding it's predecessor experiment[30] by a factor of ~ 4.5. This is achieved with a highly permeable ring electrode made from a CoFe alloy (VACOFLUX 50) having a saturation magnetization of $B_s \approx 2.35\,\mathrm{T}$. Furthermore, since $B_2 \propto B_s/r^2$ the AT trap radius measures only 3 mm. This is about the lower limit for the transmission of millimeter-waves with ~36 GHz corresponding to the Larmor frequency of boron-like systems (in the AT). However, due to the small dimensions (and operation voltage, see chapter 5) the AT is also more sensitive to patch potentials. For this reason the inner surface quality of the AT was additionally improved by plasma polishing. In contrast to the high-precision frequency measurements in the PT, the spin state analysis in the AT relies on the detection of relative frequency shifts and is thus less affected by systematic shifts as long as they are sufficiently stable (see also 3.2.6). Therefore, the AT features a simpler 5-electrode design with only one pair of correction electrodes. Frequency coupling and excitation of the ion motion in the AT is made possible by a vertically bisected electrode sitting above the upper endcap.

The major source of magnetic field inhomogeneity in the PT are residual parasitic field gradients which are caused by the AT ferromagnetic ring electrode. These are reduced by a suitably positioned ferromagnetic (VACOFLUX 50) compensation ring, resulting in $B_2^{PT} \approx 0.06\,\mathrm{T/m^2}$ and $B_1^{PT} \approx 2.6\,\mathrm{mT/m}$ (see chapter 6).

4.7.4 Millimeter-Wave Incoupling

The heretofore discussed g-factor measurement principle involves the measurement of the bound electron Larmor frequency via spin spectroscopy i.e. by interrogating the expected Larmor spin transition frequency with suitable rf-excitations. For our experimental setup (with $B \approx 4.02\,\mathrm{T}$ in the PT) the typical Larmor frequencies reach

---

[29] In our frequency range quartz has a smaller permittivity ($\epsilon_r \approx 4$) and loss tangent ($\tan\delta \approx 4 \cdot 10^{-5}$) than sapphire ($\epsilon_r \approx 9$, $\tan\delta \approx 2 \cdot 10^{-4}$).

[30] A comparison to the Mainz AT and the associated axial frequency jumps was already given in chapter 3.2.6

up to ∼112 GHz for lithium- and hydrogen-like systems and ∼37 GHz for boron-like systems (in the PT), which is in the millimeter-wave[31] regime. Millimeter-waves (MW) are generated by an Anritsu MG3694C MW synthesizer equipped with an active multiplier OMLS10MS downstream and transported with waveguides towards the apparatus. The MW and laser incoupling system is shown in figure 4.11.

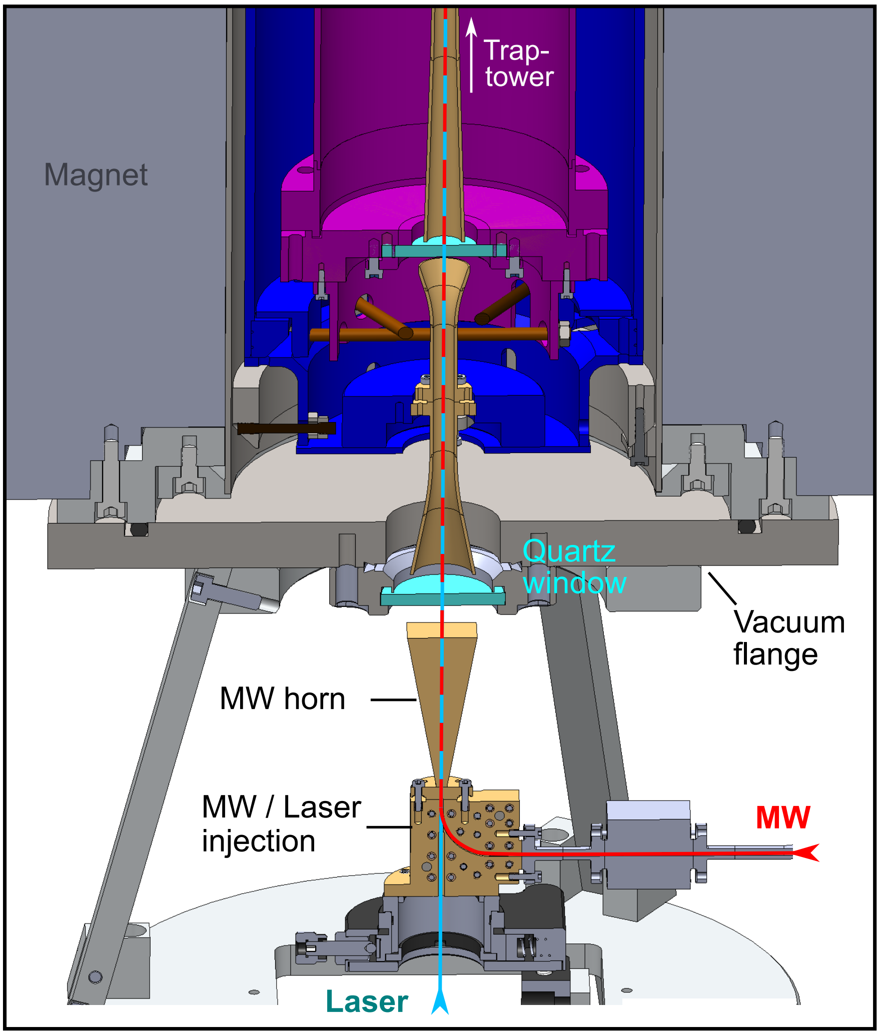

Figure 4.11: Drawing of the millimeter-wave and laser incoupling system. MW are injected axially into the trap via horn-to-horn tranmission through hermetically sealed quartz windows (light blue). The MW guide sections are thermally anchored to the respective temperature stages. Next to the MW the setup allows to introduce a laser beam through the waveguide into the trap via a pin-hole in a custom 90° MW bend (see text) [124]. The VESPEL fixation rods (brown) of the 77K shield and 4K insert are also visible.

---

[31] Colloquially also referred to as microwaves.

In contrast to the Mainz g-factor experiment at ALPHATRAP the MW have to be introduced from below the magnet, since the upper entrance is occupied by the beamline connection. Furthermore our MW injection system includes the possibility to additionally shine in a laser beam, e.g. for laser cooling or spectroscopy of the trapped ion. To this end the laser is introduced into the waveguide via a hole in a dedicated 90° waveguide bend[32][124]. Before they arrive in the trap chamber the MW (and the laser beam) have to pass through the three different temperature/pressure stages of our setup (300K, atmosphere → 77K, prevacuum → 4K, trap chamber vacuum). Thermal decoupling and vacuum sealing between the stages is achieved by transmitting the MW through two vacuum windows via two pairs of facing horn antennas. Both windows are made from quartz glass (fused silica) which provides good transmission for the MW as well as laser light frequencies up to near UV. It is noteworthy, that while the magnet-flange window is commercial (CF type), the lower trap chamber-flange window is realized with a round quartz glass plate sealed with indium. Despite this relatively simple construction, no impairment of the vacuum has been observed so far. After passing the trap tower the MW are absorbed/damped by a dielectric cone made from TECAPEEK[33]. This shall avoid possible reflections and thus unpredictable behavior of the MW amplitude at the ion position. Further information on the ALPHATRAP millimeter wave injection system can be found in [124] while the laser setup design is addressed in [19].

---

[32] This is not trivial since the hole can cause a major deterioration of the MW transmission, especially when the MW wavelengths are comparable or smaller than the size of the hole. While at ∼37 GHz a simple hole in a commercial waveguide bend is enough, at ∼112 GHz a custom-made directional coupler has to be used to allow for adequate MW transmission [124].

[33] carbon nanotube filled PEEK

5 Electronic Detection System

The electronic detection system can be considered as the nervous system of our experiment providing the readout and manipulation of the particle dynamics in the Penning-trap. In the following the essential building blocks of the detection system with a special focus on the cryogenic electronics will be discussed. Parts of this chapter can be also found in [65].

5.1 Cryogenic Detector Circuits

All measurement schemes performed at ALPHATRAP are based on the non destructive detection of tiny image currents via highly sensitive resonant detection circuits as introduced in chapter 3.2.4. For this purpose each trap is equipped with it's own axial detector, one for the high-precision frequency measurements in the PT and one for spin state detection/spectroscopy in the AT. Additionally the PT also includes a cyclotron detector for direct measurement and cooling of the reduced cyclotron mode.

Operating at cryogenic temperatures significantly reduces electronic noise and enables the implementation of low-loss superconducting resonators in order to maximize the detection efficiency. The sensitivity of a detector circuit is characterized by it's signal-to-noise ratio (SNR). This again depends on the respective detection method, as will be briefly discussed in the following.

5.1.1 Signal-to-Noise Ratio

The SNR can be derived by considering the complete equivalent circuit of a resonant detector as shown in figure 5.1. Here, the electronic noise contribution of the cryogenic amplifier is modeled by input related voltage- and current-noise sources u_{en} and i_{en}. The input impedance of the amplifier is determined by it's input capacitance C_{in} and input resistance R_{in}. To reduce the influence of the amplifier's imperfect input characteristics (impedance and noise) it is decoupled from the resonator by tapping the resonator coil winding according to an autotransformer[1]. In combination with an additional coupling capacitance C_c the overall signal transformation is given by the coupling constant

$$\kappa = \kappa_L \kappa_C \approx \frac{L_2 + M}{L} \frac{C_c}{C_{in} + C_c} \tag{5.1}$$

---

[1] The primary and secondary winding of an autotransformer are parts of a common winding and thus not galvanically isolated.

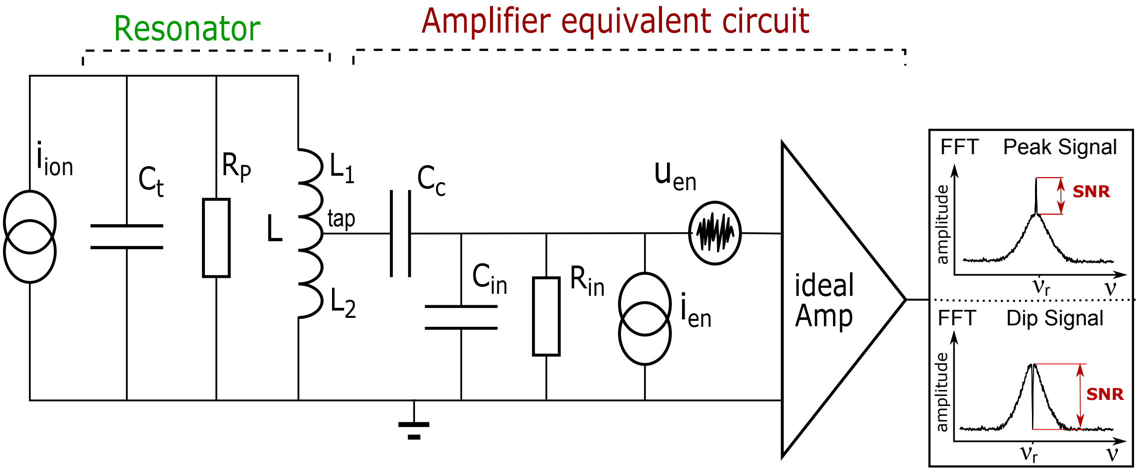

Figure 5.1: Equivalent circuit of the detection system. The capacitance C_t includes the trap electrode, resonator and cable capacitance. A hot ion is modeled with a current source (as shown here) or a series LC circuit in case the ion is thermalized (see 3.2.4). The electronic amplifier noise is modeled by voltage/current noise sources at the input of an ideal amplifier. C_c denotes a coupling capacitance while C_{in} and R_{in} are the amplifier input capacitance and resistance. Modified from [76].

where L is the total coil inductance and M denotes the mutual inductance between the partial inductances L_1 and L_2 (figure 5.1).
The definition of the SNR in general depends on the chosen detection technique.

Peak Detection For the detection of a hot ion, which appears as a sharp peak signal on top of the thermal noise resonance of the resonator (see figure 5.1), the SNR is given by the ratio of the ion's signal amplitude (voltage drop across the effective parallel resistance[2] $R_p^* \equiv (\frac{1}{R_p} + \frac{\kappa^2}{R_{in}})^{-1}$) and the sum of all thermal and electronic noise sources

$$SNR_{Peak} = \frac{i_{ion}\kappa R_p^* \sqrt{\tau_{meas}}}{\sqrt{4k_B T R_p^* \kappa^2 + u_{en}^2 + (i_{en} R_p^* \kappa^2)^2}} \approx \frac{i_{ion}\sqrt{R_p^* \tau_{meas}}}{\sqrt{4k_B T}}, \tag{5.2}$$

where in the last step the electronic noise contributions of the cryogenic amplifier are neglected by choosing an optimal noise matching $\kappa = \sqrt{\frac{u_{en}}{i_{en} R_p^*}}$ [126].
Regarding equation (5.2) SNR_{Peak} (for a resonant ion) can be increased by either decreasing the detector temperature or increasing the ion current (ion oscillation amplitude) which however can lead to systematic frequency shifts. Interestingly, for the detection of an exponentially decaying ion signal (i.e. without additional excitations) changing R_p will not affect SNR_{Peak} because the measurement time τ_{meas} scales proportional with the cooling time constant and therefore $\tau_{meas} \propto \frac{D_{eff}^2}{R_p^*}$.

---

[2] R_p^* already includes the reflected (transformed) amplifier input resistance [125].

Dip Detection For the detection of a cold ion dip which is in resonance with the detector circuit, the SNR is derived from the visible depth of the dip feature. It corresponds to the amplitude of the noise resonance (sum of all noise contributions, see figure 5.1) divided by the voltage noise floor u_{en} of the amplifier[3]

$$SNR_{Dip} = \frac{\sqrt{4k_B T R_p^* \kappa^2 + u_{en}^2 + (i_{en} R_p^* \kappa^2)^2}}{u_{en}}. \tag{5.3}$$

From equation (5.3) it can be seen, that for a high SNR_{Dip} it is important to keep the voltage noise contribution as small as possible while R_p^* should be maximized by optimizing the resonator quality factor. Although it is also possible to increase SNR_{Dip} by elevating the temperature or the current noise, this will in general result in higher particle temperatures leading to unwanted systematic shifts. The same applies when κ is excessively increased since this simultaneously translates into a higher[4] (noise current induced) effective voltage noise $u_{en}^{eff} = i_{en} R_p^* \kappa$ perceived by the ion. Apart from that, the coupling also influences the reflected parallel resistance R_p^* and thus the particle dip width which shouldn't be too small in order to allow to resolve the dip within a reasonable measurement time which is usually the case for a dip width on the order of a few Hertz.

5.1.2 Resonator Design Characteristics

In the previous section it was pointed out, that the equivalent parallel resistance $R_\mathrm{p} = Q\omega L$ is a figure of merit for a high signal-to-noise ratio and thus an efficient and fast ion detection. Electrically R_p represents the combined component losses of the resonant circuit. Close to the resonance frequency R_p can be approximately expressed in terms of the capacitor's equivalent series resistance (ESR)[5] and the inductor's equivalent winding resistance R_L [127]:

$$R_\mathrm{p} \approx \frac{L}{C(\mathrm{ESR} + R_L)}. \tag{5.4}$$

According to this relation R_p can be increased by minimizing the circuit parameters C, R_L and ESR and maximizing the inductance L. Typically, these quantities are not independent and are also partly restricted by the boundary conditions of the experiment. In order to reach maximal detection efficiency all ALPHATRAP resonators were therefore highly optimized in terms of their geometry and material selection. The detailed optimization process has been described in [76].

---

[3] This is because the achievable dip depth is only limited by the amplifier voltage noise and the frequency resolution. Actually, for an ideal amplifier without any electronic noise contributions the depth of the dip feature would be infinite (in an infinitely small frequency interval).

[4] In detail the behaviour depends on the relative size of R_p and R_{in}

[5] The ESR incorporates the capacitor's dielectric and conduction losses. Losses due to electromagnetic radiation of the tuned circuit are neglected.

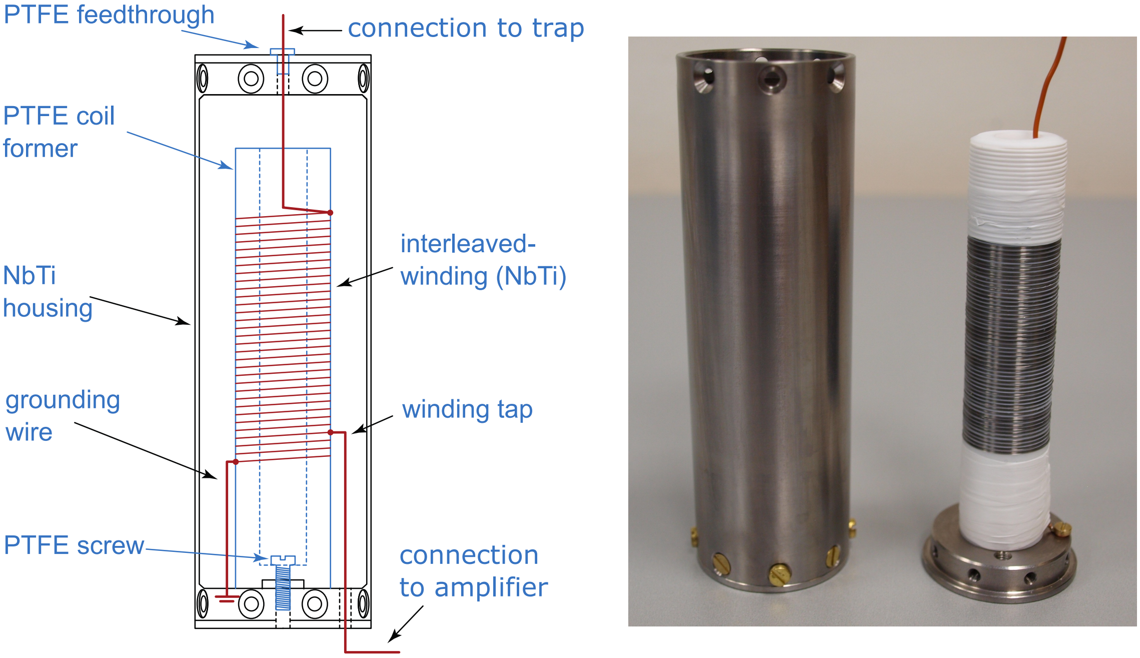

Figure 5.2: All ALPHATRAP resonators have a similar housing geometry. They are 12.8 cm long and have 4 cm outer diameter limited by spatial constraints of the experiment. The NbTi wire is arranged in a so-called interleaved winding which features a small parasitic winding capacitance. Modified from [76].

	PT	AT	PT-Cyclotron
N	684	1912	10
L	2.1 mH	10.5 mH	1.3 µH
C	5.1 pF	6.3 pF	4 pF
D_{eff}	29.3 mm	19.15 mm	18.77 mm
C_p loaded	28.4 pF	21.5 pF	29.4 pF
ν_r	651.4 kHz	335.1 kHz	25.7 MHz (^{12}C^{5+})
Q loaded	40000	7000	1800
R_p loaded	344 MΩ	155 MΩ	0.37 MΩ

Table 5.1: The circuit parameters of all ALPHATRAP detector circuits. N is the resonator coil winding number and C is the self-capacitance of the resonators. The loaded values correspond to the final cryogenic properties of the completed detector circuit, i.e. connected to the trap and the amplifiers and situated inside the magnetic field. The cyclotron resonator frequency can be tuned in situ by a varactor diode within 0.5 MHz

.

The resonators are realized as helical inductors wound on cylindrical coil formers and screened by cylindrical housings from external influences. All resonators have an identical housing geometry and mainly differ by the coil dimension and the used number of windings, which are free optimization parameters. These are chosen such that, taking into account the respective trap- and parasitic wire-capacitance, each detector reaches maximum R_p at the respectively desired operation frequency. All insulating parts including coil former and wire insulation are made from PTFE[6] due to its small permittivity (ϵ_r=2.1) and low loss angle ($\tan\delta = \mathrm{ESR} \cdot \omega C < 10^{-4}$) . The shield and the 75 µm thick wire are made from the type-II superconductor NbTi allowing for minimal conductive losses when operated below it's critical conditions. The resonators are positioned in a magnetic field of $B \approx 2$ T, which corresponds to a critical transition temperature of $T_\mathrm{c} \approx 8$K and is thus well above the typical operation temperature of ~4.5 K. The basic construction of the ALPHATRAP resonators is shown in figure 5.3. The circuit parameters of all detectors are summarized in table 5.1.

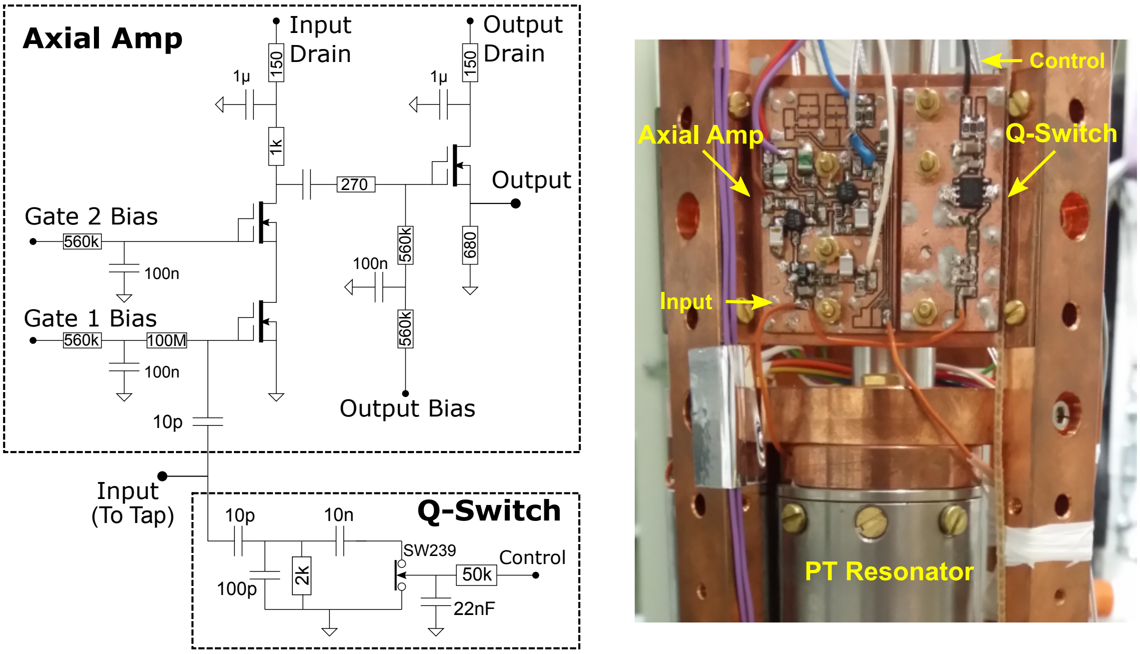

Figure 5.3: Circuit diagram and picture of the PT axial amplifier and Q-switch. In low-Q mode the Q-switch is open and the effective parallel resistance is limited by the parallel impedance of the snubber (damping) circuit. In high-Q mode the switch is closed and shorts the damping resistor to ground (see text).

---

[6] Polytetrafluoroethylene or TEFLON

u_{en}	$\sim$1.1 nV/$\sqrt{\text{Hz}}$
i_{en}	<1 fA/$\sqrt{\text{Hz}}$
G_V	$\sim$14 dB
P_l	$\sim$3 mW
$R_{in,AC}$	$\sim$ 20 MΩ
C_{in}	$\sim$ 2 pF

Table 5.2: Properties of the ALPHATRAP axial amplifiers. G_V denotes the voltage gain. Compared to earlier versions the total power consumption P_l was reduced from $\sim$ 10 to $\sim$ 3 mW by adding a separate drain bias to the output stage.

5.1.3 Axial Amplifiers

Each axial resonator is connected to its own cryogenic amplifier. Both axial amplifier circuits (see figure 5.3) are identical and based on a design discussed in [83]. As transistors, GaAs MESFETs[7] are used. These are still functional even at cryogenic temperatures[8] and also feature a high input impedance and low noise characteristics [83]. Care is taken in order to keep the amplifier's parasitic influence on the resonator as small as possible. The input stage is therefore designed in a discrete common-source cascode configuration [83]. This significantly reduces the amplifier's back-action on the resonator's quality factor caused by the parasitic Miller capacitance [129]. A source follower in the output stage provides impedance matching to the coaxial lines used for signal transport. Compared to the unloaded resonator the axial amplifiers have a relatively small effective input resistance of about 22 MΩ at their operation frequencies. For this reason both ALPHATRAP axial amplifiers are decoupled from the resonators by tapping the resonator coils according to an autotransformer (as previously described) with winding ratio $N_\text{S}/N_\text{P} \approx 1/10$ where N_S denotes the secondary winding number and N_P the primary (total) winding number. The properties of the axial amplifiers are summarized in table 5.2.

5.1.4 PT Axial Detector

The PT axial detector is connected to the lower PT endcap electrode having an effective electrode distance of 29.3 mm. The completely wired PT detector is designed with a final operation frequency of 651.4 kHz with the pickup electrode making the largest capacity contribution[9] ($C_{PE}^{PT} \approx$20 pF) to the overall circuit capac-

---

[7] metal-semiconductor field-effect transistor

[8] GaAs is less prone to charge carrier freeze out since it has comparably small activation energies of the donor/acceptor levels [128].

[9] This is a drawback of the rather large trap geometry.

ity[10] (C_{loaded} ≈28.7 pF). Being limited by a currently maximal reachable trapping voltage of $-100\,\mathrm{V}$, the chosen operation frequency enables the detection of ions with $q/m > 1/4$. For example, the detection of hydrogenlike lead ($q/m \approx 0.39$) would require a trapping voltage of ∼63 V.
For the non-coherent dip detection, which is used during the axial frequency measurement in the PT, a high signal-to-noise ratio and therefore a high R_p is of great importance since it significantly reduces the necessary measurement time. On the other hand the statistical precision is limited by the line width of the dip signal which scales linearly with $R_\mathrm{p} \cdot q^2/m$ (equation 3.55) and is thus especially problematic for highly charged ions. To counteract this limitation and increase the scope of accessible charge states during one measurement campaign[11] our PT-detector was equipped with a dedicated Q-switch which allows to intentionally lower the Q-value and therefore R_p.

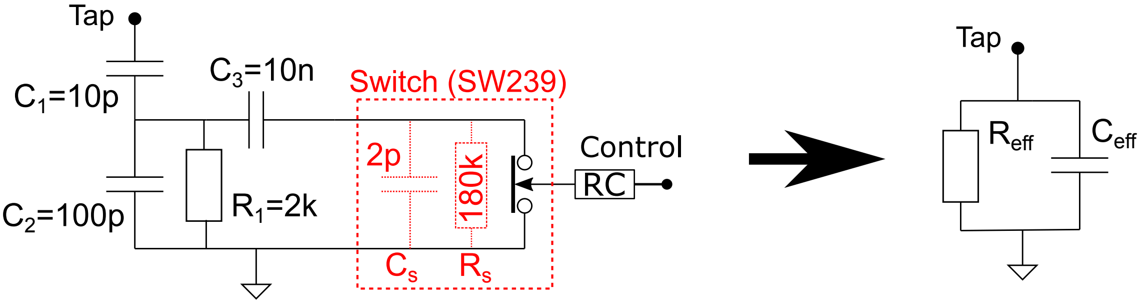

Figure 5.4: On the left side the complete Q-switch circuit is shown. The design is mostly independent of the parasitic switch properties (C_s, R_s) because $C_2 \gg C_s$ and $R_s \gg R_1$. The circuit behavior can be understood from the equivalent parallel circuit on the right side (see text).

Q-Switch

The working principle of the Q-switch is based on a variable attenuator (damping/snubber circuit) which is connected in parallel to the resonator tap. The attenuator can be switched between a non dissipative and a dissipative state in order to lower the total effective parallel resistance of the detector circuit. The switching is done by a solid state GaAs switch (*MACOM* SW239)[12] by applying a separately filtered control voltage. Referring to figure 5.1.4 the circuit is designed such that it is mostly independent of the parasitic switch properties (C_s, R_s) which are neglected in the following considerations. The circuit behavior can be understood

---

[10] The residual capacity is contributed by the trap chamber feedthrough (∼2.3 pF) and parasitic wire capacitance (∼1 pF).

[11] In principle the SNR vs. dip width optimization for ions with specific $\frac{q^2}{m}$ can be also achieved by a proper ion or resonator decoupling, however this can not be easily adjusted in situ. Furthermore the Q-switch also enables systematic checks of the lineshape influence.

[12] Actually the SW239 IC includes two GaAs switches which we connect in parallel in order to half the series resistance.

from an equivalent impedance transformation as shown in figure 5.1.4. In high-Q (HQ) mode the Q-switch is closed and the damping resistor R_1 is ac-wise shorted by the large coupling capacitance C_3. Using standard linear circuit analysis methods the effective parallel resistance and capacitance of the equivalent circuit can be calculated.

$$R_{eff}^{HQ} = \frac{(\omega R_1)^2(C_1+C_2+C_3)^2+1}{(\omega C_1)^2 R_1} \tag{5.5}$$

$$C_{eff}^{HQ} = \frac{R_1\omega^2 C_1(C_2+C_3)(C_1+C_2+C_3)+C_1}{R_1\omega^2(C_1+C_2+C_3)^2+1} \tag{5.6}$$

where ω is the operation frequency ($\omega_r^{PT} \approx 2\pi \cdot 651.4\text{kHz}$). Equations (5.5) and (5.6)) can also be easily adopted for the case when the Q-switch is in low-Q (LQ) mode by setting $C_3 = 0$. The Q-switch is connected to the resonator tap. Thus, for the calculation of the reflected impedance appearing across the resonator, the inductive decoupling constant of the PT resonator $\kappa_L^{PT} \approx 0.08$ has to be taken into account

$$R_{eff}^r = R_{eff}/\kappa_L^2 \quad \text{and} \quad C_{eff}^r = C_{eff}\cdot\kappa_L^2. \tag{5.7}$$

Table 5.3 summarizes the calculated reflected capacitance and resistance which are "seen" by the resonator when the Q-switch is in HQ- or LQ mode. With this, the resulting Q-values and resonance frequency shift[13] of the complete detector can be calculated:

$$Q = \frac{R_p||R_{eff}^r}{2\pi\nu_r L} = \frac{R_p \cdot R_{eff}^r}{R_p + R_{eff}^r}\cdot\frac{1}{2\pi\nu_r L} \tag{5.8}$$

$$\Delta\nu_r = \nu_r \cdot \frac{\Delta C_p}{2C_p} = \nu_r \cdot \frac{C_{eff}^r}{2C_p} \tag{5.9}$$

where R_p, C_p are the loaded effective parallel resistance and capacitance of the PT detector without the Q-switch (given in table 5.1). In HQ mode the reflected resistance of the Q-switch is almost three orders of magnitude higher than R_p and the Q value stays virtually unchanged [14] at 40000. The unavoidable frequency drop due to the additional parasitic capacitance of the Q-switch amounts 736 Hz. This is smaller than the typical frequency variations observed between successive cooldowns due to thermal contraction processes of the resonator[15]. In LQ mode the effective parallel resistance of the Q-switch is chosen such that $R_p||R_{eff}^r \approx 67.8\,\text{M}\Omega$ or $Q \approx 7900$. Thus, compared to the HQ mode the 3dB bandwidth of the resonator ($\Delta\nu_{3dB} = \frac{\nu_r}{Q}$) is increased while the particle dipwidth is decreased by a factor of $\frac{40000}{7900} \approx 5.1$. Due to switching, the parasitic capacitance of the Q-switch slightly changes. The resonance frequency shift between LQ and HQ mode amounts only $736\,\text{Hz} - 704\,\text{Hz} = 32\,\text{Hz}$ (see table 5.3 and figure 5.5). Figure 5.5 shows the effect of the Q-switch on the noise resonance of the PT detector and the dip width

---

[13] Compared to the PT detector without the Q-switch.

[14] It drops by only $\sim 1‰$.

[15] These are typically on the order of ~1kHz but can be considerably higher if e.g. the resonator-trap connection cable is slightly displaced with respect to ground reference.

	R^r_{eff}	$R_p \vert\vert R^r_{eff}$	Q	$\Delta C_p = C^r_{eff}$	$\Delta\nu_r$
HQ-Mode	~319 GΩ	~344 MΩ	~ 40000	~63.9 fF	-736 Hz
LQ-Mode	~84.4 MΩ	~67.8 MΩ	~ 7900	~61.4 fF	-704 Hz

Table 5.3: Additional reflected capacitance $\Delta C_p = C^r_{eff}$ and resistance R^r_{eff} appearing across the resonator when the Q-switch is in *HQ*- or *LQ* mode (see text). The resulting Q values and the frequency shift of the complete PT detector circuit are also shown.

of a single Ar^{13+} ion. In high-Q mode the complete PT-detector features a SNR of 24 dB at a loaded Q-value of ~40000 (R_p ~344 MΩ). According to equation 3.55 this translates into a dip width of ~4.1 Hz for a single Ar^{13+} ion. In *LQ* mode the noise resonance widens and shifts by ~31 Hz. The SNR drops to ~15 dB as expected[16] from equation 5.3. The dipwidth decreases to ~0.8 Hz. The Q-Switch is also switched to low-Q mode during particle creation/preparation since it also facilitates the initial particle detection and sideband cooling of hot ions. It also increases the cooling time constant and enables an extension of the evolution time during phase resolved detection.

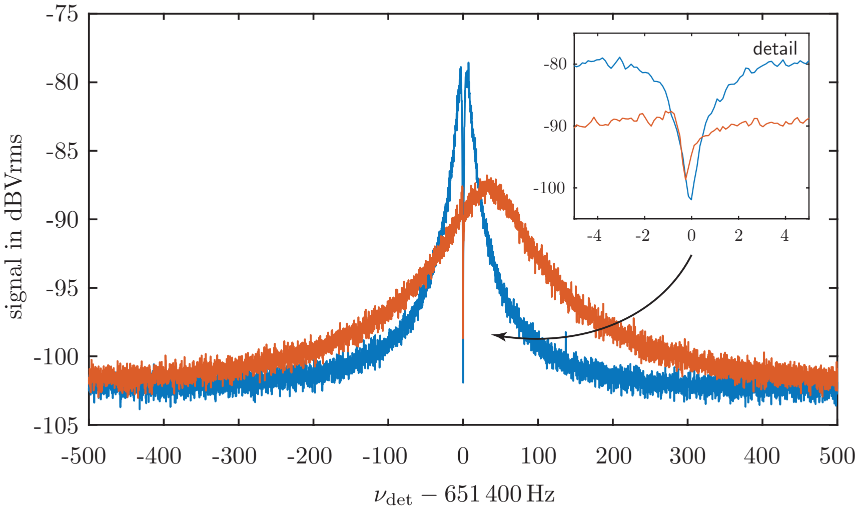

Figure 5.5: Noise resonance of the PT detection circuit in high-Q (blue) and low-Q (orange) mode. In low-Q mode R_p and therefore also the width of the visible Ar^{13+} ion dip is reduced by a factor of ~5. The parasitic capacitance of the active Q-switch shifts the detector's resonance frequency by about 31 Hz. The small shift of the ion frequency visible in the detail can be explained by a thermalisation related drift of the (not yet temperature stabilized) trap voltage source which occurred during the measurement time of the two resonances.

---

[16] Compared to PT amplifier the voltage and current noise contribution of the Q-switch can be neglected.

5.1.5 AT Axial Detector

Compared to the PT the AT detection circuit is designed for a lower detection frequency of approximately 335.1 kHz. The lower frequency improves the detection of spin-flips in the AT since according to equation (3.68) the spin flip induced axial frequency jump in the AT scales with $1/\nu_z$. However, the detection frequency also can't be chosen too small because this would also imply a lower trapping voltage an thus an increased influence of patch potentials which could potentially impair the harmonicity of the AT. The value is also the lower frequency limit without sacrificing SNR due to the amplifiers $1/f$ noise [83]. To achieve the lower resonance frequency the AT resonator coil includes 1912 windings which are arranged in a special interleaved winding (chamber winding) configuration with a low intrinsic capacitance. This results in an inductivity of 10.5 mH which is ∼5 times higher than for the PT detector while the self capacitances differ by only 1.2 pF (table 5.1). Compared to the PT-detector the AT-detector circuit has a lower quality factor of $Q^{AT} \approx 7000$ ($R_p^{AT} \approx 155\,\mathrm{M\Omega}$). On the one hand this can be attributed to the higher conduction losses due to the larger winding number. On the other hand because of technical reasons the AT resonator is wound with FORMVAR[17] insulated wire. FORMVAR shows considerably higher dielectric losses ($\tan\delta \approx 3 \cdot 10^{-4}$) [130] than PTFE, which was used for the PT winding.

A special feature of the AT detector is the additional implementation of a frequency switch (see figure 5.6). It is based on a capacitor with $C_{FS} = 100\,\mathrm{pF}$ which can be switched in parallel to the AT resonator tap in order to shift it's resonance frequency by ∼ 10 kHz (∼200x the 3 dB-bandwidth of the AT resonator). Being out of resonance with the resonator the ion damping by the real part of the resonator impedance is reduced and the cooling time constant of the ion is extended. This enables a longer evolution time and a smaller frequency uncertainty during phase sensitive measurements of the axial frequency fluctuations in the AT [104].

5.1.6 PT Cyclotron Detector

It is remarkable that in principle (utilizing sideband coupling) one axial detector per trap is sufficient for the determination of all eigenfrequencies. However, a dedicated cyclotron detector is useful for the direct detection as well as an efficient bolometric cooling of the modified cyclotron motion. Therefore, the PT is also equipped with a cyclotron detector circuit. It is connected to one side of the half split ring and inner correction electrodes which are capacitively interconnected within the trap chamber (see full schematic 5.7). Compared to the axial detectors the cyclotron detector

---

[17] Compared to PTFE, FORMVAR is mechanically more robust and thus less prone to shorts between adjacent windings. Such winding shorts typically occur due to mechanical tensions during thermal cycling and are the most common resonator defects especially when the winding number is large, as is the case for the AT resonator. Winding shorts are best avoided by a durable insulation or sufficient distance between turns which is however limited by space constraints of the setup. In this context an improved AT coil former design with a PTFE insulated winding will be tested in the near future.

circuit is optimized for much higher operation frequencies on the order of 20 MHz to 30 MHz depending on the ion's charge-to-mass ratio (equation 3.5). Just as the axial resonators the cyclotron resonator also features a helical coil geometry and is built into a similar NbTi housing. Due to the comparably high frequency the coil includes only 10 windings made from multistranded NbTi wire. Using multiple thin insulated wires instead of a single thick wire reduces conduction losses caused by the skin effect. Since at 300 K NbTi has a considerable specific resistance of $\rho_s \approx 0.7$ µΩ cm[131] this measure ensures a normal conducting quality factor of $Q \approx 80$ and allows for easier frequency adjustment during maintenance at room temperature. The cyclotron amplifier is based on a design discussed in [95].

For later *in situ* frequency tuning the cyclotron detector is equipped with a capacitively decoupled varactor diode. It allows for a compensation of typical frequency shifts on the order of ∼0.5 MHz caused by thermal contraction processes during the cooldown and thermalisation of the experiment. It also enables an adjustment of the cooling time constant during phase resolved detection of the modified cyclotron frequency [22] and reduces the effect of frequency pulling (i.e. the image current shift, see section 3.2.4) when it is used to detune the resonator.

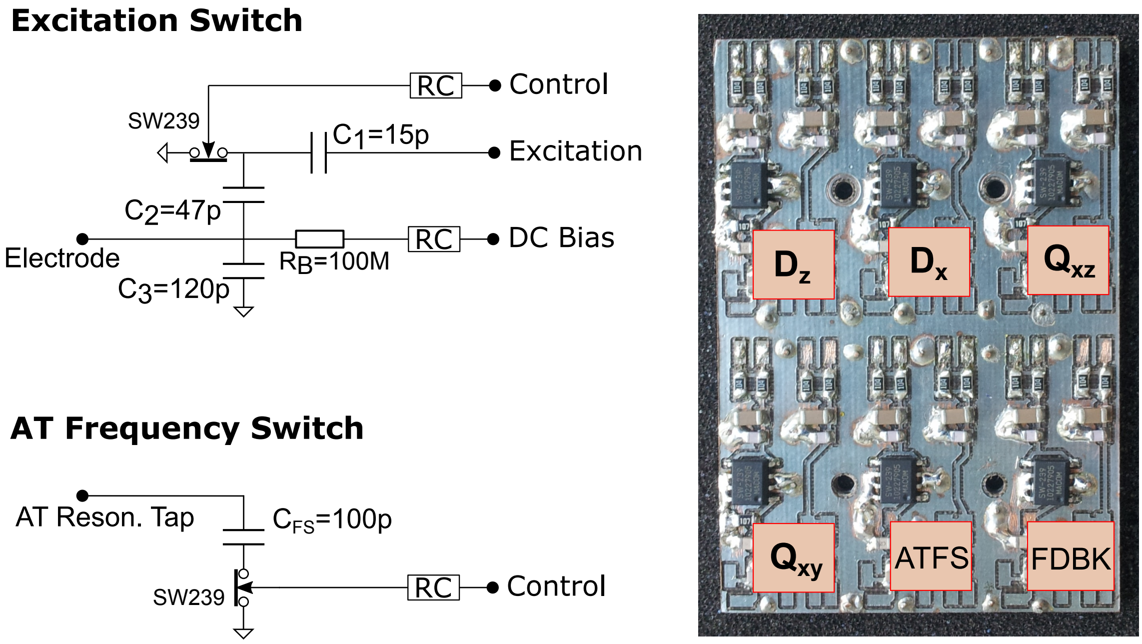

Figure 5.6: All excitation lines (D_z, D_x, Q_{xz}, Q_{xy}) including the feedback (FDBK) are controlled by the basic excitation circuit shown on the top left. The AT frequency switch (ATFS) is currently also located on the excitation board (right side). The control and bias voltages are pre-filtered by the basic RC-filter circuit shown in figure 5.9.

5.1.7 RF-Excitation Board

For the excitation and frequency coupling of the individual particle eigenmodes the ALPHATRAP experiment is fed by 5 excitation lines including two dipolar (D_z and D_x) and two quadrupolar (Q_{xz} and Q_{xy}) excitations which are connected to the PT. A Q_{xz} excitation in the AT is made possible by tapping the PT Q_{xz} line with a 220 pF capacitor inside the trap chamber. Additionally, electronic feedback (FDBK) can be applied through a shared excitation line, which is weakly coupled to the inputs of all resonant detector circuits via 0.3 pF capacitors. The layout of all excitation lines and the detailed connection to the AT and PT is shown in the schematic of the complete trap tower in figure 5.7. All excitation lines are connected to the trap electrodes via cryogenic switching circuits. With these, each line can be shorted to ground when it is not needed. This allows for an effective reduction of radio frequency noise entering through the lines [83]. The basic circuit of a cryogenic excitation switch is shown in figure 5.6. The switching circuits are based on the same GaAs solid-state switch (SW239) which has also been used in the PT Q-switch (see section 5.1.4) and the AT frequency switch. In "on" state, i.e. during the application of an excitation signal the switches are high ohmic ($\sim 180\,\mathrm{k\Omega}$) such that the signal is passed on to the excitation electrode. At 30 MHz the signal and therefore also the noise attenuation difference between "on" and "off" amounts >40 dB.
The excitation is applied through a capacitive voltage divider (C_1, C_2, C_3) with a splitting ratio of $\sim 1/10$[18] which enables relative noise reduction[19]. The excitation switch circuit already contains the DC biasing for the respective excitation electrode. A radio frequency blocking resistors (R_B) protects the excitation signals from being AC-wise shorted to ground by the bias RC-filter capacitor. Split electrode pieces are connected (biased) by another blocking resistor within the trap chamber as shown in figure 5.7. The excitation switches are placed on a common "excitation board", which currently also holds the AT frequency switch[20]. The signal crosstalk between the individual switching circuits has been measured to be <-60 dB at 30 MHz.

5.1.8 Charge Sensitive Detectors

Efficient dynamic capturing of externally produced HCI in the capture section requires precise information on the energy and arrival time of the ion bunch on the order of microseconds. For this purpose ALPHATRAP is equipped with two cryogenic charge sensitive detectors. As Faraday cups the diaphragm at the upper end of the trap tower (FC1) with a capacitance[21] of $C_{FC1} \approx 12$ pF and the microwave horn

---

[18] $\sim 4/10$ for electronic noise generated by the switch

[19] The noise and the signal amplitude are both attenuated by the voltage divider by $\sim 1/10$, however, the signal attenuation is compensated by applying a stronger (e.g. x10) excitation amplitude.

[20] For a clearer cable management and in order to reduce parasitic cable capacitance this should be changed in the future. Instead the frequency switch can be placed right next to the AT amplifier as shown in figure 5.7.

[21] including parasitic cable and feedthrough capacitances

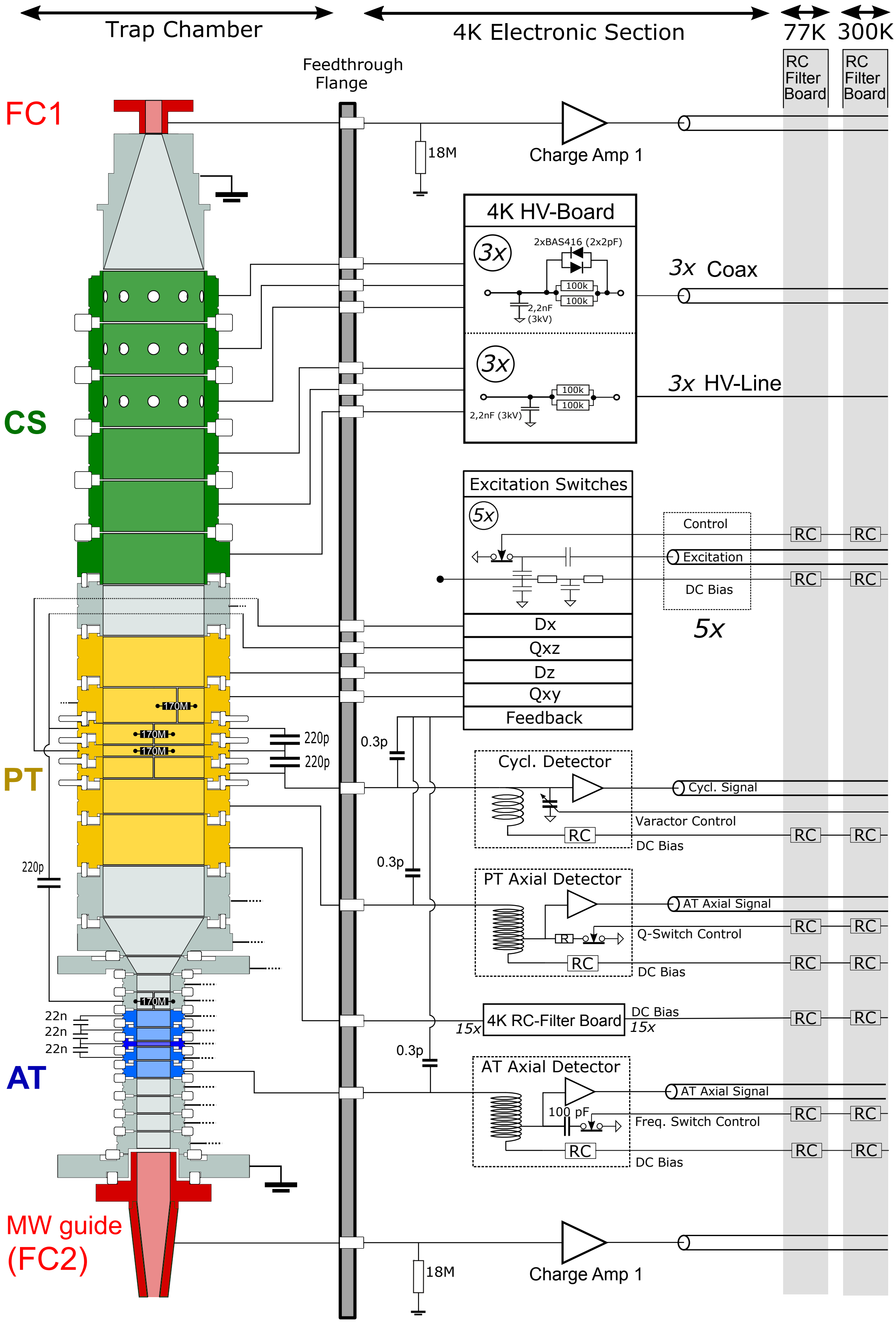

Figure 5.7: Simplified wiring diagram of the complete trap tower. Only essential components are shown. See text for explanation of individual components.

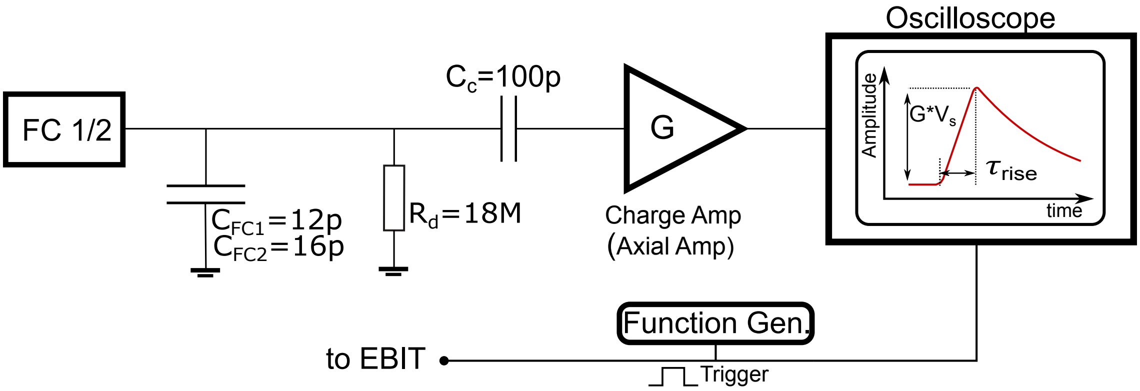

Figure 5.8: Basic circuit of the two charge sensitive detectors. The diaphragm electrode (FC1) and the MW horn (FC2) are used as Faraday cups. The charge amp is based on the axial frequency detector (see text). After the charge amp the signal is amplified at room temperature (not shown) and recorded with an oscilloscope which is synchronized with the EBIT ejection trigger pulse.

at bottom with $C_{FC2} \approx 16\,\mathrm{pF}$ are used. The basic circuit is shown in figure 5.8. The charge amplifiers are based on the cryogenic axial amplifier circuit shown in figure 5.3. Since this already comes with a high input impedance only slight modifications had to be made. The major difference are a larger coupling capacitor $C_c = 100\,\mathrm{pF}$ at the input and an additional discharge resistor $R_d = 18\,\mathrm{M\Omega}$ in parallel to the FC. This results in discharge time constants on the order of $\tau_d = R_d C_{FC} \approx 0.2 - 0.3\mathrm{ms}$ (depending on the FC) allowing for a maximum ion bunch injection (repetition) rate of up to $\sim 400\,\mathrm{Hz}$. Referring to the typical signal shape shown in figure 5.8, the signal rise time τ_{rise} corresponds to the temporal ion bunch length (time of flight distribution) while the total charge Q of the ion bunch determines the signal amplitude[22] with $V_S \approx Q C_{FC} \cdot G$, where G is the amplifier gain. In other words the output charge sensitivity V/Q can be expressed by the inverse capacity of the Faraday cup times the gain of the amplifier:

$$V/Q \equiv \frac{1}{C_{FC}} \cdot G. \tag{5.10}$$

For example at a measured gain of 14 dB the output charge sensitivity of the upper detector (FC1) amounts 418 mV/pC or 67 nV per elementary charge[23]. The properties of both charge sensitive detectors are summarized in table 5.4.

---

[22] Actually both is only true if $\tau_d \gg \tau_{rise}$ which holds in our case.

[23] With an output related amplifier noise of $5\,\mathrm{nV}/\sqrt{\mathrm{Hz}}$ and a bandwidth of 1 MHz the single shot detection threshold is ≥ 82 elementary charges.

	FC	C_{FC}	Gain (G)	V/Q
Charge Detector 1	diaphragm	12 pF	$\sim$ 14 dB	418 mV/pC
Charge Detector 2	MW horn	16 pF	$\sim$ 14 dB	394 mV/pC

Table 5.4: Properties of the two charge sensitive detectors (see text).

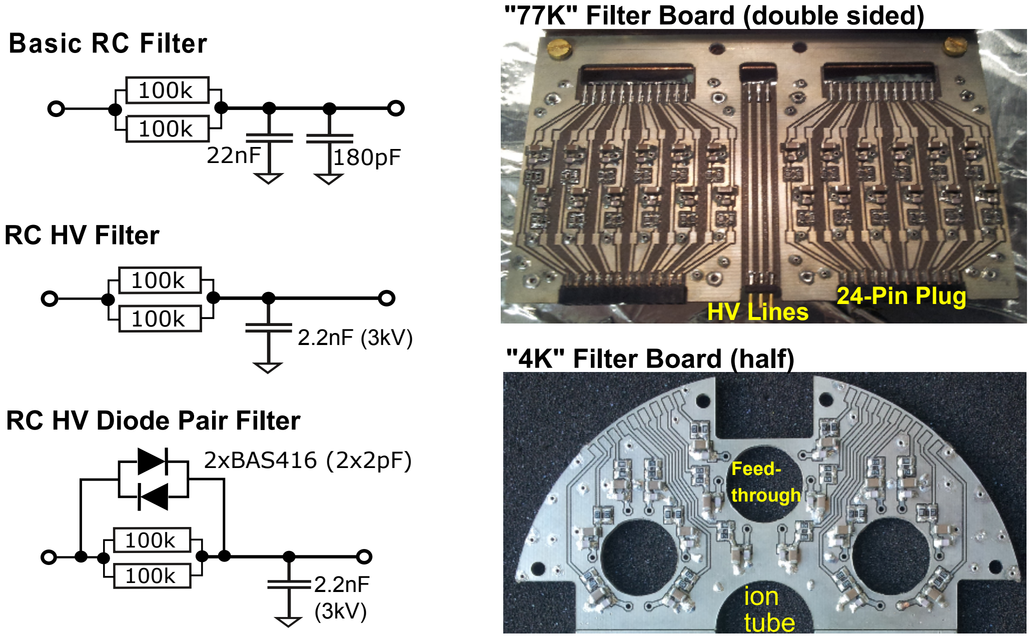

Figure 5.9: Low DC voltages are filtered by a serial connection of three filter stages ("300K"→"77K"→"4K" in which the most commonly used filter type is shown on the top left. The six electrodes in the capture section are filtered by dedicated HV filters. Fast switching of the first three electrodes is enabled by bridging the filter resistors with antiparallel diode pairs (see text). The double sided "77K" filter board is attached to the 77K hat shield and is equipped with 48 filters connected via 24-pin connector plugs. It also provides thermal anchoring of the DC-HV lines. The circular "4K" filter board, of which a half piece is shown, sits on top of the upper trap chamber flange and is equipped with cutouts for the ion tube and the total of 6 multipin feedthroughs.

5.1.9 Filters and Wiring

DC-Biasing Filters

On their way to the trap electrodes and cryogenic electronics the DC lines run through three RC lowpass filter stages (filter boards) located at 300 K, 77 K and 4.2 K which are connected in series. The filter boards also provide thermal anchoring of the lines at the respective temperatures.

Each filter includes two parallel[24] 100 kΩ metal film resistors. As capacitors a parallel connection of a 22 nF (200V proof) and a 180 pF (250V proof) is used[25]. Each filter has a cutoff frequency of ∼ 144 Hz while the serial connection of the three successive filter stages results in an effective cutoff frequency[26] of 28 Hz. The effective filter time constant is 6.8 ms enabling a smooth adiabatic transport (chapter 6.4) between the traps. The high voltages needed in the capture section are filtered by dedicated HV filters on a separate HV board. The filters of the first three switchable capture electrodes are bypassed with antiparallel diode pairs (BAS416)[27]. They enable a fast switching (∼1 µs) of voltages exceeding the diode threshold voltage (this increases from ∼0.7 V at 300 K to ∼1.6 V at 4.2 K) while typical noise amplitudes are still filtered by the RC filter.

Components

At cryogenic temperatures only certain electronic components can be used. Especially suitable are NPO (COG) type ceramic multilayer capacitors which have a low ESR and keep their nominal capacitance within 1 % down to 4 K [132]. Where larger capacitance values are needed, polyphenylene sulfide (PPS) film capacitors are used. Suitable resistors are metal film resistors having low-noise characteristics and good temperature stability [133]. Generally, the use of carbon film resistors should urgently be avoided due to their strong temperature dependence, although this can be exploited for the design of sensitive temperature sensors as has been shown in chapter 4.5.2. At ALPHATRAP additional care was taken to use as nonmagnetic components as possible, especially those which are positioned close to the PT within the trap chamber, have been carefully preselected[28].

---

[24] For reasons of redundancy: In case one resistor or connection breaks (i.e. becomes high ohmic) the filter will still work, albeit it's cutoff frequency will be doubled.

[25] The smaller capacitor has a lower parasitic inductance and thus improves the high frequency performance of the filter.

[26] Since the filters influence each other, the effective cutoff frequency is calculated from the common transfer function of the combined filters.

[27] This high doped Ge diode is still operational at 4K. Additionally it has a comparably small parasitic zero bias capacitance of 2.2 pF. This diode type was suggested to us by Stefan Stahl.

[28] Some manufacturers offer special non magnetic components where no ferromagnetic materials such as nickel are used in the galvanization process. However, these components rarely fulfill the additionally required temperature stability and high quality factors.

Wiring

The trap and the cryogenic 4K electronics are supplied with 48 low-voltage DC-lines made from 0.1mm thick manganin wire. The wires are arranged in two strands of cryo loom cable with 24 (12 twisted pairs) individual wires per strand. The highly insulated HV lines for the CT and temperature sensor wires are separately installed. All wires are connected to vacuum feedthroughs in the hat flange and are thermally anchored via the 77K hat shield filter board (figure 5.9) before they are guided down into the 4K electronic section. Here the two low voltage cryo loom cable strands are connected to two "distribution boards" from where the voltages are distributed to the 4K filters and amplifiers via normal stranded copper lines[29]. The AC signals[30] are transported via 13 cryogenic coaxial cables made from stainless steel due to it's low thermal conductivity (table 4.1 in section 4.5.1). As the DC lines, the AC lines are thermally anchored on a 77K hat shield "AC-board".

Quality Factor-Loss Sources

Due to the high number of components involved, the final wiring of the trap and the connection to the detection electronics is not trivial but requires a thorough planing. Apart from an optimization of the quality factors of the isolated detector circuits special care must be taken when connecting the detectors to the trap. This is because even the best optimized detection circuit can be impaired by parasitic interactions with adjacent circuit components which can potentially result in lossy configurations that are in general frequency dependent. Especially critical are electrodes which are next or close to pickup electrodes due to their rather large coupling capacitance of up to $C_c^{PT} \approx 10\,\mathrm{pF}$ between adjacent electrodes in the PT. To give a simplified example: Assuming the next electrode to the PT axial detector pickup-electrode would be connected to ground via some resistor R_g and thus in series with C_c^{PT}. This series RC circuit adds an additional effective resistance R_{eff} in parallel to the PT resonator with

$$R_{eff}(R_g) = \frac{1}{R_g(2\pi\nu_z C_c^{PT})^2} + R_g, \tag{5.11}$$

where $\nu_z \approx 651\,\mathrm{kHz}$ is the axial detector frequency. Equation 5.11 has a minimum at $R_g = \frac{1}{2\pi\nu_z C_c^{PT}}$ such that R_g must be either chosen very small ($R_g < 1\,\Omega$) or very large ($R_g > 1\,\mathrm{G\Omega}$) in order not to limit[31] the quality factor of the PT resonator. In this way the filters and other circuitry connected close (i.e. with strong coupling) to the detector pickup electrodes have to be optimized to achieve a high effective parallel resistance. The layout of the ALPHATRAP wiring is designed with the focus to avoid any extra loading of the detector circuits. Here the main limitation of

---

[29] During maintenance work the distribution boards allow for an easier and save handling, since the soldering is done to the stable copper lines and not to the highly fragile cryo loom connections.

[30] 5x excitations, 5x detector outputs including charge amps, 3x switchable CT electrodes

[31] Note, that this also depends on the size of C_c.

the wired PT detector quality factor of ~ 40000 (in high-Q mode) is given by the ceramic multipin feedthrough in the upper trap chamber flange.

5.2 Roomtemperature Electronics

5.2.1 Electronic Boxes

The room temperature electronics is located in 5 aluminum boxes each of which is connected to a 32pin vacuum feedthrough in the vacuum vessel hat. The boxes are organized as follows:

- **2 RC-Filter Boxes** The room temperature RC filters are distributed over two "DC boxes" such that the current carrying supply lines of the cryogenic amplifiers are separated from high-precision voltage supply lines of the PT and AT electrodes.

- **Excitation Box** It provides the connection between the inner cryogenic and outer room temperature coaxial cables which supply the 5 excitation signals and the 3 switchable electrodes of the capture section. The excitation signals are generated by commercial frequency generators (*Keysight 33612A*).

- **HV Box** Here, the three HV blocking voltages for the capture section are introduced. During the first commissioning experiments the HV Box also provided the supply voltages needed for the operation of the trap tower EBIS, see chapter 6.1.

- **Signal Output Box** It accommodates all five detector output signal lines including the two charge sensitive detector outputs. The axial signals are mixed down to a frequency range of $0-20$kHz with a built in single sideband down converter *AF-DC-c* from Stahl electronics [134, 135, 136]. The respective input signal (AT or PT) applied to the *AF-DC-c* is selected with a computer-controlled multiplexer switch. The lower frequency allows for high-resolution FFT analysis via a *SR1 audio analyzer* from *SRS*. The FFT analyzer as well as all frequency generators are locked to the 10 MHz reference of a rubidium frequency standard *SRS FS725*.

5.2.2 Voltage Sources

For the DC-biasing of the trap electrodes and cryogenic electronics ALPHATRAP is equipped with four different types of voltage sources.

The ring and correction electrodes of the PT are individually supplied with up to -100 V from five ultra-stable channels of a StaReP[32] voltage source [137] built in house. The voltage resolution of each channel is defined by two 16bit DACs [33], one

---

[32] **Sta**ble **Re**ference for **P**enning-trap experiments

[33] digital-to-analog converter

for the coarse and one for the fine voltage setting. The nominal relative voltage stability is on the order of 10^{-8} for a typical time scale of 10 minutes.

The AT ring and correction electrodes are connected to three 25-bit precision channels of a UM1-14 (Stahl Electronics) voltage source which shows relative fluctuation on a 10^{-7} level. Additionally, the UM1-14 includes ten 16-bit fast mode channels that are used for the AT endcaps and for controlling the solid state excitation line switches. The remaining transport electrodes as well as the cryogenic amplifiers are supplied with two internally developed bipolar LoCepps[34] sources which are described in [138].

The high positive blocking voltages that are needed in the capture section during the injection of ions are delivered by a bipolar HV 200-8 supply by Stahl Electronics.

---

[34] **Lo**w **C**urrent **e**nabled **p**recision **p**ower **s**upply

6 Commissioning Experiments: Ion Preparation, Detection and Manipulation

In this chapter the very first commisioning runs of the ALPHATRAP experiment are described. Since the coupling section of the ALPHATRAP beamline to the large HD-EBIT is still under construction the ions were produced in two different ways. At first by a provisionally installed miniature electron beam ion source (EBIS) as explained below. Later, the implementation of the cryo-valve drive allowed for the first successful injection of argon ions which were externally produced with the small HC-EBIT. The commissioning phase was crowned by the first direct observation of spin flips in our experiment. Parts of this chapter can be also found in [65].

6.1 Trap Loading

6.1.1 Trap Tower EBIS

After finalization of the largest part of the experimental setup the very first tests of the ALPHATRAP trap tower and detection electronics began. These were performed with carbon ions generated inside the trap chamber by a miniature EBIS. At that time the microwave and laser inlet system was not yet implemented, so the EBIS was temporarily installed at the end of the trap tower instead of the microwave horn antenna as shown in figure 6.1. A similar trap tower EBIS is also successfully used by the Mainz experiment [104].
The operating principle resembles an EBIT described in chapter 4.2.1. An electron beam is produced by field electron emission from a pointed tungsten electrode (field emission point or FEP). To this end a potential difference (extraction voltage) between the negatively biased FEP and the acceleration electrode is applied. Since the EBIS is positioned in close proximity to the Penning-trap it is likewise immersed in the strong axial magnetic trapping field which guides the electrons along the field lines. After emission and acceleration the electron beam passes through a central 0.8 diameter hole within the target plate which in our case is manufactured from solid carbon. The beam continues its way through the entire trap tower to the capture section where it is reflected by predefined high-voltage reflection electrodes. Here the C4 and C5 electrodes[1] were combined to increase the field penetration to about

---

[1] Since C1-C3 are fast switchable electrodes they are connected via coaxial lines which are specified to a maximum of 600V. Furthermore the use of C6 as a HV reflector (>400V) should be avoided

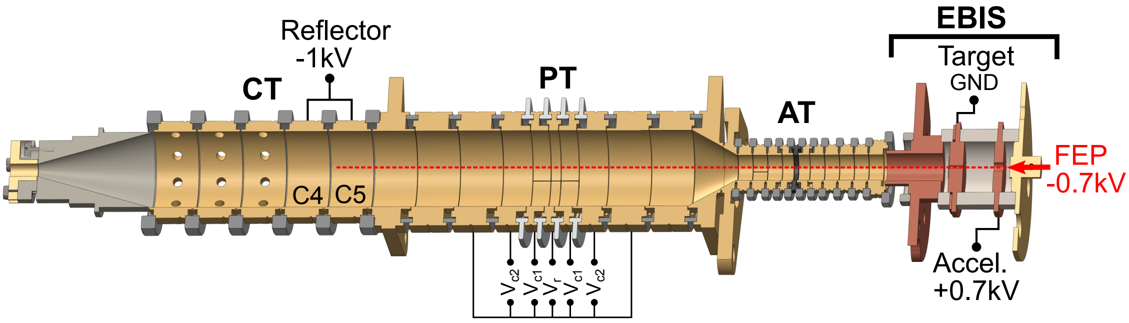

Figure 6.1: During the first commissioning runs ions were generated by an EBIS (see text) which was mounted in place of the microwave guide. Typically applied voltages during ion production are shown. The FEP is represented by the red arrow. The beam (red dashed line) is reflected by the combined C4 and C5 electrodes of the capture section. The target is a carbon plate with a central 0.8mm hole. The ions are caught in the AT or PT by applying the corresponding trapping voltages.

90 percent. The beam is reflected back and forth between the reflection electrodes and the FEP[2], which is still emitting and increasing the beam current density. Due to space charge effects the electron beam will eventually widen until it hits and evaporates atoms from the target surface. Similar to an EBIT, the atoms are then ionized and bred to higher charge states by consecutive electron impact within the electron beam. The ions can be collected/produced either in the AT or the PT by applying the respective trapping voltages. At ALPHATRAP the maximum electron beam energy is limited by the breakdown voltage of the cryogenic feedthroughs in the trap chamber. The feedthrough breakdown voltage was experimentally determined to be on the order of 1.5 kV at 10^{-6} mbar at room temperature[3]. During operation the risk of a breakdown is reduced by distributing the effective extraction voltage to the FEP and the acceleration electrode. Ion loading was carried out with typically applied voltages of $V_{\mathrm{FEP}} \approx -0.7\,\mathrm{kV}$ and $V_{\mathrm{Acc}} \approx 0.7\,\mathrm{kV}$, i.e. an extraction voltage (electron beam energy) of $V_{ext} = V_{Acc} - V_{FEP} \approx 1.4\,\mathrm{kV}$ and breeding times of about 15 s. The electron beam current impinging on the target surface was measure to be on the order of ∼20 nA. With these settings the production of carbon ions up to naked carbon nuclei $^{12}\mathrm{C}^{6+}$, having an ionization energy[4] of ∼490 eV, has been achieved. During and after loading the formation of a hot ion cloud within the chosen trap can be observed as an increase in the overall detector noise resonance.

---

since the gap size to the adjacent transport electrode is only about half of the distance between the other CT electrodes.

[2] The beam is trapped due to loss mechanisms as for example collision processes or synchrotron radiation.

[3] It is expected that the breakdown voltage should improve at experimental temperatures of ∼4K due to the reduction of leakage currents and cryogenic pumping.

[4] The electron beam energy should be ∼2.5 times higher than the ionization energy of the desired charge state [104].

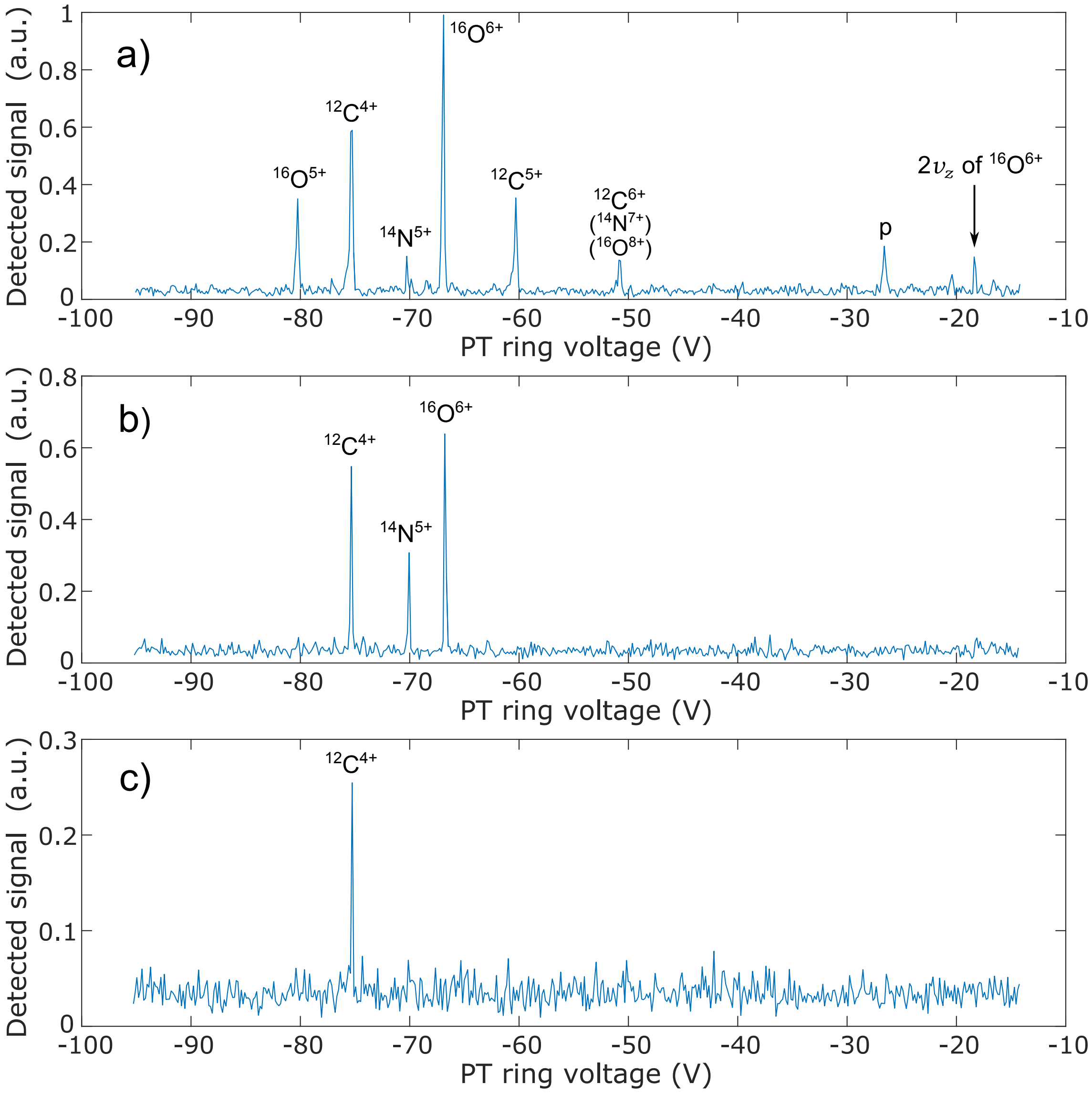

Figure 6.2: a) shows a PT mass spectrum after in-trap loading with $V_{ext} \approx 1.4\,\mathrm{kV}$ applied to the EBIS using a carbon target. Charge states up to naked carbon as well as ionized components of residual air-ice can be identified. Bracketed species are less likely produced due to the higher ionization energies. The most outer peak on the right side is likely to be a harmonic of the strong $^{16}O^{6+}$ signal. Spectra b) and c) were taken after sweeping the trap content over a strong dipolar excitation. This way ions can be successively ejected from the trap albeit not selectively (see text).

6.1.2 Mass Spectra

After producing and storing an ion cloud in one of the traps the ion composition of the cloud can be analyzed by recording a mass spectrum within the trap. To this end the dependence of the axial frequency (equation 3.13) on the charge-to-mass ratio q/m and the trapping voltage (ring voltage) can be exploited. By doing a continuous down (or up) sweep of the ring voltage, different ion species with increasing (decreasing) q/m will successively be brought into resonance with the detector circuit. Here they are detected as peak signals provided that the ion axial mode energy is hot, which is usually the case right after production. Figure 6.2 a) shows a typical mass spectrum of an ion cloud shortly after production with the in trap EBIS using a carbon target. The spectrum was recorded with a Rigol DSA815 spectrum analyzer in zero span mode: The integrated power at the resonator resonance frequency was measured and plotted against the ring voltage during a down-sweep. While sweeping, the ions are resistively cooled by the PT resonator with cooling time constants $<$1s (depending on their mass and charge) . In order to compensate for the bolometric cooling and to allow for multiple scans a constant dipolar excitation at a frequency above the resonator frequency was applied, such that the ions are swept over the excitation before they arrive on the resonator. As expected from the electron beam energy, charge states up to naked carbon can be generated. Other observable ions are most likely due to contaminations of the target with air-ice. In figure 6.2 b) and c) the excitation amplitude was continuously increased such that ions species are successively lost from the binding trap potential and only a single species $^{12}\mathrm{C}^{4+}$ remains. Although this is a first illustrative example of trap cleaning, in general this process is not applicable to generate a specific single ion of interest. More selective cleaning techniques will be discussed.

6.1.3 External Injection

In the course of this thesis the first successful injection and capturing of externally produced HCI in the ALPHATRAP trap setup has been achieved. The whole injection process consists of the following steps:

Beam Production and Alignment

The first injection was performed with Ar ions created with the HC-EBIT at an electron beam energy of 3 keV allowing for charge states up to Ar^{16+}. For a detailed discussion and optimization process of the HC-EBIT and the beamline the reader is referred to [107, 108]. The ions were ejected in bunches at a rate of $\sim$ 5 Hz (i.e. a breeding time of 200 ms) by pulsing the central EBIT drifttube electrode (DT3) from $U_t \approx 1750\,\mathrm{V}$ trapping potential to an extraction voltage of $V_{ext} \approx 2010\,\mathrm{V}$ for an extraction time[5] of $t_{ext} \approx 4\,\mu\mathrm{s}$. After extracting the beam from the HC-EBIT the desired charge state is selected via the Wien filter voltage and the

---

[5] After 4 µs the ions are typically completely depleted from the EBIT trap region [107].

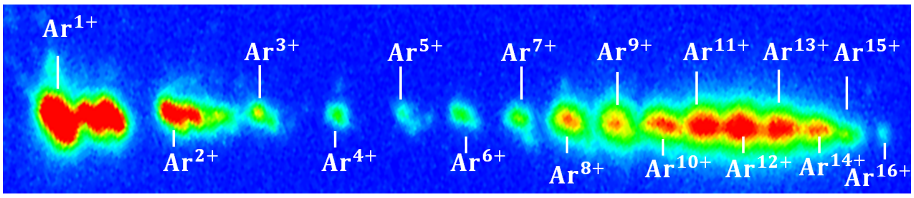

Figure 6.3: Charge states up to $^{40}\mathrm{Ar}^{16+}$ are visible on the MCP detector behind the Wien filter which is here operated in low dispersion mode. Modified from [111].

subsequently installed MCP detector. A convenient way to find out the charge state is by identifying the $^{40}\mathrm{Ar}^{10+}$ peak with the $^{16}\mathrm{O}^{4+}$ peak in the rest-gas spectrum when closing the Ar gas supply valve. Using the electrostatic lenses and quadrupole benders the purified high energy beam is then guided through the horizontal into the vertical beamline and focused on the last MCP detector. Subsequently the segmented electrostatic lenses within the vertical beamline branch are manually scanned and optimized until a strong signal of high energy ions can be detected on the oscilloscope connected to the cryogenic charge sensitive detectors within the trap chamber.

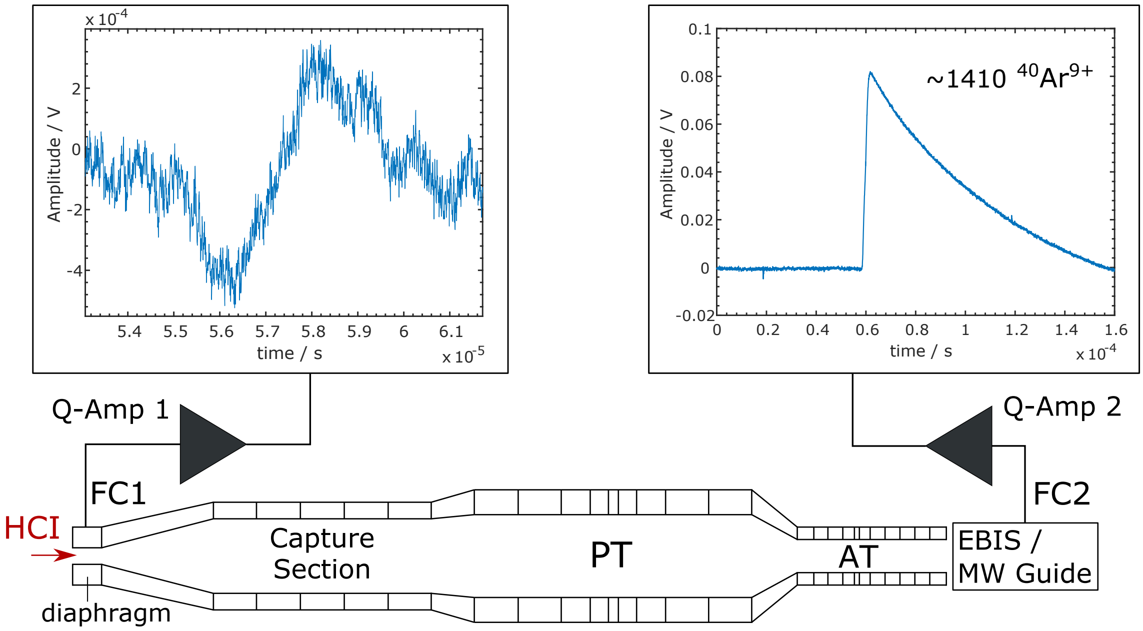

Figure 6.4: Typical averaged signals of slow (100 eV) Ar^{9+} bunches visible on the two charge sensitive detectors. The bunches arrive at FC2 about 0.6 ms after the ejection from the Mini-EBIT. The signal rise time corresponds to an ejection pulse time (temporal bunch length) of ∼3 µs. The discharge time constant is slightly longer than the value given in section 5.1.8. This is because an additional high pass filter was used to suppress the mains noise.

Beam Deceleration

Deceleration of the ion bunches within the beamline (see chapter 4.3) is achieved by letting them run up a positive potential V_d applied to the long pulsed drifttube (DT) electrode. It is important that the beam enters straight and central into the DT, otherwise the beam position after the DT will sensitively depend on V_d. The alignment can be optimized by step wise increasing the DT voltage (static, i.e. without switching) while observing if the beam position on the last MCP is changing. After this adjustment, the actual deceleration process begins. At an extraction/beam energy of $E_{ext} \approx 2\,\mathrm{keV} \cdot q$ the initial length of a $^{40}\mathrm{Ar}^{9+}$ bunch[6] is $l_b = t_{ext}\sqrt{2E_{ext}/m_{ion}} \approx 1.18\,\mathrm{m}$. Thus, to fit/compress the beam into the $l_d \approx 0.5\,\mathrm{m}$ long drifttube a voltage of at least

$$V_d \geq V_{ext} - \frac{1}{2q} m_{ion} \left(\frac{l_b}{t_{ext}}\right)^2 \approx 1640\,\mathrm{V} \tag{6.1}$$

has to be applied. As soon as the ion bunch is within the potential free region, the DT is rapidly discharged within $< 100\,\mathrm{ns}$ via a HV switch (Behlke GHTS100A). To increase the yield of decelerated HCI the proper timing of the DT discharge trigger is important. It is generated and synchronized to the EBIT extraction trigger pulse by a delay timer card. The timing for a certain V_d is manually determined by maximizing the time delay and amplitude of the cryogenic charge detector signals. It was found that deceleration down to injection energies as low as $45\,\mathrm{eV}q$ works best when V_d is increased in small steps, whereby each time the signal amplitude on the cryogenic charge detector has to be re-optimized by fine-tuning the optical elements of the beamline. Figure 6.4 shows the post-amplified averaged signal of the two charge sensitive detectors during the injection of Ar^{9+} bunches. The dispersive signal picked up by FC1 indicates that the magnetic field of the magnet allows for a sufficient radial compression of the ion bunch in order to pass the 3 mm hole of the diaphragm without significant ion loss. The signal on the second detector shows an Ar^{9+} bunch impinging on the target of the in-trap EBIS, which was used as the second FC at that time. Considering a post amplification of 54 dB [7] and neglecting conduction losses the signal amplitude corresponds to ≥ 1410 Ar^{9+} ions. To estimate the transfer efficiency from the room temperature beamline into the trap tower a separate measurement was performed using $^{8}\mathrm{O}^{5+}$ ions[8] decelerated to $100\,\mathrm{eV} \cdot q$. Here the number of oxygen ions impinging on the Faraday cup behind the Wien filter was determined to be ~14500 while the lower cryogenic charge detector showed 410 decelerated ions, corresponding to an overall transfer efficiency of $\sim 3\%$. The second (lower) cryogenic charge sensitive detector offers a convenient way to determine the

---

[6] During the first injection tries $^{40}\mathrm{Ar}^{9+}$ was used due to the good signal quality/yield which faciliated the adjustment.

[7] Here a commercial amplifier with 40dB gain was used in addition to the lower charge amp with 14dB gain.

[8] Oxygen was used because the dispersion of the Wien filter was not sufficient to get only a single charge state of Argon ions onto the FC.

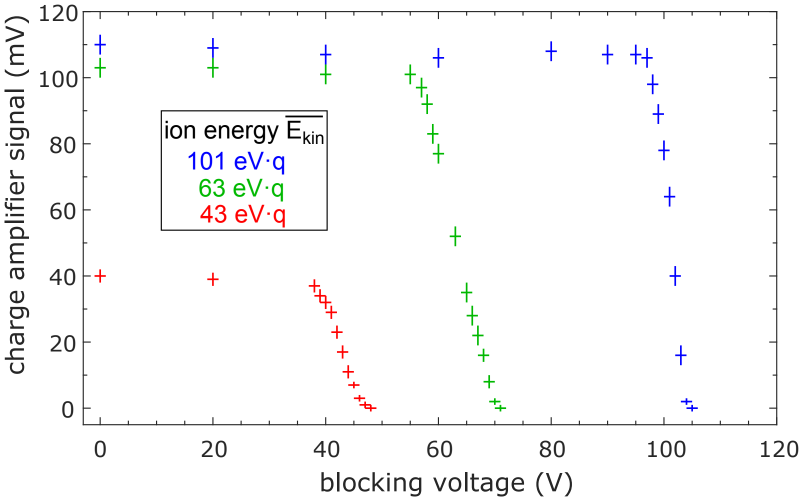

Figure 6.5: The ion beam energy can be measured by stepwise increasing the blocking voltage in the capture section while observing the signal on the lower charge sensitive detector. Here this was repeated for three different beam energies after deceleration.

ion beam energy and dispersion. To this end a blocking voltage which is applied to C4-C6[9] is stepwise increased until the signal on the second charge sensitive detector disappears. In figure 6.5 such a measurement is shown for three different ion beam energies after deceleration with the pulsed drifttube.

Ion Capturing

For the final capturing of decelerated ions a typical potential configuration as shown in figure 6.6 is applied to the capture electrodes. The capture efficiency can be optimized by adjusting the capture potential according to the energy of the ion bunch which has been previously measured (figure 6.5). In a first step the ion bunch is slowed down and spatially compressed. When the ion bunch arrives at its motional reversal point it is caught in a potential well by applying a fast switching pulse to the diode pair filtered electrodes C1-C3. Knowing the kinetic energy of the ion bunch and taking into account the rise time ($\sim 1\,\mu s$) of the diode pair filter, the proper switching timing can be calculated e.g. from the arrival time on the first FC and the applied potential configuration in the capture section. When switching at the reversal point, the remaining axial energy (and with it the needed potential depth) is mainly determined by the energy spread of the ion bunch. For HCI injected from the HC-EBIT the axial energy spread is typically on the order of 5 eV/q to 10 eV/q as can be seen in figure 6.5.

---

[9] This configuration has almost 100 percent field penetration.

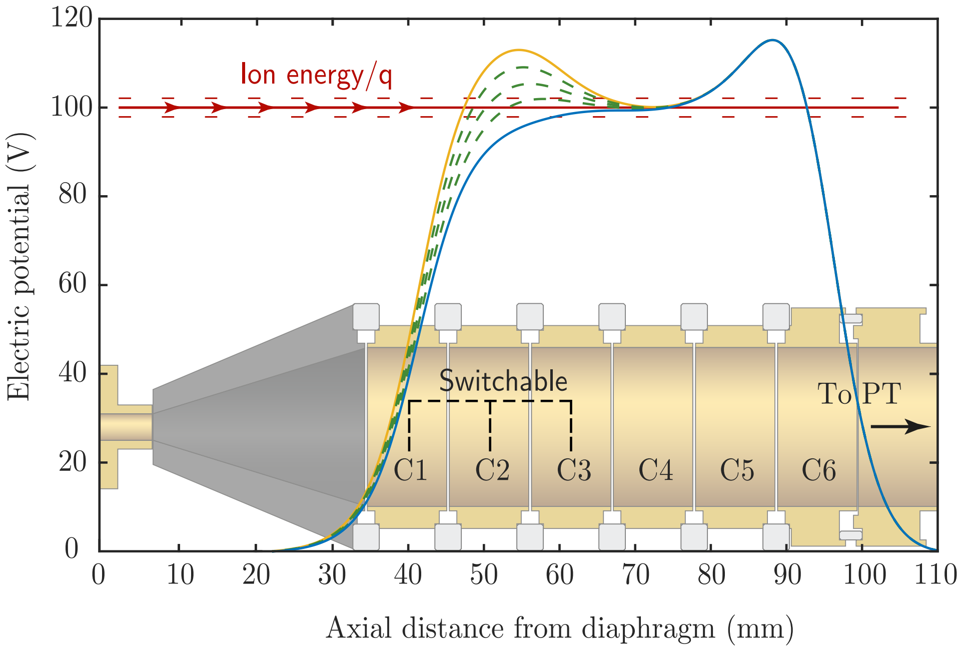

Figure 6.6: Illustration of a typical potential applied to the capture electrodes during the injection of ions with an average energy of 100 eV · q. The incoming ion bunch is slowed down and compressed by the blue potential curve. When the bunch arrives at its motional reversal point it is caught in a potential well by switching C1-C3 to a high potential (yellow curve).

6.1.4 Ion Life Time

A long ion life time is an essential requirement for a successful g-factor measurement. The dominant[10] loss mechanism for a single particle stored in a Penning-trap are collisions with other restgas atoms or molecules contained within the trap chamber volume. These can either lead to charge exchange or complete ion loss due to momentum transfer, where at typical operation conditions, the metastable magnetron motion is particularly vulnerable. To date, during the complete operation time of the ALPHATRAP experiment, none of these processes could definitely be observed while the so far longest achieved storage times of up to four months for a single $^{40}\mathrm{Ar}^{13+}$ were limited by either intentional change of the ion species or accidental ion loss due to faulty operation[11]. Since no charge exchange process has been observed during the time of 4 months the trap chamber pressure can be conservatively estimated provided that charge exchange predominantly takes place by Langevin-scattering

---

[10] Naturally, apart from technical or human error.

[11] "In the heat of the battle."

with hydrogen molecules as discussed in [139]

$$p_{H_2} = n_{H_2} k_B T = \frac{k_B T}{k_L(\mathrm{Ar}^{13+}, \mathrm{H}_2) \cdot \mathrm{Ar}^{13+}} \approx 3 \cdot 10^{-18} \mathrm{mbar}. \tag{6.2}$$

Here, the Langevin rate coefficient is $k_L(\mathrm{Ar}^{13+}, \mathrm{H}_2) \approx 1.957{\cdot}10^{-14}\mathrm{m}^3\mathrm{s}^{-1}$ [139] while for the lifetime $\tau_{\mathrm{Ar}^{13+}} \approx 4$ months was used, assuming that the particle is lost with a probability of $1 - 1/e \approx 63\%$ within this time. It is remarkable that this excellent vacuum was not influenced by the connection to the beamline which demonstrates the successful operation of the online setup and the cryogenic valve. Based on this pressure value the calculation can be inverted to estimate the possible storage time of hydrogen-like lead $^{208}\mathrm{Pb}^{81+}$ ions. With $k_L(\mathrm{Pb}^{81+}, \mathrm{H}_2) \approx 1.194 \cdot 10^{-13}\mathrm{m}^3\mathrm{s}^{-1}$ one gets $\tau_{\mathrm{Pb}^{81+}} \approx 0.67$ months.

6.2 Single Ion Preparation and Detection

6.2.1 Cleaning Methods

After successful ion production/injection the stored ion cloud has to be "cleaned" from unwanted species[12] and charge states until only a single ion of interest is left in the trap. This is achieved by a number of well-established techniques of which the following are commonly used at ALPHATRAP.

- **Axial Cleaning** A simple but very effective method is to temporarily lower ("dip") the potential depth (trapping voltage) close to 0V so that ions with excessive axial energy leave the trap potential. Prior to dipping the ions with the needed q/m ratio are tuned and thermalized with the axial detector circuit down to $k_B{*}T \approx 0.4\,\mathrm{meV}$ so it is less likely to lose them. After dipping a strong broadband axial excitation (sweep) can be applied around the resonator/ion resonance frequency (leaving out the magnetron as well as harmonics of the ion frequency). This process can be repeated until only a single particle remains in the trap.

- **Magnetron Cleaning** By applying a radial broadband white noise excitation near the magnetron frequency the magnetron radius increases until unwanted ions impinge on the inner electrode surface. Simultaneously, magnetron sideband cooling is used in order to counteract the excitation of ions with desired q/m. Compared to axial excitation/cleaning, magnetron cleaning has the advantage that already excited hot ions do not pass though the purposely cooled ion cloud in the trap center which can lead to energy transfer and loss of the wanted ions species.

---

[12] Especially after production with the in-trap EBIS the cloud is composed of different species and charge states.

- **Cyclotron Cleaning** Direct cyclotron cleaning, i.e. by widening the reduced cyclotron radius, is practically not applicable since it requires high excitation energies on the order of $\frac{1}{2}\omega_+^2 r_{PT}^2 \approx 170\,\mathrm{eV/u}$. Nevertheless, heating the cyclotron mode with a strong burst excitation allows for an indirect cleaning as some of the cyclotron energy is transmitted via collisions to the other eigenmodes which are inherently less stable. Since this process only works as long as there is more than one particle in the trap, it is particularly suitable for producing a single particle from a preselected ion cloud with similar q/m.

6.2.2 Bolometric Detection

Axial Detection After successful cleaning and sideband cooling a cold ion of the desired species which is tuned to the axial detector circuit appears as a dip signal in the detector noise resonance. The presence of other ions of the same species can be excluded by the characteristic dip width[13], which according to equation (3.55) scales linearly[14] with the ion number. In figure 6.7a) this is demonstrated by comparing the dip width of a single and two $^{12}\mathrm{C}^{5+}$.

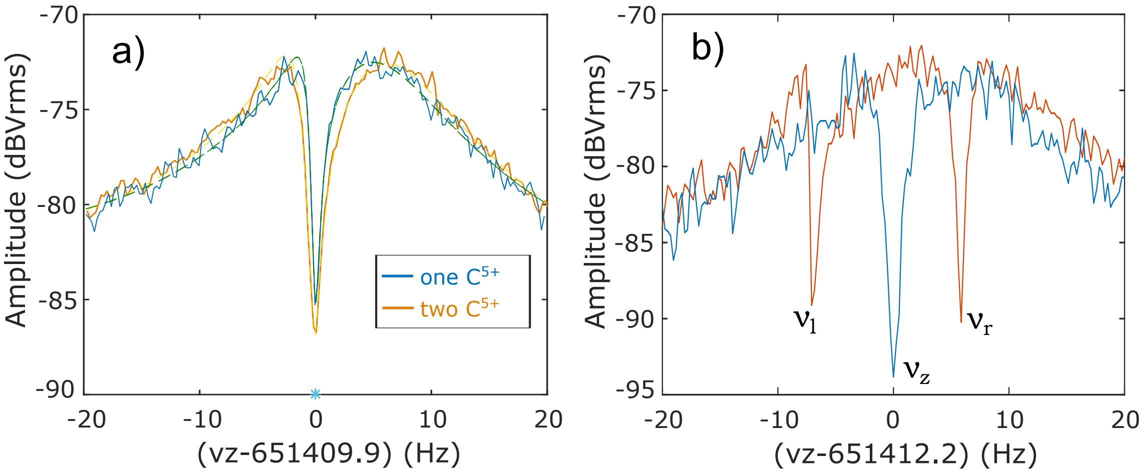

Figure 6.7: a) Overlapped dip signals of a single $^{12}\mathrm{C}^{5+}$ and two ions of the same species showing the doubled dip width. b) Overlapped single-dip (before sideband coupling) and double-dip signal (during sideband coupling) on the PT axial detector. The radial frequencies (here the reduced cyclotron frequency) can be determined from ν_l, ν_r, ν_z and the applied coupling frequency. The smaller depth of the single dip in figure a) is due to an unoptimized tuning ratio used at that time.

---

[13] Even if the dip width corresponds to a single ion this does not automatically exclude the presence of ions with different q/m. However, a deteriorated frequency stability ("smeared out" dip signal) can typically give an indication of this.

[14] for small ion numbers

ν_z	651 411.20(10) Hz
ν_+	25 738 548.39(22) Hz
ν_-	8243.84(22) Hz
ν_c	25 746 791.60(22) Hz
B	4.023 033 683(35) T

Table 6.1: Results of an exemplary eigenfrequency measurement with a $^{12}\mathrm{C}^{5+}$ ion in the PT.

Radial Detection As discussed in chapter 3.2.5 the radial frequencies of the reduced cyclotron or magnetron mode can be determined from equations (3.65) and (3.66) by measuring the double-dip frequencies[15] appearing when a coupling drive close to the corresponding sideband frequencies $\nu_+ - \nu_z$ or $\nu_- + \nu_z$ is applied. To be able to see the double-dip on the $\sim$ 16 Hz wide PT resonator the coupling drive frequency must match the respective sideband within a few single Hertz. This was challenging especially during the very first commissioning when the Q-switch was not yet implemented and the magnetic field was only roughly known. It had to be estimated from the measured B-field value after magnet charging and the initially observed relative field drift of $\sim 1.4 \cdot 10^{-6}$ per day. Having found the correct coupling frequencies the full set of eigenfrequencies can be determined. Thereupon, the invariance theorem yields the free cyclotron frequency and the magnetic field. The result of such a single measurement (performed in the PT with a $^{12}\mathrm{C}^{5+}$ ion) is exemplary summarized in table 6.1.

Excitation Switch Linearity Since the Rabi frequency and thus the splitting of the double-dip signal scales linearly[16] with the signal amplitude (perceived by the ion) sideband detection can be exploited in order to check the transmission linearity of the excitation switches (chapter 5.1.7) which simplifies the excitation of an ion to a predefined radius[17]. The linearity was confirmed by a measurement of the double-dip splitting depending on the amplitude of the coupling drive (see figure 6.8).

6.3 Trapping Field Characterization

As discussed in chapter 3.2.3, deviation from the ideal trapping field configuration can lead to unwanted systematic shifts of the particle eigenfrequencies. For com-

---

[15] The coupling drive frequency and axial frequency must also be known/measured.

[16] Actually this is only the case for negligible detuning δ of the coupling drive from the real sideband frequency.

[17] Apart from the amplitude the radius is also proportional to the excitation time, and thus can be alternatively influenced by the cycle number of the excitation burst. However, this comes at the cost of a varying excitation bandwidth.

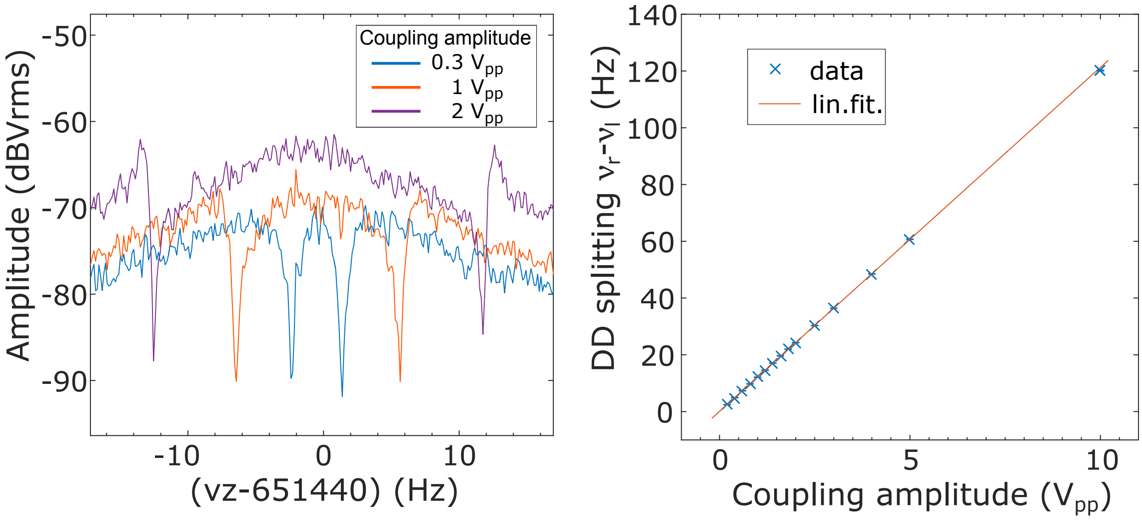

Figure 6.8: Test of the excitation switch linearity via the double-dip (DD) splitting during cyclotron sideband coupling in the PT. Up to $5\,\mathrm{V}_{pp}$ (peak to peak), the splitting is sufficiently linear within 0.1%. Even at $10\,\mathrm{V}_{pp}$, which is the maximum output amplitude of our frequency generators, the deviation amounts only ∼1%.

pleteness the basic optimization procedure of the electrostatic field harmonicity as well as measurements of the magnetic field properties and a characterization of the stability will be briefly introduced in the following. Further informations on the underlying measurement techniques can be found in [83, 104] while the detailed characterization of the ALPHATRAP trap tower is discussed in [105].

6.3.1 Tuning Ratio Optimization

In a real Penning-trap electrostatic field unharmonicities (e.g. due to manufacturing tolerances) can be minimized by optimization of the tuning ratio. To this end one can exploit the (unharmonicity induced) dependency of the axial frequency on the particle oscillation amplitude/radius. This shift, to first order given by equation (6.3), also shows a linear behaviour with the applied tuning ratio (see also chapter 3.2.3)

$$\frac{\Delta\omega_z}{\omega_z} = \frac{C_4}{C_2}\frac{3}{4d^2}\left({a_z}^2 - 2{a_+}^2 - 2{a_-}^2\right) \quad \text{with} \quad C_4 = {C_4}^0 + D_4 \cdot TR. \tag{6.3}$$

Thus, by stepwise changing the TR and measuring the axial frequency shift after exciting[18] the ion to a defined magnetron[19]radius, the optimal tuning ratio can be

---

[18] Between single shift measurements for different TR, magnetron cooling is applied in order to restore the original axial frequency.

[19] When using the comparably slow magnetron mode the additional shift due to the magnetic bottle term as well as the relativistic shift are negligible.

derived from the zero crossing of the linear fit to the measured frequency shift data. It must be noted that the 7 electrode PT, having two sets of correction electrodes, necessitates a "dynamic" optimization process in which the ideal (calculated) tuning ratios ($TR_1 = 0.9636$ and $TR_2 = 0.8156$ [105]) are varied proportionally, i.e. by a combined tuning ratio TR^{comb}[20] such that

$$C_4 = {C_4}^0 + TR^{comb} \cdot \underbrace{(D_{41} \cdot TR_1 + D_{42} \cdot TR_2)}_{D_4^{comb}} \overset{!}{=} 0. \tag{6.4}$$

In the ideal case this would be fulfilled for $TR^{comb}_{ideal} = 1$ while the experimental optimization of the PT yields a combined tuning ratio[21], of $TR^{comb}_{opt} = 1.0004872(50)$ demonstrating the successful realization of the theoretical prediction. For the detailed optimization process with estimations of residual higher order field contributions the reader is referred to [105].

6.3.2 Magnetic Field Shape

During commissioning first measurements of the dominant magnetic field inhomogeneities up to the second order[22] have been performed in the PT and AT. This can be achieved by two common techniques.

On the one hand the magnetic field shape can be directly recorded. By applying an asymmetric trapping potential (e.g. to the correction electrode) it is possible to purposely vary the axial ion position in a defined way around its original position. At each new position the magnetic field is derived by measuring the free cyclotron frequency. The field coefficients can then be directly extracted from the corresponding polynomial fit. In the PT this method was used to determine the B_1 contribution via a linear fit to the measured magnetic field data as shown on the left side in figure 6.9. The given B_2 value was derived via a different technique described below. Compared to the old Mainz g-factor experiment at ALPHATRAP the B_1 and B_2 contributions in the PT are reduced by a factor of ~ 5 and ~ 15, respectively [83, 104]. Additionally, taking into account that the corresponding systematic shifts cancel to a large extent[23] in the final determination of the g-factor via the frequency ratio $\Gamma = \frac{\nu_L}{\nu_c}$ (see equation (3.3)) they do not impose a limitation for the currently reachable relative precision level of 10^{-9} [105].

For the explicit measurement of the B_2 term in both traps one can directly exploit equation (3.32). To this end the reduced cyclotron mode is excited to different (defined[24]) radii and each time the corresponding axial shift is measured. Conse-

---

[20] in order to preserve the combined orthogonality criterion introduced in chapter 3.2.3

[21] Actually the TR has to be optimized after every loading procedure since this typically leads to a modification of patch potentials on the electrode surface (especially when the in trap EBIS was used).

[22] Measurements are typically performed with cold ions such that higher orders can be neglected.

[23] Actually, the B_1 contribution even cancels completely.

[24] This necessitates a dedicated energy/radius calibration which relates the applied excitation pulse strength to the cyclotron radius [83, 105].

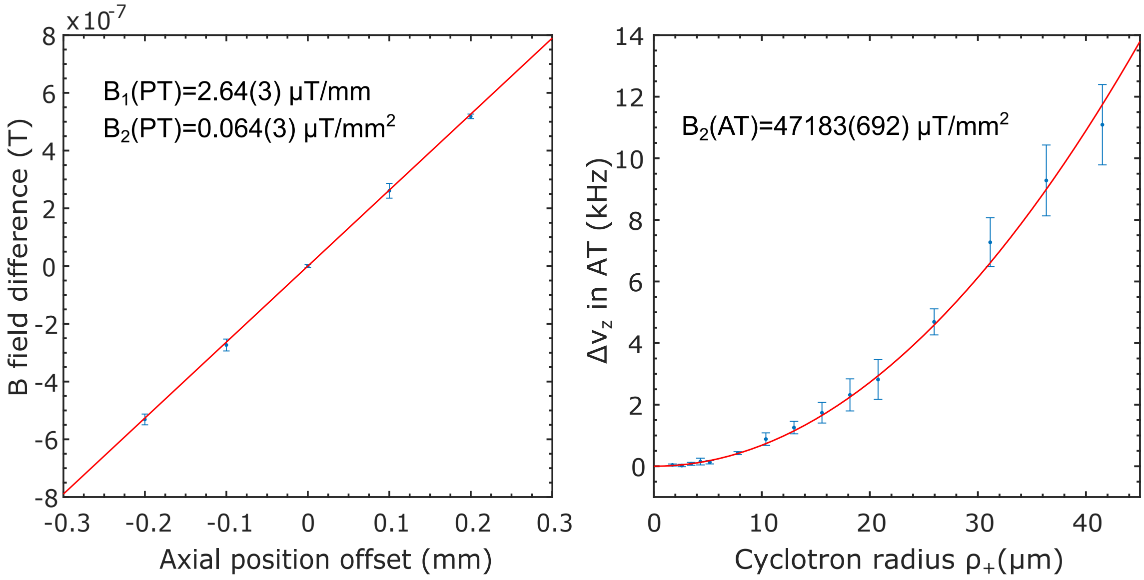

Figure 6.9: (left side) In the PT the axial magnetic field shape was scanned by purposely shifting the ion position and measuring the free cyclotron frequency. Compared to the old Mainz g-factor experiment at ALPHATRAP the homogeneity in the PT has improved (see text). (right side) An alternative method to determine the magnetic bottle term is by measuring the B_2 induced shift when an ion is excited to different cyclotron radii as here shown for the AT. In both plots the data points and error bars are mean values and standard deviations of 5 single measurements.

quently, the magnetic bottle term is extracted from equation 3.32 via a parabolic fit to the frequency shift data. The aforementioned method was used to determine the strong magnetic bottle term in the PT and AT[25]. The measurement of the magnetic bottle term in the AT is shown on the right side of figure 6.9. Apart from getting an estimation on the spin flip induced shift, the B_2 value is also needed for other purposes as e.g. the measurement of the ion/detector temperature as presented in section 6.5.

6.3.3 Trapping Field Stability

Stability Measurements in the PT Ideally, the determination of the g-factor via the Larmor to cyclotron frequency ratio $\Gamma = \nu_L/\nu_c$ (see equation (3.3)) is independent of the magnetic field. However, this is only true if ν_L and ν_c are measured

---

[25] In principle the magnetic field shape can also be determined by position dependent cyclotron frequency measurements. However, in the AT this is complicated by the fact that the double-dip method can not be applied in the strong magnetic bottle. Instead, a spectroscopic method is used in which the correct cyclotron resonance frequency is found by maximizing the observed B_2 related axial frequency shift in dependence on the applied cyclotron excitation frequency [80, 104].

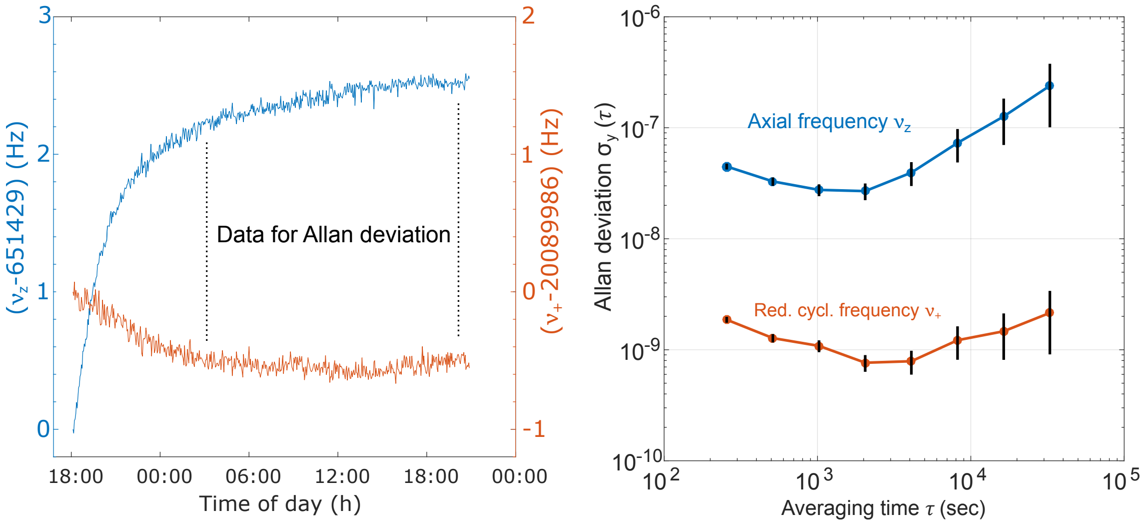

Figure 6.10: Stability measurement and Allan deviation of the axial and reduced cyclotron frequency in the PT using the dip and double-dip detection technique. The frequencies were measured alternately with an averaging time of ~80 s per measurement. The initial drift is caused by the thermalization of the not yet stabilized voltage supply and magnet after closing the laboratory door.

simultaneously. In reality the spectroscopic determination of ν_L and the indirect measurement of ν_c (via the invariance theorem) happen within a finite measurement time which generally leads to a broadening of the Γ resonance due to trapping field instabilities. In this context the measurement technique plays an important role. First characterization measurements of the electric and magnetic trapping field stability in the PT were performed with bolometric measurements of the eigenfrequencies. Figure 6.10 shows a stability measurement in which the axial and reduced cyclotron frequency[26] of an $^{40}\mathrm{Ar}^{13+}$ ion were monitored over 24 hours via dip and sideband detection. At the current stage neither the trap voltage sources nor the magnet are temperature stabilized. For demonstration purposes the thermalization related drift after closing the laboratory door is also plotted but omitted in the calculation of the Allan deviation. The axial relative frequency stability is $\sim 4 \cdot 10^{-8}$ on a timescale of 16 minutes corresponding to a voltage stability of $\sim 8 \cdot 10^{-8}$ of the StaReP supply. A further deterioration for shorter measurement times is visible. However, since the frequency uncertainty from a lineshape fit to the incoherent dip signal scales with the inverse square root of the averaging time, it is currently not possible to make a more precise statement about the actually achievable short-term stability. Nevertheless, at the current level of precision achievable with the dip technique,

---

[26] Here the measurement of the magnetron frequency ν_- has been omitted due to it's suppressed contribution (see equation (3.38)) to the final measurement uncertainty of the free cyclotron frequency. For the same reason ν_- is typically only periodically checked during a g-factor measurement [104].

the relative uncertainty contribution of the axial frequency to the free cyclotron frequency can be estimated $< 6 \cdot 10^{-11}$. As far as magnetic field stability is concerned, it has to be mentioned that the shown measurement was taken during the night and after improving the intrinsic shielding of the superconducting magnet by a factor of ∼6.7, which was achieved with an additional superconducting shielding coil wound around the trap chamber [19, 140]. With this, no significant fluctuations can be observed within the currently achievable precision which is mainly limited by the sideband detection method. This is because in a double-dip measurement ν_+ is determined from an offset to the typically less stable axial frequency (see chapter 3.2.5) which directly impairs the measured stability/uncertainty of ν_+. In this sense the measurement of ν_+ via sideband detection can only give a lower limit of the actual magnetic field stability and the currently achievable statistical uncertainty, which can be conservatively estimated by $\delta\nu_c/\nu_c \approx \delta\nu_+/\nu_+ \approx 2 \cdot 10^{-9}$ for a single measurement. This limitation can be avoided by direct measurements of the reduced cyclotron frequency with the phase sensitive PnA technique which will be implemented in the near future.

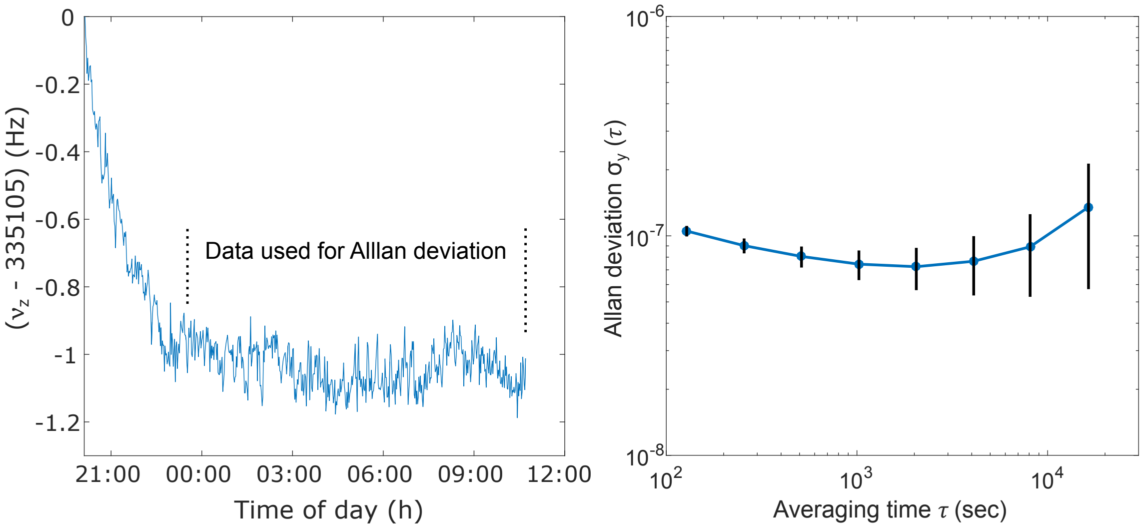

Figure 6.11: Stability measurement and Allan deviation of the axial frequency in the AT using the dip detection technique. The measurement time was 80s. The initial drift is caused by the thermalization of the not yet stabilized voltage supply after closing the laboratory door.

Stability Measurements in the AT In chapter 3.2.6 it was pointed out that the direct detection of a spin-flip in the magnetic bottle of the AT necessitates a highly stable axial frequency which mainly depends on the supply voltage stability as well as a good performance of the detection system with respect to the reduction of spurious noise. As in the PT the axial frequency stability in the AT was monitored via dip detection during a night measurement shown in figure 6.11. The Allan deviation is derived from the frequency data after thermalisation of the laboratory and the UM1-14 voltage supply. Within the precision achievable with the dip detection technique the measured relative frequency stability in the AT on the order of $\sim 1 \cdot 10^{-7}$ demonstrates the satisfactory performance of the detection system. The standard deviation of the absolute fluctuations between consecutive measurements corresponds to only 51 mHz. As will be shown in chapter 6.7 this good stability enabled the first direct detection of bound electron spin transitions at the ALPHATRAP experiment.

6.4 Ion Transport

During a g-factor measurement run the ion is transported hundreds of times between the PT and the AT. To rule out systematic errors in the detection of the spinflip in the AT, it is of great importance that the transport does not influence the spin state of the particle. Particle transport within the trap tower is realized by adiabatically[27] shifting the confining trap potential along the trap tower such that the ion is passed on from electrode to electrode. This is achieved in steps in which the negative transport voltage applied to the electrode holding the particle is raised (grounded) after the adjacent electrode voltage was lowered to the same transport potential. At ALPHATRAP a one directional transport between the AT and the PT takes $\sim 30\,\mathrm{s}$. The minimum transport voltage is $-10\,\mathrm{V}$ which is the lower limit of the UM1-14 voltage source supplying the AT as well as the neighboring transport electrodes. Furthermore the individually applied transport voltages must compensate for the different field penetrations which depends on the particular electrode geometries. Special care must be taken when leaving or arriving in the AT or PT. For example, before leaving the PT, the ring and correction voltages must be changed from the compensated (harmonic) measurement potential to the uncompensated transport potential which is only applied to the ring electrode while the correction electrodes are set to ground. Here the sequence in which the ring and correction voltages are set matters as is shown in figure 6.12. When changing from the (ion specific) measurement voltage ($V_r = V_m$) to a more shallow transport configuration ($|V_r| = |V_t| < |V_m|$) the correction voltages must be set from "outside to inside" i.e. the correction voltages must be grounded before the ring voltage is decreased. This order has to be inverted when the measurement configuration is restored after the transport. It was observed that if the wrong sequence is used, the potential will transit two times through highly anharmonic configuration with an elongated field-free region (right side of figure 6.12) which drastically increases the probability to lose the ion[28]. The influence of the transport was separately investigated by performing 100 transports between the traps and measuring the axial frequency dip in the strong magnetic bottle of the AT after each transport. Thus, a spinflip or change in the cyclotron energy would be directly reflected in the axial

---

[27] This means, that the applied voltages are varied much slower than the eigenmotion of the ion such that its classical action is conserved.

[28] This is mainly due to an increase of the magnetron radius.

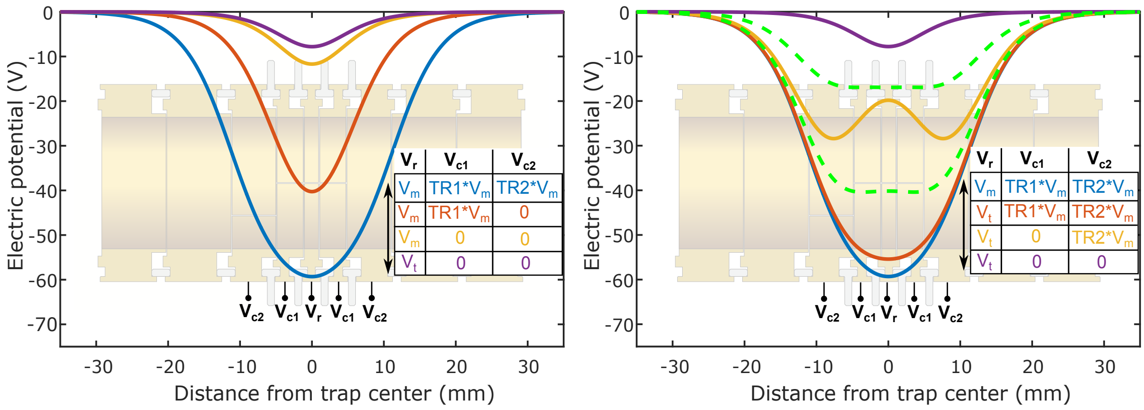

Figure 6.12: When changing between the compensated measurement configuration ($V_r = V_m$, $V_{c1} = TR1 * V_m$, $V_{c2} = TR2 * V_m$) and the transport configuration ($V_r = V_t$, $V_{c1} = 0$, $V_{c2} = 0$) the ring and correction voltages must be applied in the correct order as shown on the left side. Otherwise the potential will transit two times through anharmonic configurations with a central field-free region (dashed green line) which can lead to ion loss (see text).

frequency stability. The measurement was performed with a $^{40}\mathrm{Ar}^{13+}$ ion. It must be noted, that before the measurement the particle was prepared with a low cyclotron energy. As can be seen in figure 6.13 no significant increase in the axial frequency fluctuation can be observed. The stability differs only insignificantly from the pure AT stability without transport which demonstrates the successful implementation of the adiabatic transport.

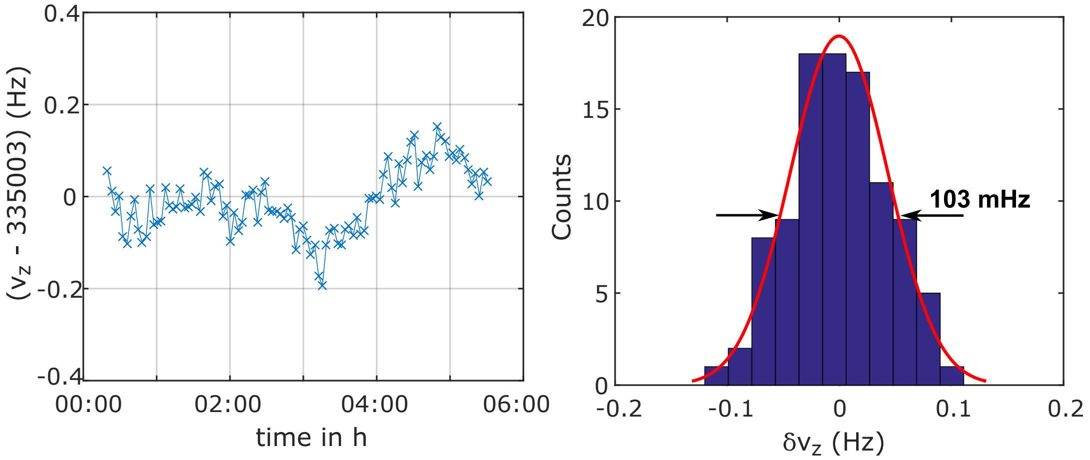

Figure 6.13: Measurement of the axial frequency in the strong magnetic bottle of the AT during 100 transport cycles between the PT and AT. Each cycle takes 3 minutes. The normally distributed frequency deviation between consecutive measurements shows a FWHM of 103 mHz, i.e. a standard deviation of $\sim 44\,\mathrm{mHz}$.

6.5 Particle Temperature Measurement

In order to reduce systematic frequency shifts, a small particle temperature is an essential requirement for a high-precision g-factor measurement. As discussed in chapter 3.2.5 resistive- and sideband cooling techniques allow to thermalise the corresponding ion mode temperatures with the axial detector circuit. When the ion is in thermal equilibrium with the detector circuit it is driven by the incoherent detector noise. It includes not only the resonator Johnson noise $u_J = \sqrt{4k_B T R_p}$ but also the electronic noise u_{el} of the cryogenic amplifier. Consequently the detector circuit, or rather its electron gas ensemble, can be assigned with an effective noise temperature T_{eff} which in general is higher[29] than the lattice temperature T_l of the experiment:

$$T_{eff} = \frac{u_{el}^2 + u_J^2}{4k_B R_P} = \left(\frac{u_{el}}{4k_B R_P}\right)^2 + T_l. \tag{6.5}$$

In this regard, ion temperature measurements are an effective way to verify the detector noise performance. As long as the ion and detector frequency are in (or close to) resonance, the ion energy is not constant but fluctuates on timescales of the cooling time constant τ. According to the ergodic hypothesis, consecutive measurements of the axial energy of the thermalised ion will reproduce a Boltzmann distribution at the effective detector (ion) temperature $T_{eff} = T_z = \frac{\langle E_z \rangle}{k_B}$ [83]. The thermal distribution of the axial mode can be accessed via sideband coupling to the reduced cyclotron mode. During sideband coupling the reduced cyclotron energy reflects the thermal distribution of the axial mode

$$\rho(E_+, T_+) = \frac{1}{k_B T_+} e^{-\frac{E_+}{k_B T_+}} = \frac{\nu_z}{k_B \nu_+ T_z} e^{-\frac{E_+ \nu_z}{k_B \nu_+ T_z}}, \tag{6.6}$$

where the cyclotron temperature is correspondingly scaled according to $T_+ = \frac{\nu_+}{\nu_z} T_z$ (see chapter 3.2.5). When the coupling drive is switched off, the cyclotron energy will be fixed at its current value. At ALPHATRAP the strong magnetic bottle of the AT can be used to translate the instantaneous cyclotron energy after coupling into a measurable shift of the axial frequency

$$\Delta\nu_z = \frac{1}{(2\pi)^2 m \nu_z} \frac{B_2^{AT}}{B_0^{AT}} E_+^{AT}. \tag{6.7}$$

This way the thermal distribution can be recorded by repeating the sideband coupling between the axial and the reduced cyclotron mode and measuring each time the corresponding shifts of the axial frequency in the AT which maps the Boltzman distribution (see figure 6.14). Note, that when measuring the PT detector temperature the sideband coupling is performed in the PT with $B_0^{PT} = 4.02\,\mathrm{T}$ but the temperature is evaluated in the AT where the magnetic field is reduced by the ferromagnetic ring to $B_0^{AT} = 3.85\,\mathrm{T}$. Due to conservation of angular momentum the

---

[29] This does not hold when the detector input is fed by a negative feedback loop.

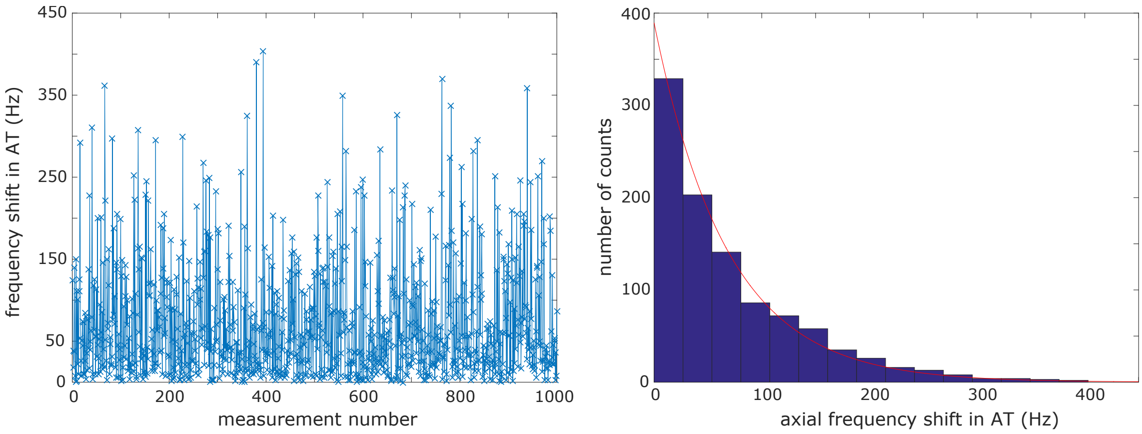

Figure 6.14: Left side: Consecutive measurements of the axial frequency shift in the strong magnetic bottle of the AT after sideband coupling in the PT. In one measurement cycle the axial and reduced cyclotron modes are coupled in the PT and transported to the AT where the corresponding frequency shift is measured. Right side: Histogram of the axial frequency shifts for 1000 measurement cycles. The axial frequency shift data reflects the energy distribution of the reduced cyclotron/axial mode and allows to extract the corresponding mode and detector temperatures, assuming other sources of frequency fluctuations such as voltage changes or energy gained during the transport can be neglected, which was ensured in a separate measurement in section 6.4. Here the exponential fit (red curve) yields $T_z^{PT} = 12.1(4)\,\mathrm{K}$.

reduced cyclotron energy in the AT and PT are therefore not the same but related via

$$E_+^{AT} \approx E_+^{PT} \frac{B_0^{AT}}{B_0^{PT}}. \tag{6.8}$$

Apart from that, the determination of the PT detector temperature additionally requires that the reduced cyclotron energy is not influenced by the adiabatic transport between the traps, which was explicitly verified in section 6.4. The temperature measurement for the axial PT detector is shown in figure 6.14. The axial frequency shift data reflects the energy distribution. A fit to the distribution allows to extract the PT detector temperature $T_z^{PT} = 12.1(4)\,\mathrm{K}$. In a similar way the AT axial and PT cyclotron detector temperatures were measured to $T_z^{AT} = 14.1(4)\,\mathrm{K}$ and $T_{cycl}^{PT} = 28(1)\,\mathrm{K}$. Compared to the lattice temperature the AT and PT detector temperatures are slightly elevated pointing to the existence of residual electronic noise which is currently under investigation. The elevated cyclotron temperature could be explained by the unfavorable operational point[30] of the varactor diode which had to

---

[30] Typically varactor diodes are operated in reverse bias (i.e. "non conducting") direction. To increase the tunable range, the diode was biased in forward direction which potentially can cause an increased current noise at the amplifier input.

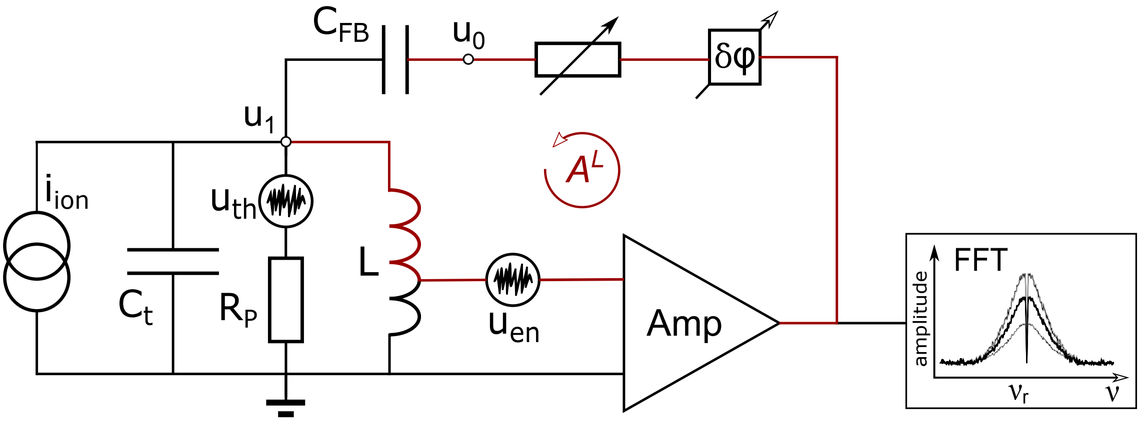

Figure 6.15: Typical circuit to apply electronic feedback. The phase and attenuation of the feedback signal are variable. u_{th} represents the thermal Johnson noise. A^L denotes the complex loop amplification $A^L = u_o/u_1 = |A|e^{i\varphi}$. For a total phase shift of $\varphi = \pm 90°$ it is possible to alter the effective parallel resistance and effective noise temperature of the detector and the ion (see text).

be used at that time in order to allow for adequate tuning of the cyclotron resonator to the reduced cyclotron frequency of the ion.

6.6 Implementation of Electronic Feedback

Active electronic feedback is an effective way to in situ modify the detector noise resonance and consequently its influence on the motion of a resonant ion [141]. Figure 6.15 shows a typical simplified feedback configuration. It allows for a variable phase-shift and attenuation of the output signal before it is fed back to the tuned circuit via a dedicated feedback capacitor C_{FB}. In general the effect of the feedback loop depends on the phase shift of the feedback signal. For a phase shift of 0° or 180°, the otherwise complex loop amplification A^l becomes real with $A^l_{0,180} = \frac{u_0}{u_1} = \pm|A^l|$. From this the effective impedance/capacitance of the feedback capacitor can be calculated [83]

$$Z_{C_{FB}^{eff}} = \frac{u_1}{(u_1 - u_0)i\omega C_{FB}} = \frac{1}{(1 \mp |A^l|)i\omega C_{FB}} \quad \longmapsto \quad C_{FB}^{eff} = (1 \mp |A^l|)C_{FB} \quad (6.9)$$

Thus, by changing $|A^l|$ it is possible to shift the detector resonance frequency in a small range[31] as demonstrated in figure 6.16. In the Mainz experiment this method was used to increase the cooling time constant of the ion during phase sensitive detection in the AT [83]. At ALPHATRAP this task is taken over by the AT frequency switch (chapter 5.1.5). By using a feedback phase of ±90° (i.e. $A^l_{\pm 90} = \pm i|A^l|$) it is

---

[31] Typically a few line widths of the resonator [83]. This is mainly limited by the transfer function and phase response of the overall feedback loop.

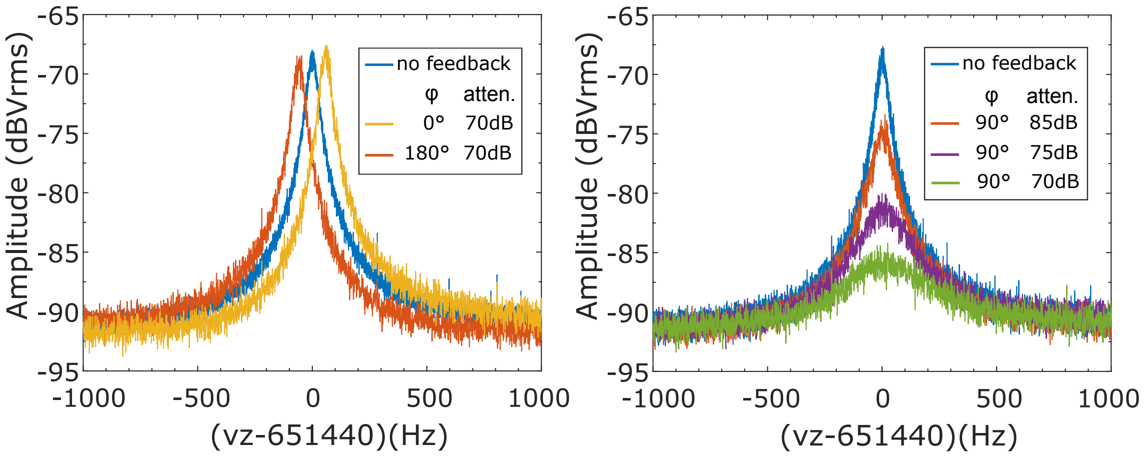

Figure 6.16: Demonstration of electronic feedback. (left side) For 0° and 180° the resonance frequency of the detector can be influenced (see text). (right side) ±90° feedback allows to change the effective parallel resistance and noise temperature of the detector (see text).

even possible to alter the effective parallel resistance (close to resonance frequency ω_r) and noise (electron gas) temperature of the detector circuit [141, 83]:

$$R_p^{eff} = \gamma R_p, \quad T^{eff} = \gamma T \quad \text{with} \quad \gamma = \frac{1}{1 \pm |A| \omega_r R_p C_{FB}} \tag{6.10}$$

where T is the lattice temperature of the resonator. Next to altering the SNR and particle dip width, this allows to simultaneously affect the particle temperature. In particular, the particle temperature can be cooled below the lattice temperature (feedback cooling). To calculate the minimum reachable temperature the finite electronic noise contribution of the cryogenic amplifier has to be considered, which modifies the effective temperature to [83]

$$T_{el}^{eff} = T \left(\gamma + \frac{(\gamma - 1)^2}{\gamma SNR^2} \right). \tag{6.11}$$

This function has a minimum at $\gamma = 1/\sqrt{(SNR^2 - 1)} \approx 1/SNR$ which can be approximated by

$$T_{el,min}^{eff} \approx T \left(\frac{2}{SNR} - \frac{2}{SNR^2} + \frac{1}{SNR^3} \right). \tag{6.12}$$

At ALPHATRAP the measured lattice temperature in the cryo-electronics section is $T \approx 4.5\,\mathrm{K}$ (see figure 4.9). With $SNR_{PT} \approx 23\,\mathrm{dB}$ and $SNR_{AT} \approx 20\,\mathrm{dB}$ the minimum reachable effective temperatures of the PT and AT detector (via feedback cooling) are $T_{min,PT}^{eff} \approx 0.9\,\mathrm{K}$ and $T_{min,AT}^{eff} \approx 1.3\,\mathrm{K}$.

6.7 Direct Observation of Spin-flips

The cyclotron frequency and the Larmor frequency are the two decisive measured quantities for the determination of the g-factor via the experimental approach introduced in chapter 3.1. In contrast to the cyclotron frequency which follows from the trap eigenfrequencies of the ion, the Larmor frequency of the bound electron can't be measured directly. Instead the resonance has to be spectroscopically interrogated by repeated rf excitations around the expected resonance frequency and a subsequent evaluation of the spin state via the continuous Stern-Gerlach effect in the AT. Here, a reliable excitation and an unambiguous detection of spin transitions is of great importance. The underlying spin dynamics are characterized by Rabi oscillations between the spin-up and the spin-down state.

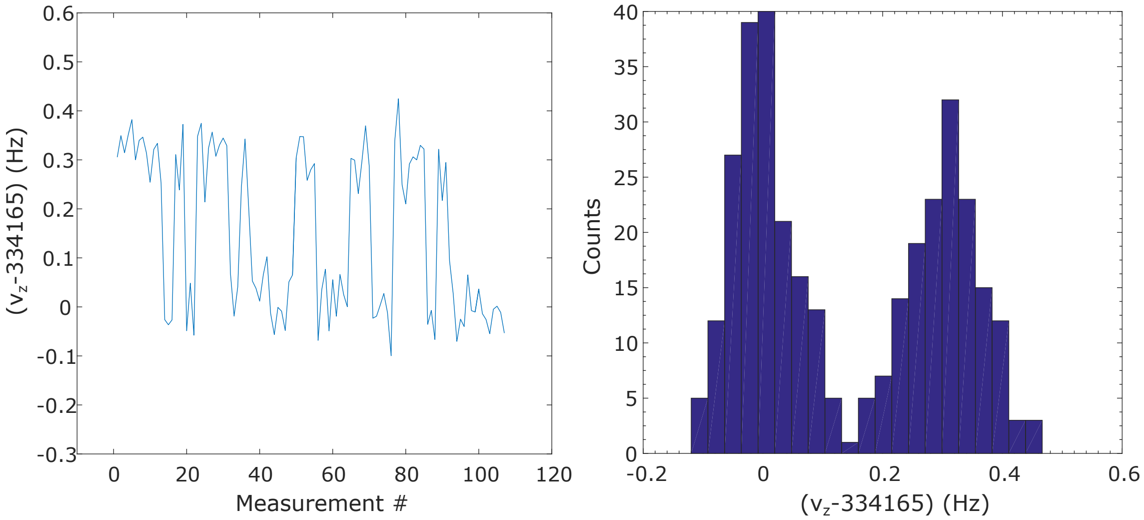

Figure 6.17: (left) First successful excitation and detection of spin flips in the AT using the dip detection technique. (right) The histogrammed data illustrates, that a reliable direct spin-flip detection is possible for boron-like argon. The average spinflip induced axial frequency shift of 310(25)mHz agrees with the expected shift due to the measured B_2 value.

The excitation of spin transitions in the AT is simplified by the fact that the Larmor resonance has a comparably large width, which is mainly caused by the finite motional amplitude of the ion. This is because in the strong magnetic bottle the perceived magnetic field (and therefore the Larmor frequency of the bound electron) sensitively depends on the axial ion position. As a consequence the oscillating ion motion causes a modulation of the Larmor frequency which in general leads to the formation of sidebands at multiples of the axial frequency.

Another line broadening mechanism is caused by the interaction with the axial detector circuit. While in resonance, the ion's axial energy/amplitude and therefore ν_L will fluctuate on timescales of the cooling time constant, reproducing the asymmetric

Boltzman distribution with a $1/e$ width of

$$\delta\nu_L \approx \frac{\nu_L B_2 k_B T_z}{B_0 m (2\pi\nu_z)^2}. \tag{6.13}$$

First spin flip tries in the AT were performed with a single $^{40}\mathrm{Ar}^{13+}$ ion with an expected Larmor frequency of $\nu_L \approx 35.9215\,\mathrm{GHz}$ and an estimated spin-flip related axial frequency shift of 330(5)mHz. Inserting the experimental parameters for the AT in equation (6.13) the resonance width can be estimated to be on the order of $\geq 140\,\mathrm{kHz}$ allowing a quick find of the resonance. Furthermore, during the first attempts an additional broadening (saturration) can be achieved by a generously selected rf (MW) excitation power. As can be seen in figure 6.17 for boron-like argon the currently achieved axial frequency stability in the AT allows for definite spin flip detection with an error rate of less than ~3 %. The measured average spin-flip induced axial frequency shift of 310(25)mHz corresponds to a magnetic bottle of $B_2 = 44\,135(3560)\,\mathrm{T/m^2}$, in accordance with the previously measured value. It was observed, that reliable excitation of spin transitions with excitation times of only 2s and source power of $-15\,\mathrm{dBm}$ (~31 µW) could be achieved speaking for a good MW power transmission into the AT contributing to an efficient spin state analysis and a reduction of the overall measurement time.

7 Conclusion and Outlook

Conclusion: ALPHATRAP is a next generation g-factor experiment aiming to extend the range of high-precision BS-QED tests into the regime of extreme electromagnetic fields. This can be achieved by measuring the bound electron g-factor of single HCI up to hydrogenike lead $^{208}\mathrm{Pb}^{81+}$ stored in the highly stable trapping field of a cryogenic Penning-trap apparatus. During my time as a PhD student I had the privilege to be a witness and part of the full development process of this exciting venture.
A major part of this thesis was dedicated to the assembly of the ALPHATRAP experiment including the development, implementation and testing of essential components with a main focus on the electronic detection system. After completing the construction the experiment was cooled down via the homebuilt cryostat reaching close to liquid helium temperature. The cryostat showed good holding performance of the cryogenic liquids allowing for an undisturbed measurement time of $\geq$4 days. Shortly after, the commissioning phase of the whole experiment with HCI began. In a first commissioning run highly charged carbon ions $^{12}\mathrm{C}^{5+}$ were created with an in trap EBIS which was provisionally installed inside the cryogenic trap chamber. By employing state-of-the-art cleaning techniques and adiabatic ion transport this led to the first successful detection of a single HCI in the precision and the analysis trap. In a second commissioning run a major breakthrough was achieved by the first injection of externally produced HCI. At that time the beamline coupling section to the HD-EBIT was not finished yet. Therefore, the injection was performed with highly charged argon ions $^{40}\mathrm{Ar}^{13+}$, which were supplied by the HC-EBIT and pre-decelerated to kinetic energies $< 100\,\mathrm{eV} \cdot \mathrm{q}$ by the pulsed drift tube within the beamline. The reliable detection, characterization and capturing of ion bunches in the capture section was made possible using the new cryogenic charge sensitive detectors. An important feature of ALPHATRAP is the cryogenic valve which was integrated in the cryogenic beamtube. After external injection the valve can be closed in order to ensure good vacuum conditions despite the coupling to the room temperature beamline. A drive coupling mechanism allows to decouple the valve from the room temperature manipulator while it is not in use. With this, the additional effective thermal load on the cryostat stages was found to be negligible. The cryo-valve was successfully tested by storing a single $^{40}\mathrm{Ar}^{13+}$ over an extended time period of 4 months which corresponds to an estimated trap chamber pressure of at least $3 \cdot 10^{-18}$ mbar. This is encouraging, since it will enable measurements with storage times on the order of $\geq$ 3 weeks even for HCI as the sought after $^{208}\mathrm{Pb}^{81+}$. Furthermore the commissioning also comprised first characterization measurements and tests of the trap assembly and the detection system. For instance the functional-

ity of the excitation lines and switches was demonstrated via exemplary bolometric measurements of all three eigenfrequencies of a single HCI in the precision trap. The overall performance of the resonant detectors in the analysis and the precision trap fulfilled the expectations reaching signal-to-noise ratios >20 dB. However, a later measurement of the ion temperature revealed that the effective detector temperatures are exceeding the ambient lattice temperature by a factor of ~ 3, possibly indicating the existence of a yet unknown electronic noise contribution. Nevertheless, considering the measured residual leading order trapping field imperfections the corresponding systematic cyclotron frequency shifts due to the elevated detector/ion temperature do not exceed a few ppt. A closer analysis of other potential systematic errors is still pending. Apart from that, first bolometric stability measurements of the ion eigenfrequencies suggest, that for now the overall achievable relative uncertainty for the g-factor is in the lower 10^{-9} level being mainly limited by the incoherent sideband detection technique which was used throughout commissioning. In this context, the full capabilities of ALPHATRAP will be unlocked not before the use of the superior phase sensitive detection technique PnA [83] which will be implemented in the near future.
Finally, after the installation of the millimeter-wave guide, the commissioning experiments peaked in the very first direct detection of induced spin transitions completing the necessary ingredients to perform g-factor measurements and demonstrating the full functionality of ALPHATRAP which was also the intended goal of this work.

Outlook: While this thesis was written tremendous progress has been made on account of the inexhaustible creativity and effort of my colleagues. Some of the achievements are:

- The very first g-factor measurement at ALPHATRAP based on the spin-flip detection method discussed within this thesis. The measurement was performed on the ground-state electron in boron-like $^{40}\mathrm{Ar}^{13+}$ and is currently being evaluated [105]. The result will contribute to resolve the current discrepancy between different theoretically predicted values [142, 143, 144].

- Successful laser cooling has been demonstrated on stored beryllium ions [19], an encouraging step on the way towards sympathetic laser cooling of HCI at ALPHATRAP. In combination with the new highly harmonic precision trap design and the upcoming implementation of PnA this will hopefully allow to access the targeted relative precision level of 10^{-11} and below.

- Furthermore the new microwave and laser injection system also led to the development and successful test of an entirely new measurement technique which combines laser-spectroscopy with the continuous Stern-Gerlach effect, thus, being independent of fluorescent detection. Via this new approach measurements of fine structure transitions in HCI became possible at ALPHATRAP as has been recently demonstrated for the $2\mathrm{p}_{1/2} - 2\mathrm{p}_{3/2}$ fine structure in $^{40}\mathrm{Ar}^{13+}$[19]. In even heavier systems the same technique could also be employed for hyperfine structure transitions enabling independent measurements of nuclear magnetic moments in order to reduce the dominant source of uncertainty in the corresponding BS-QED calculations.

After the finalization of the beamline connection to the HD-EBIT [145] the accessible systems will finally allow to step into the strong field regime of up to 10^{18} V/m which is two order of magnitudes higher than in the predecessor experiments. Next to stringent BS-QED tests also the possibility to perform independent high-precision measurement of fundamental constants as the electron mass and ultimately the determination of the fine structure constant make out the highly exciting future prospects of ALPHATRAP.

8 Bibliography

[1] Dirac, Paul A.: The quantum theory of the electron. In: *Proc. R. Soc. Lond. A* Bd. 117 The Royal Society, 1928, S. 610–624

[2] Kiefer, Claus: Quantum gravity: general introduction and recent developments. In: *Annalen der Physik* 15 (2006), Nr. 1-2, S. 129–148

[3] Ross, Graham G.: *Grand Unified Theories.* Westview Press, 1984

[4] Georgi, Howard ; Glashow, Sheldon L.: Unity of all elementary-particle forces. In: *Physical Review Letters* 32 (1974), Nr. 8, S. 438

[5] Beyer, Axel ; Maisenbacher, Lothar ; Matveev, Arthur ; Pohl, Randolf ; Khabarova, Ksenia ; Grinin, Alexey ; Lamour, Tobias ; Yost, Dylan C. ; Hänsch, Theodor W. ; Kolachevsky, Nikolai u. a.: The Rydberg constant and proton size from atomic hydrogen. In: *Science* 358 (2017), Nr. 6359, S. 79–85

[6] Hayakawa, Masashi: Theory of Anomalous Magnetic Dipole Moments of the Electron. In: *Springer Tracts in Modern Physics* 256 (2014), 01, S. 41–71

[7] Jegerlehner, Fred ; Nyffeler, Andreas: The muon g- 2. In: *Physics Reports* 477 (2009), Nr. 1-3, S. 1–110

[8] Louisell, WH ; Pidd, RW ; Crane, HR: An experimental measurement of the gyromagnetic ratio of the free electron. In: *Physical Review* 94 (1954), Nr. 1, S. 7

[9] Hanneke, D ; Fogwell, S ; Gabrielse, G: New measurement of the electron magnetic moment and the fine structure constant. In: *Physical Review Letters* 100 (2008), Nr. 12, S. 120801

[10] Hanneke, D ; Hoogerheide, S F. ; Gabrielse, G: Cavity control of a single-electron quantum cyclotron: Measuring the electron magnetic moment. In: *Physical Review A* 83 (2011), Nr. 5, S. 052122

[11] Bouchendira, Rym ; Cladé, Pierre ; Guellati-Khélifa, Saïda ; Nez, François ; Biraben, François: New determination of the fine structure constant and test of the quantum electrodynamics. In: *Physical Review Letters* 106 (2011), Nr. 8, S. 080801

[12] Aoyama, Tatsumi ; Hayakawa, Masashi ; Kinoshita, Toichiro ; Nio, Makiko: Tenth-order electron anomalous magnetic moment: contribution of diagrams without closed lepton loops. In: *Physical Review D* 91 (2015), Nr. 3, S. 033006

[13] Schwinger, Julian: On gauge invariance and vacuum polarization. In: *Physical Review* 82 (1951), Nr. 5, S. 664

[14] Stöhlker, Th ; Mokler, PH ; Bosch, F ; Dunford, RW ; Franzke, F ; Klepper, O ; Kozhuharov, C ; Ludziejewski, T ; Nolden, F ; Reich, H u. a.: 1 s Lamb shift in hydrogenlike uranium measured on cooled, decelerated ion beams. In: *Physical review letters* 85 (2000), Nr. 15, S. 3109

[15] Seelig, P ; Borneis, S ; Dax, A ; Engel, T ; Faber, S ; Gerlach, M ; Holbrow, C ; Huber, G ; Kühl, T ; Marx, D u. a.: Ground State Hyperfine Splitting of Hydrogenlike 207 Pb 8 1+ by Laser Excitation of a Bunched Ion Beam in the GSI Experimental Storage Ring. In: *Physical review letters* 81 (1998), Nr. 22, S. 4824

[16] Ullmann, Johannes ; Andelkovic, Zoran ; Brandau, Carsten ; Dax, Andreas ; Geithner, Wolfgang ; Geppert, Christopher ; Gorges, Christian ; Hammen, Michael ; Hannen, Volker ; Kaufmann, Simon u. a.: High precision hyperfine measurements in Bismuth challenge bound-state strong-field QED. In: *Nature communications* 8 (2017), S. 15484

[17] Shabaev, VM ; Artemyev, AN ; Yerokhin, VA ; Zherebtsov, OM ; Soff, G: Towards a test of QED in investigations of the hyperfine splitting in heavy ions. In: *Physical review letters* 86 (2001), Nr. 18, S. 3959

[18] Shabaev, VM ; Glazov, DA ; Shabaeva, MB ; Yerokhin, VA ; Plunien, G ; Soff, G: g factor of high-Z lithiumlike ions. In: *Physical Review A* 65 (2002), Nr. 6, S. 062104

[19] Egl, Alexander: *In Preparation*, Ruprecht-Karls-Universität Heidelberg, Diss., 2019

[20] Häffner, H ; Beier, Th ; Hermanspahn, N ; Kluge, H-J ; Quint, W ; Stahl, S ; Verdú, J ; Werth, G: High-accuracy measurement of the magnetic moment anomaly of the electron bound in hydrogenlike carbon. In: *Physical review letters* 85 (2000), Nr. 25, S. 5308

[21] Verdú, José ; Djekić, S ; Stahl, S ; Valenzuela, T ; Vogel, M ; Werth, G ; Beier, T ; Kluge, H-J ; Quint, W: Electronic g Factor of Hydrogenlike Oxygen O 7+ 16. In: *Physical review letters* 92 (2004), Nr. 9, S. 093002

[22] Sturm, Sven ; Wagner, Anke ; Schabinger, Birgit ; Blaum, Klaus: Phase-sensitive cyclotron frequency measurements at ultralow energies. In: *Physical review letters* 107 (2011), Nr. 14, S. 143003

[23] Sturm, Sven ; Wagner, Anke ; Schabinger, Birgit ; Zatorski, Jacek ; Harman, Zoltan ; Quint, Wolfgang ; Werth, Günter ; Keitel, Christoph H. ; Blaum, Klaus: g Factor of Hydrogenlike Si 13+ 28. In: *Physical review letters* 107 (2011), Nr. 2, S. 023002

[24] Wagner, Anke ; Sturm, Sven ; Köhler, Florian ; Glazov, Dmitry A. ; Volotka, Andrey V. ; Plunien, Günter ; Quint, Wolfgang ; Werth, Günter ; Shabaev, Vladimir M. ; Blaum, Klaus: g Factor of Lithiumlike Silicon Si 11+ 28. In: *Physical review letters* 110 (2013), Nr. 3, S. 033003

[25] Beier, Thomas ; Häffner, Hartmut ; Hermanspahn, Nikolaus ; Karshenboim, Savely G. ; Kluge, H-Jürgen ; Quint, Wolfgang ; Stahl, Stefan ; Verdú, José ; Werth, Günther: New determination of the electron's mass. In: *Physical review letters* 88 (2001), Nr. 1, S. 011603

[26] Sturm, Sven ; Köhler, Florian ; Zatorski, Jacek ; Wagner, Anke ; Harman, Zoltán ; Werth, Günter ; Quint, Wolfgang ; Keitel, Christoph H. ; Blaum, Klaus: High-precision measurement of the atomic mass of the electron. In: *Nature* 506 (2014), Nr. 7489, S. 467

[27] Köhler, Florian ; Sturm, Sven ; Kracke, Anke ; Werth, Günter ; Quint, Wolfgang ; Blaum, Klaus: The electron mass from g-factor measurements on hydrogen-like carbon 12C5+. In: *Journal of Physics B: Atomic, Molecular and Optical Physics* 48 (2015), Nr. 14, S. 144032

[28] Köhler, Florian ; Blaum, Klaus ; Block, Michael ; Chenmarev, Stanislav ; Eliseev, Sergey ; Glazov, Dmitry A. ; Goncharov, Mikhail ; Hou, Jiamin ; Kracke, Anke ; Nesterenko, Dmitri A. u. a.: Isotope dependence of the Zeeman effect in lithium-like calcium. In: *Nature communications* 7 (2016), S. 10246

[29] Heisse, Fabian ; Köhler-Langes, Florian ; Rau, Sascha ; Hou, Jamin ; Junck, Sven ; Kracke, Anke ; Mooser, Andreas ; Quint, Wolfgang ; Ulmer, Stefan ; Werth, Günter u. a.: High-precision measurement of the proton's atomic mass. In: *Physical review letters* 119 (2017), Nr. 3, S. 033001

[30] Crespo Lopez-Urrutia, JR ; Braun, J ; Brenner, G ; Bruhns, H ; Lapierre, A ; Gonzalez Martinez, AJ ; Mironov, V ; Soria Orts, R ; Tawara, H ; Trinczek, M u. a.: Optimization of the charge state distribution of the ion beam extracted from an EBIT by dielectronic recombination. In: *Review of scientific instruments* 75 (2004), Nr. 5, S. 1560–1562

[31] Sailer, Tim: *A Laser Ion Source for the Alphatrap Experiment.* Ruprecht-Karls-Universität Heidelberg, Master's Thesis, 2017

[32] Buchauer, Lisa: *Konstruktion einer kompakten Elektronenstrahl-Ionenfalle mit Permanentmagneten für Fluoreszenzmessungen*, Ruprecht-Karls-Universität Heidelberg, Diplomarbeit, 2012

[33] Feynman, Richard P. ; Leighton, Robert B. ; Sands, Matthew: *Lectures on Physics, vol. III.* Addison-Wesley Reading (Mass), 1965

[34] Sommerfeld, Arnold: Zur quantentheorie der spektrallinien. In: *Annalen der Physik* 356 (1916), Nr. 17, S. 1–94

[35] Kinsler, LE ; Houston, WV: The Value of e/m from the Zeeman Effect. In: *Physical Review* 45 (1934), Nr. 2, S. 104

[36] Dirac, Paul A.: The quantum theory of the emission and absorption of radiation. In: *Proc. R. Soc. Lond. A* Bd. 114 The Royal Society, 1927, S. 243–265

[37] Oppenheimer, J R.: Note on the theory of the interaction of field and matter. In: *Physical Review* 35 (1930), Nr. 5, S. 461

[38] Lamb Jr, Willis E. ; Retherford, Robert C.: Fine structure of the hydrogen atom by a microwave method. In: *Physical Review* 72 (1947), Nr. 3, S. 241

[39] Nafe, John E. ; Nelson, Edward B. ; Rabi, Isidor I.: The hyperfine structure of atomic hydrogen and deuterium. In: *Physical Review* 71 (1947), Nr. 12, S. 914

[40] Breit, Gregory: Does the electron have an intrinsic magnetic moment? In: *Physical Review* 72 (1947), Nr. 10, S. 984

[41] Bethe, Hans A.: The electromagnetic shift of energy levels. In: *Physical Review* 72 (1947), Nr. 4, S. 339

[42] Tomonaga, Sin-itiro: On a relativistically invariant formulation of the quantum theory of wave fields. In: *Progress of Theoretical Physics* 1 (1946), Nr. 2, S. 27–42

[43] Schwinger, Julian: Quantum electrodynamics. I. A covariant formulation. In: *Physical Review* 74 (1948), Nr. 10, S. 1439

[44] Feynman, Richard P.: The theory of positrons. In: *Physical Review* 76 (1949), Nr. 6, S. 749

[45] Dyson, Freeman J.: The radiation theories of Tomonaga, Schwinger, and Feynman. In: *Physical Review* 75 (1949), Nr. 3, S. 486

[46] Kusch, P ; Foley, HM: The magnetic moment of the electron. In: *Physical Review* 74 (1948), Nr. 3, S. 250

[47] Dorr, Joshua C.: *Quantum Jump Spectroscopy of a Single Electron in a New and Improved Apparatus.* Harvard University, 2013

[48] Feynman, Richard P.: Space-time approach to quantum electrodynamics. In: *Physical Review* 76 (1949), Nr. 6, S. 769

[49] Laporta, Stefano: High-precision calculation of the 4-loop contribution to the electron g-2 in QED. In: *Physics Letters B* 772 (2017), S. 232–238

[50] Kinoshita, Toichiro: TENTH-ORDER QED CONTRIBUTION TO THE ELECTRON g- 2 AND HIGH PRECISION TEST OF QUANTUM ELECTRODYNAMICS. In: *Proceedings Of The Conference In Honour Of The 90th Birthday Of Freeman Dyson* World Scientific, 2014, S. 148–172

[51] Parker, Richard ; Yu, Chenghui ; Zhong, Weicheng ; Estey, Brian ; Müller, Holger: Measurement of the fine-structure constant as a test of the Standard Model. 360 (2018), 04, S. 191–195

[52] Yanovsky, V ; Chvykov, V ; Kalinchenko, G ; Rousseau, P ; Planchon, T ; Matsuoka, T ; Maksimchuk, A ; Nees, J ; Cheriaux, G ; Mourou, G u. a.: Ultra-high intensity-300-TW laser at 0.1 Hz repetition rate. In: *Optics Express* 16 (2008), Nr. 3, S. 2109–2114

[53] Di Piazza, A ; Müller, C ; Hatsagortsyan, KZ ; Keitel, CH: Extremely high-intensity laser interactions with fundamental quantum systems. In: *Reviews of Modern Physics* 84 (2012), Nr. 3, S. 1177

[54] Darwin, Charles G.: The wave equations of the electron. In: *Proceedings of the Royal Society of London. Series A* 118 (1928), Nr. 780, S. 654–680

[55] Gordon, Walter: Die energieniveaus des wasserstoffatoms nach der diracschen quantentheorie des elektrons. In: *Zeitschrift für Physik A Hadrons and Nuclei* 48 (1928), Nr. 1, S. 11–14

[56] Breit, G: The magnetic moment of the electron. In: *Nature* 122 (1928), Nr. 3078, S. 649

[57] Furry, WH: On bound states and scattering in positron theory. In: *Physical Review* 81 (1951), Nr. 1, S. 115

[58] Beier, Thomas: The gj factor of a bound electron and the hyperfine structure splitting in hydrogenlike ions. In: *Physics Reports* 339 (2000), Nr. 2-3, S. 79–213

[59] Blundell, SA ; Cheng, KT ; Sapirstein, J: Radiative corrections in atomic physics in the presence of perturbing potentials. In: *Physical Review A* 55 (1997), Nr. 3, S. 1857

[60] Yerokhin, VA ; Indelicato, P ; Shabaev, VM: Evaluation of the self-energy correction to the g factor of S states in H-like ions. In: *Physical Review A* 69 (2004), Nr. 5, S. 052503

[61] Beier, Thomas ; Lindgren, Ingvar ; Persson, Hans ; Salomonson, Sten ; Sunnergren, Per ; Häffner, Hartmut ; Hermanspahn, Nikolaus: g j Factor of an electron bound in a hydrogenlike ion. In: *Physical Review A* 62 (2000), Nr. 3, S. 032510

[62] Jentschura, Ulrich D.: Binding two-loop vacuum-polarization corrections to the bound-electron g factor. In: *Physical Review A* 79 (2009), Nr. 4, S. 044501

[63] Czarnecki, Andrzej ; Szafron, Robert: Light-by-light scattering in the Lamb shift and the bound electron g factor. In: *Physical Review A* 94 (2016), Nr. 6, S. 060501

[64] Czarnecki, Andrzej ; Dowling, Matthew ; Piclum, Jan ; Szafron, Robert: Two-Loop Binding Corrections to the Electron Gyromagnetic Factor. In: *Phys. Rev. Lett.* 120 (2018), Jan, S. 043203

[65] Sturm, Sven ; Arapoglou, Ioanna ; Blaum, Klaus ; Egl, Alexander ; Höcker, Martin ; Krämer, Sandro ; Sailer, Tim ; Tu, Bingsheng ; Weigel, Andreas ; Wolf, Robert u. a.: The Alphatrap Experiment. In: *The European Physical Journal Special Topics* (2018)

[66] Volotka, AV ; Glazov, DA ; Shabaev, VM ; Tupitsyn, II ; Plunien, G: Many-electron QED corrections to the g factor of lithiumlike ions. In: *Physical review letters* 112 (2014), Nr. 25, S. 253004

[67] Glazov, DA ; Shabaev, VM: Finite nuclear size correction to the bound-electron/g factor in a hydrogenlike atom. In: *Physics Letters A* 297 (2002), S. 408–411

[68] Karshenboim, Savely G. ; Ivanov, Vladimir G.: Finite-nuclear-size contribution to the g factor of a bound electron: Higher-order effects. In: *Phys. Rev. A* 97 (2018), Feb, S. 022506

[69] Zatorski, Jacek ; Oreshkina, Natalia S. ; Keitel, Christoph H. ; Harman, Zoltán: Nuclear shape effect on the g factor of hydrogenlike ions. In: *Physical review letters* 108 (2012), Nr. 6, S. 063005

[70] Nefiodov, AV ; Plunien, G ; Soff, G: Nuclear-polarization correction to the bound-electron g factor in heavy hydrogenlike ions. In: *Physical review letters* 89 (2002), Nr. 8, S. 081802

[71] Volotka, Andrey V. ; Plunien, Günter: Nuclear polarization study: new frontiers for tests of qed in heavy highly charged ions. In: *Physical review letters* 113 (2014), Nr. 2, S. 023002

[72] Shabaev, VM: QED theory of the nuclear recoil effect on the atomic g factor. In: *Physical Review A* 64 (2001), Nr. 5, S. 052104

[73] Shabaev, VM ; Yerokhin, VA: Recoil Correction to the Bound-Electron g Factor in H-Like Atoms to All Orders in α Z. In: *Physical review letters* 88 (2002), Nr. 9, S. 091801

[74] Bohr, Aage ; Weisskopf, VF: The influence of nuclear structure on the hyperfine structure of heavy elements. In: *Physical Review* 77 (1950), Nr. 1, S. 94

[75] Repp, Julia ; Böhm, Christine ; López-Urrutia, JR C. ; Dörr, Andreas ; Eliseev, Sergey ; George, Sebastian ; Goncharov, Mikhail ; Novikov, Yuri N. ; Roux, Christian ; Sturm, Sven u. a.: PENTATRAP: a novel cryogenic multi-Penning-trap experiment for high-precision mass measurements on highly charged ions. In: *Applied Physics B* 107 (2012), Nr. 4, S. 983–996

[76] Weigel, Andreas ; Blaum, Klaus ; Sturm, Sven: *Entwicklung des kryogenen Nachweissystems für ALPHATRAP und THe-Trap*. Ruprecht-Karls-Universität Heidelberg, Master's Thesis, 2014

[77] Penning, Frans M.: Die Glimmentladung bei niedrigem Druck zwischen koaxialen Zylindern in einem axialen Magnetfeld. In: *physica* 3 (1936), Nr. 9, S. 873–894

[78] Blaum, Klaus ; Novikov, Yu N. ; Werth, Günther: Penning traps as a versatile tool for precise experiments in fundamental physics. In: *Contemporary Physics* 51 (2010), Nr. 2, S. 149–175

[79] Brown, Lowell S. ; Gabrielse, Gerald: Geonium theory: Physics of a single electron or ion in a Penning trap. In: *Reviews of Modern Physics* 58 (1986), Nr. 1, S. 233

[80] Wagner, Anke A.: *The g-factor of the valence electron bound in lithiumlike silicon 28Si11+: The most stringent test of relativistic many-electron calculations in a magnetic field*, Johannes Gutenberg-Universität Mainz, Diss., 2013

[81] Brown, Lowell S. ; Gabrielse, Gerald: Precision spectroscopy of a charged particle in an imperfect Penning trap. In: *Physical Review A* 25 (1982), Nr. 4, S. 2423

[82] Ketter, Jochen ; Eronen, Tommi ; Höcker, Martin ; Schuh, Marc ; Streubel, Sebastian ; Blaum, Klaus: Classical calculation of relativistic

frequency-shifts in an ideal Penning trap. In: *International Journal of Mass Spectrometry* 361 (2014), S. 34–40

[83] Sturm, Sven ; Heil, Werner ; Blaum, Klaus: *The g-factor of the electron bound in 28Si13+: The most stringent test of bound-state quantum electrodynamics*, Johannes-Gutenberg Universität Mainz, Diss., 2012

[84] Thomas, Llewellyn H.: The motion of the spinning electron. In: *Nature* 117 (1926), Nr. 2945, S. 514

[85] Tan, Joseph ; Gabrielse, Gerald: One electron in an orthogonalized cylindrical Penning trap. In: *Applied physics letters* 55 (1989), Nr. 20, S. 2144–2146

[86] Ketter, Jochen ; Eronen, Tommi ; Höcker, Martin ; Streubel, Sebastian ; Blaum, Klaus: First-order perturbative calculation of the frequency-shifts caused by static cylindrically-symmetric electric and magnetic imperfections of a Penning trap. In: *International Journal of Mass Spectrometry* 358 (2014), S. 1–16

[87] Häffner, H: *Präzisionsmessung des magnetischen Moments des Elektrons in wasserstoffähnlichem Kohlenstoff.*, Johannes Gutenberg-Universität Mainz, Diss., 2000

[88] Galiana, José Luis V.: *Ultrapräzise Messung des elektronischen g-Faktors in wasserstoffähnlichem Sauerstoff*, Johannes Gutenberg-Universität Mainz, Diss., 2003

[89] Dehmelt, HG ; Walls, FL: " Bolometric" Technique for the rf Spectroscopy of Stored Ions. In: *Physical Review Letters* 21 (1968), Nr. 3, S. 127

[90] Shockley, William: Currents to conductors induced by a moving point charge. In: *Journal of applied physics* 9 (1938), Nr. 10, S. 635–636

[91] Nyquist, Harry: Thermal agitation of electric charge in conductors. In: *Physical review* 32 (1928), Nr. 1, S. 110

[92] Johnson, John B.: Thermal agitation of electricity in conductors. In: *Physical review* 32 (1928), Nr. 1, S. 97

[93] Natarajan, Vasant: *Penning trap mass spectroscopy at 0.1 ppb*, Massachusetts Institute of Technology, Diss., 1993

[94] Wineland, DJ ; Dehmelt, HG: Principles of the stored ion calorimeter. In: *Journal of Applied Physics* 46 (1975), Nr. 2, S. 919–930

[95] Ulmer, Stefan: *First observation of spin flips with a single proton stored in a cryogenic Penning trap*, Ruprecht-Karls-Universität Heidelberg, Diss., 2011

[96] Cornell, Eric A. ; Weisskoff, Robert M. ; Boyce, Kevin R. ; Pritchard, David E.: Mode coupling in a Penning trap: π pulses and a classical avoided crossing. In: *Physical Review A* 41 (1990), Nr. 1, S. 312

[97] Stern, Otto: Ein Weg zur experimentellen Prüfung der Richtungsquantelung im Magnetfeld. In: *Zeitschrift für Physik* 7 (1921), Nr. 1, S. 249–253

[98] Gerlach, Walther ; Stern, Otto: Der experimentelle nachweis der richtungsquantelung im magnetfeld. In: *Zeitschrift für Physik* 9 (1922), Nr. 1, S. 349–352

[99] Batelaan, Herman ; Gay, Timothy J. ; Schwendiman, JJ: Stern-Gerlach effect for electron beams. In: *Physical review letters* 79 (1997), Nr. 23, S. 4517

[100] Van Dyck Jr, Robert S. ; Schwinberg, Paul B. ; Dehmelt, Hans G.: Electron magnetic moment from geonium spectra: Early experiments and background concepts. In: *Physical Review D* 34 (1986), Nr. 3, S. 722

[101] Dehmelt, Hans: Continuous Stern-Gerlach effect: principle and idealized apparatus. In: *Proceedings of the National Academy of Sciences* 83 (1986), Nr. 8, S. 2291–2294

[102] Hermanspahn, N ; Häffner, H ; Kluge, H-J ; Quint, W ; Stahl, S ; Verdú, J ; Werth, G: Observation of the continuous Stern-Gerlach effect on an electron bound in an atomic ion. In: *Physical review letters* 84 (2000), Nr. 3, S. 427

[103] Ulmer, Stefan ; Smorra, Christian: The magnetic moments of the proton and the antiproton. In: *Fundamental Physics in Particle Traps.* Springer, 2014, S. 165–201

[104] Köhler, Florian ; Quint, Wolfgang ; Jochim, Selim: *Bound-Electron g-Factor Measurements for the Determination of the Electron Mass and Isotope Shifts in Highly Charged Ions*, Ruprecht-Karls-Universität Heidelberg, Diss., 2015

[105] Arapoglou, Ioanna: *In Preparation*, Ruprecht-Karls-Universität Heidelberg, Diss., 2019

[106] López-Urrutia, JR C. ; Braun, J ; Brenner, Gunter ; Bruhns, Hardo ; Dimopoulou, Christina ; Draganić, IN ; Fischer, Daniel ; Martínez, AJ G. ; Lapierre, A ; Mironov, V u. a.: Progress at the Heidelberg EBIT. In: *Journal of Physics: Conference Series* Bd. 2 IOP Publishing, 2004, S. 42

[107] Egl, Alexander: *Commissioning of the offline transfer beamline for the ALPHATRAP experiment.* Ruprecht-Karls-Universität Heidelberg, Master's Thesis, 2016

[108] Hirzler, H: *Aufbau und Test der Transferbeamline für das ALPHATRAP Projekt.* Ruprecht-Karls-Universität Heidelberg, Bachelor's Thesis, 2014

[109] Penetrante, BM ; Bardsley, JN ; DeWitt, D ; Clark, M ; Schneider, D: Evolution of ion-charge-state distributions in an electron-beam ion trap. In: *Physical Review A* 43 (1991), Nr. 9, S. 4861

[110] Simon, MC ; Schwarz, M ; Epp, SW ; Beilmann, C ; Schmitt, BL ; Harman, Z ; Baumann, TM ; Mokler, PH ; Bernitt, S ; Ginzel, R u. a.: Photoionization of N3+ and Ar8+ in an electron beam ion trap by synchrotron radiation. In: *Journal of Physics B: Atomic, Molecular and Optical Physics* 43 (2010), Nr. 6, S. 065003

[111] Micke, P ; Kühn, S ; Buchauer, L ; Harries, JR ; Bücking, TM ; Blaum, K ; Cieluch, A ; Egl, A ; Hollain, D ; Kraemer, S u. a.: The Heidelberg compact electron beam ion traps. In: *Review of Scientific Instruments* 89 (2018), Nr. 6, S. 063109

[112] Mann, R: Total one-electron capture cross sections for Ar q+ and I q+ ions in slow collisions on H 2 and He. In: *Zeitschrift für Physik D Atoms, Molecules and Clusters* 3 (1986), Nr. 1, S. 85–90

[113] Turkalj Orešković, Marko: *Development of a cryogenic vacuum valve and an electromechanical switch for ALPHATRAP.* Heidelberg : Ruprecht-Karls-Universität Heidelberg, Master's Thesis, 2014

[114] Benvenuti, Cristoforo: Molecular surface pumping: cryopumping / Cern. 1999. – Forschungsbericht

[115] Hermanspahn, N: *Das magnetische Moment des gebundenen Elektrons in wasserstoffartigem Kohlenstoff (C 5+).*, Johannes-Gutenberg Universität Mainz, Diss., 1999

[116] Kraemer, S.: *Aufbau und Charakterisierung eines Geschwindigkeitsfilters für das ALPHATRAP-Experiment.* Ruprecht-Karls-Universität Heidelberg, Bachelor's Thesis, 2014

[117] Hobein, Matthias ; Solders, Andreas ; Liu, Yuwen ; Ketelaer, Jens ; Linné, M S. ; Marx, G ; Schuch, Reinhold: SMILETRAP II. In: *Hyperfine Interactions* 199 (2011), Nr. 1-3, S. 141–150

[118] White, Guy K.: Experimental techniques in low-temperature physics. (1987)

[119] Ulmer, Stefan: *Entwicklung des experimentellen Aufbaus zur Messung des g-Faktors des Protons in einer Penning-Falle.* Ruprecht-Karls-Universität Heidelberg, Diplomarbeit, 2006

[120] Baehr, Hans D. ; Stephan, Karl: *Wärme-und stoffübertragung.* Bd. 7. Springer, 1994

[121] Marquardt, ED ; Le, JP ; Radebaugh, Ray: Cryogenic Material Properties Database. (2000)

[122] Van Sciver, Steven W.: Low-temperature materials properties. In: *Helium Cryogenics.* Springer, 2012, S. 17–58

[123] Schulte, EH: Carbon resistors for cryogenic temperature measurement. In: *Cryogenics* 6 (1966), Nr. 6, S. 321–323

[124] Steinsberger, Timo: *Microwave injection for the ALPHATRAP experiment and developments of the multi-reflection time-of-flight technique of the ISOLTRAP experiment.* Ruprecht-Karls-Universität Heidelberg, Master's Thesis, 2018

[125] Dörr, Andreas ; Blaum, Klaus ; Jochim, Selim: *PENTATRAP: A novel Penning-trap system for high-precision mass measurements*, Ruprecht-Karls-Universität Heidelberg, Diss., 2015

[126] Jefferts, Steven R. ; Heavner, T ; Hayes, P ; Dunn, GH: Superconducting resonator and a cryogenic GaAs field-effect transistor amplifier as a single-ion detection system. In: *Review of scientific instruments* 64 (1993), Nr. 3, S. 737–740

[127] Weisskoff, Robert M.: *Detecting single, trapped ions*, Massachusetts Institute of Technology, Diss., 1988

[128] Lengeler, B: Semiconductor devices suitable for use in cryogenic environments. In: *Cryogenics* 14 (1974), Nr. 8, S. 439–447

[129] Horowitz, Paul ; Hill, Winfield: *The art of electronics.* Cambridge Univ. Press, 1989

[130] Ulmer, Stefan ; Kracke, Holger ; Blaum, Klaus ; Kreim, Susanne ; Mooser, Andreas ; Quint, Wolfgang ; Rodegheri, Cricia C. ; Walz, Jochen: The quality factor of a superconducting rf resonator in a magnetic field. In: *Review of Scientific Instruments* 80 (2009), Nr. 12, S. 123302

[131] Pavičić, DZ ; Maglić, KD: Specific heat and electrical resistivity of 53% niobium-47% titanium alloy measured by subsecond calorimetric technique. In: *International journal of thermophysics* 23 (2002), Nr. 5, S. 1319–1325

[132] Teyssandier, F ; Prêle, D: Commercially available capacitors at cryogenic temperatures. In: *Ninth International Workshop on Low Temperature Electronics-WOLTE9*, 2010

[133] Patterson, Richard ; Hammoud, Ahmad ; Gerber, Scott: Performance of various types of resistors at low temperatures. In: *Test Report NASA Glenn Research Center* (2001)

[134] Stahl, Stefan: *Axialfrequenzverstärker mit integriertem Abwärtsmischer AF-DC-b und AF-DC-c*, 2010

[135] Dörr, Andreas: *Setup, test and optimization of detection electronics for high-precision mass measurements at PENTATRAP*, Ruprecht-Karls-Universität Heidelberg, Germany, Diss., 2011

[136] Weigel, Andreas: *Aufbau und Charakterisierung von Axialfrequenzverstärkern für das PENTATRAP-Experiment.* Ruprecht-Karls-Universität Heidelberg, Bachelor's Thesis, 2011

[137] Böhm, Ch ; Sturm, Sven ; Rischka, Alexander ; Dörr, Andreas ; Eliseev, Sergey ; Goncharov, Mikhail ; Höcker, Martin ; Ketter, Jochen ; Köhler, Florian ; Marschall, D u. a.: An ultra-stable voltage source for precision Penning-trap experiments. In: *Nuclear Instruments and Methods in Physics Research Section A: Accelerators, Spectrometers, Detectors and Associated Equipment* 828 (2016), S. 125–131

[138] Sailer, Tim ; Blaum, Klaus ; Sturm, Sven: *Aufbau einer Präzisionsspannungsquelle für das ALPHATRAP-Experiment.* Ruprecht-Karls-Universität Heidelberg, Bachelor's Thesis, 2015

[139] Schmöger, Lisa: *Kalte hochgeladene ionen für Frequenzmetrologie*, Ruprecht-Karls-Universität Heidelberg, Diss., 2017

[140] Gabrielse, G ; Tan, J: Self-shielding superconducting solenoid systems. In: *Journal of Applied Physics* 63 (1988), Nr. 10, S. 5143–5148

[141] D'Urso, Brian R.: *Cooling and self-excitation of a one-electron oscillator*, Harvard University, Diss., 2003

[142] Marques, J. P. ; Indelicato, P. ; Parente, F. ; Sampaio, J. M. ; Santos, J. P.: Ground-state Landé g factors for selected ions along the boron isoelectronic sequence. In: *Phys. Rev. A* 94 (2016), Oct, S. 042504

[143] Shchepetnov, Arseniy A. ; Glazov, Dmitry A. ; Volotka, Andrey V. ; Shabaev, Vladimir M. ; Tupitsyn, Ilya I. ; Plunien, Günter: Nuclear recoil correction to the g factor of boron-like argon. In: *Journal of Physics: Conference Series* Bd. 583 IOP Publishing, 2015, S. 012001

[144] Glazov, Dmitry A.: g-factor of middle-Z lithiumlike and boronlike ions. In: *Conference Talk PSAS*, 2018

[145] Sailer, Tim: *In Preparation*, Ruprecht-Karls-Universität Heidelberg, Diss., 2020

Danksagung

Am wichtigsten sind die Menschen die mich bei der Umsetzung dieser Arbeit sowie im täglichen Leben begleitet und unterstützt haben und denen ich hiermit danken möchte, soweit ich das mit Worten vermag.

Klaus Blaum, mein Erstbetreuer. Danke für deinen ständigen Beistand und deinen wertvollen Rat, dein Vertrauen und Verständnis, sowie das Teilen deiner unzerstörbaren Begeisterung und Zuversicht, in der Wissenschaft und im Leben. Danke für deine fast schon übermenschliche Verlässlichkeit und Erreichbarkeit und die großzügige Aufopferung des wertvollsten Gutes, deiner Zeit.

Sven Sturm, mein Zweitbetreuer und Teamleader von ALPHATRAP. Sven, ohne dich wären wir niemals da angekommen wo wir heute sind. Danke für deine unendliche Geduld beim Vermitteln deines immensen Wissens und deiner Erfahrung im Labor, sowie darüber hinaus. Danke, dass du mich in die Geheimnisse der kryogenen Elektronik eingeweiht hast. Ich bin jeden Tag aufs Neue beeindruckt von deiner Kreativität und Intuition in allen (Kfz:-)technischen Belangen.

Selim Jochim möchte ich herzlich für seine Bereitschaft danken die Rolle des Zweitgutachters meiner Arbeit zu übernehmen.

Robert Wolf, Martin Höcker und Bingsheng Tu unsere drei aufeinanderfolgenden Postdocs bei ALPHATRAP. Danke, dass ihr so massiv zur Entstehung unseres Experiments beigetragen habt und dass ich auf meinem Weg so viel von euch lernen durfte. Schade, dass ihr nicht einfach alle bei uns bleiben konntet. Ich wünsche euch und euren Familien das Beste in euren neuen Positionen und hoffe weiterhin mit euch in Kontakt zu bleiben.

Ioanna Arapoglou my first PhD fellow from the ALPHATRAP team. Thank you for your help and the great collaboration in the lab. Thanks for the many valuable and funny discussions we had and your assistance in language related questions in English as well as in Matlab. Your joyful nature made the sun shine even in our basement lab.

Alexander Egl und Tim Sailer meine ALPHATRAP Team- und Büro Kollegen. Jungs, danke für die tolle freundschaftliche Zusammenarbeit und für eure vollkommen unkomplizierte und lockere Art. Ihr habt es zu jeder Zeit geschafft mir ein Grinsen zu entlocken. In euren geschickten Händen ist ALPHATRAP bestens aufgehoben, was ihr bereits mehrfach auf beeindruckende Weise demonstriert habt.

Marko Turkalj Oreskovic, Sandro Krämer und allen anderen Ex-ALPHATRAP Kollegen die wichtige Vorarbeit auf dem Weg zur Verwirklichung unseres Experiments geleistet haben.

Den Penning-Trappern von PENTATRAP und THe-TRAP. Insbesondere Alexander Rischka und Marc Schuh die ich nun schon seit der Bachelor Arbeit kenne und die zu treuen Gefährten geworden sind. Danke für die unzähligen informativen Gespräche, für die gemeinsame Durchführung und Erstellung spannender Experimente und Prototypen und euren Enthusiasmus und Initiative für alles Technische.

Marina und Peter Danke Marina, einfach dafür, dass Du meine große Schwester bist auf die ich mich immer verlassen kann und die mich auch ohne Worte immer versteht. Ich bin unsagbar froh darüber, dass Du mit Peter deinen Seelenverwandten gefunden hast. Pete, insgeheim warst Du schon mein Schwager als ich Dich zum ersten Mal kennenlernen durfte ;-). Ich wünsche euch von Herzen das Beste auf eurem gemeinsamen Weg.

meine Liebe Susi DANKE für Dein wundervolles, unvergleichlich authentisches Wesen und für Deine Lebensfreude, mit der Du mich jeden Tag aufs Neue heilst. Danke, dass Du mich vervollständigst und mir unter allen Lebensumständen selbstlos zur Seite stehst. Du bist der mutigste und stärkste Mensch den ich kenne. Ich bin unendlich dankbar, dass ich das Glück hatte Dich zu treffen und für jeden einzelnen Augenblick mit Dir.